

Study of Wear and Viscous Heating in Paste Backfill Pipeline System

Bhargav Bharathan

Mining and Materials Engineering Department

McGill University, Montreal

Dec, 2016

A thesis submitted to McGill University in partial fulfilment of the
requirements of the degree of Master of Engineering

© Bhargav Bharathan 2016

All Rights Reserved

CONTENTS

1	INTRODUCTION	1
1.1	EROSION	2
1.2	VISCOUS HEATING	3
1.3	OUTLINE OF THESIS	4
2	LITERATURE REVIEW	4
2.1	EROSION	5
2.1.1	RESEARCH GAP	8
2.1.2	OBJECTIVE	9
2.2	VISCOUS HEATING	9
2.2.1	RESEARCH GAP	12
2.2.2	OBJECTIVE	12
3	FLUID RHEOLOGY	12
3.1	NEWTONIAN FLUIDS	13
3.2	NON-NEWTONIAN FLUIDS	14
3.2.1	POWER-LAW MODEL	15
3.2.2	CROSS MODEL	16

3.2.3	CARREAU MODEL	17
3.2.4	HERSCHEL-BULKLEY AND BINGHAM MODELS	17
3.3	NON-NEWTONIAN FLUID PROPERTIES	19
3.3.1	SLUMP TEST	19
3.3.2	CUP AND BOB VISCOMETER	21
3.3.3	VANE RHEOMETER	24
3.3.4	ARRHENIUS RELATIONSHIP - TEMPERATURE DEPENDENT PROPERTIES	28
3.3.5	THERMAL PROPERTIES	33
4	NUMERICAL MODELLING	35
4.1	EULERIAN-LAGRANGIAN	36
4.1.1	DISCRETE PHASE MODEL	37
4.1.2	DENSE DISCRETE PHASE MODEL	38
4.1.3	PARCELS	42
4.1.4	COUPLING BETWEEN PHASES	42
4.2	EROSION RATE	44
4.3	VISCOUS HEATING	45
5	METHODOLOGY	46

5.1	TAGUCHI METHOD	47
5.2	L-PIPE FLOW MODEL	47
5.3	MODEL DEVELOPMENT	48
5.4	MATERIAL PROPERTIES	51
5.5	PARTICLE SIZE DISTRIBUTION	53
5.6	BOUNDARY CONDITIONS AND SOLUTION PARAMETERS	55
6	RESULTS AND DISCUSSION	57
6.1	EROSION	57
6.2	VISCOUS HEATING	66
7	CONCLUSIONS AND RECOMMENDATIONS	74
7.1	RECOMMENDATIONS FOR FUTURE WORKS	74
8	APPENDIX A	83
9	APPENDIX B	89

LIST OF FIGURES

3.1	Shear rate vs shear stress for various fluids	14
3.2	Schematic arrangement showing the initial and final stress distribution of the cylindrical boger slump test (Pashias et al., 1996)	19
3.3	Schematic arrangement showing the initial and final stress distribution of the conical C143 slump test (Schowalter & Chrsitensen, 1998)	20
3.4	Dimensionless slump height as a function of dimensionless yield stress . .	22
3.5	Bob attachment in the viscometer for yield stress and consistency index measurement	22
3.6	Cup and bob attachment with outer jacket for water circulation	23
3.7	Mine-A consistency index at three different temperatures	24
3.8	Mine-A yield stress at three different temperatures	24
3.9	Mine-B consistency index at three different temperatures	25
3.10	Mine-B yield stress at three different temperatures	25
3.11	Mine-C consistency index at three different temperatures	26
3.12	Mine-C yield stress at three different temperatures	26
3.13	Vane attachment in the rheometer for yield stress measurement	27
3.14	Rheogram of 70% solid concentration of Mine-A tailings in water at three different temperatures	28
3.15	Arrhenius plot for Mine-A	30

3.16 Arrhenius plot for Mine-B	31
3.17 Arrhenius plot for Mine-C	31
3.18 Activation energies in Mine-A, Mine-B and Mine-C tailings-water mixture	32
3.19 Thermal conductivities of Mine-A, Mine-B and Mine-C backfill	34
3.20 Specific heat capacities of Mine-A, Mine-B and Mine-C backfill	34
5.1 L-pipe arrangement used in the laboratory	48
5.2 Erosion model pipeline schematic arrangement	49
5.3 Viscous heating model pipeline schematic arrangement	49
5.4 Rosin-Rammler curve fit for Mine-A sand particle sizes	54
6.1 Backfill flow model validation with experimental results	58
6.2 Erosion contour from numerical model at level 3800 - horizontal segment .	58
6.3 Vector contour from numerical model at level 3800 - horizontal segment .	59
6.4 Erosion contour from numerical model at level 3800 - vertical segment . . .	59
6.5 Vector contour from numerical model at level 3800 - vertical segment . . .	59
6.6 Erosion contour from numerical model at level 6400 - horizontal segment .	60
6.7 Erosion contour from numerical model at level 6400 - elbow segment . . .	60
6.8 Particle impact angle in a 90° elbow	60
6.9 Measurement points along pipe circumference	61

6.10 Erosion validation in Level 3800	62
6.11 Discrete phase volume fraction and secondary flow at level 3800	62
6.12 Erosion validation in Level 6400	63
6.13 Discrete phase volume fraction and secondary flow at level 6400	63
6.14 Taguchi analysis main effects plot	65
6.15 Taguchi analysis interaction plot	65
6.16 D* comparison in three mines	66
6.17 Temperature rise in Mine-A	67
6.18 Temperature rise in Mine-B	67
6.19 Temperature rise in Mine-C	68
6.20 Influence of viscous heating on temperature rise	69
6.21 Influence of thermal conductivity on temperature rise	69
6.22 Influence of consistency index on temperature rise	70
6.23 Influence of mass flow rate on temperature rise	70
6.24 Influence of specific heat capacity on temperature rise	71
6.25 Influence of yield stress on temperature rise	71
6.26 Temperature contour of pipeline entry, middle and exit segments	72
6.27 Temperature distribution at exit showing higher temperatures in vertical segment and elbow and temperature drop in horizontal segment	73

6.28 Temperature distribution in Mine-A	73
---	----

LIST OF TABLES

3.1 Yield stress and flow behaviour index of Fluids	16
4.1 Erosion functions for steel	44
4.2 Piecewise linear profile of the impact angle function	44
5.1 Factors used in the erosion model	46
5.2 Grid independence results for Mine-A	50
5.3 Grid independence results for Mine-B	50
5.4 Grid independence results for Mine-C	50
5.5 Pipeline dimensions for Mine-A, Mine-B and Mine-C	51
5.6 Backfill constituents densities	51
5.7 Material properties for erosion validation case	52
5.8 Material properties for viscous heating validation case	53
5.9 Rosin-Rammler sand particle size distribution parameters	54
5.10 DPM wall discrete phase reflection coefficients	55
5.11 Erosion model boundary conditions	56
5.12 Granular phase parameters	56

5.13	Viscous heating model boundary conditions	57
6.1	% Error in Level 3800 erosion results	61
6.2	% Error in Level 6400 erosion results	61
8.1	Taguchi variables for erosion model	83
8.2	Erosion model material properties	84
8.3	Erosion model material properties	85
8.4	Material properties of Mine-A viscous heating model	86
8.5	Material properties of Mine-B viscous heating model	86
8.6	Material properties of Mine-C viscous heating model	87
8.7	Sand and tailings composition	87
8.8	Mine-A sand particle size distribution	88

ACKNOWLEDGEMENT

I would like to express my deepest gratitude to Prof. Agus P. Sasmito, my supervisor at McGill University, who offered me the opportunity to do my Master of Engineering thesis. His patience and guidance along with enthusiastic encouragement has helped me accomplish the goals of my thesis. It was an overwhelming experience working and learning from him everyday.

I would also like to thank Prof. Ferri Hassani for his support and providing me with access to the Mining Geomechanics Laboratory. I would like to thank Dr. Pejman Nekoovaght, Mrs. Maureen McGuinness for helping me with setting up and conducting the laboratory experiments. A special thanks to Dr. Mehrdad Fadei Kermani and Mr. Kelvin Creber for conducting tests in the mine to obtain data with which our results were validated with. I would also like to thank Mr. Dilip Sembakutti, Mr. Anaas Jadal, Mr. N'Guetta Yannic Kassi, Mr. Zhishuang Liu, Ms. Joyce Yang Song and Mr. Mohamed Zaki for their assistance with the laboratory experiments and numerical simulations.

I would like to extend my gratitude to the fellow members of Dr. Sasmito's group, Mr. Mahmoud Alzou'bi, Mr. Aurelien Nie-Rouquette and Mr. Saad Akhtar and my friends Mr. Divye Malik and Mr. Badal Yadav for giving me precious advice during the course of the thesis and setting up a great work environment.

The role of Mr. Pier-Luc St-Onge and his McGill HPC team in fulfilling all my supercomputing needs and playing a big part in the smooth progress of my research is gratefully acknowledged.

Last but not the least I want to convey my deepest gratitude to my family and friends for their continuous and unwavering support that encouraged me to overcome all obstacles and challenges throughout my study.

ABSTRACT

Mine Backfill is transported from the surface to underground stopes through pipelines. They are driven through a combination of pumps and varying pipe geometry utilizing the effect of gravity. The material transported contains a combination of water, sand and mine tailings in predetermined proportions. Cement is added in scenarios where an improvement in the mechanical strength of the backfill is desired, but this also increases the overall cost of the system. Transfer of backfill through long pipelines poses significant problems in the system. This thesis focusses on the erosion in the pipe wall due to the high solid content and the gradual temperature rise due to its inherently high viscosity.

Erosion is brought about by the impact of solid particles in the backfill with the pipe wall causing material removal that results in a decreased lifetime and an increase in repair and replacement cost. A numerical model of the backfill pipeline from an underground mine is developed to study the impacts of system design parameters on erosion. The design parameters analysed are solid percentage, flow velocity and sand percentage. The ANSYS multiphase model is solved for this purpose using Dense Discrete Phase Model (DDPM) with Kinetic Theory of Granular Flow (KTGF) formulation that solves the continuous phase flow field in Eulerian reference frame and the trajectories of injected granular phase in Lagrangian reference frame.

The high viscosity of the backfill gives rise to the viscous heating phenomenon that causes a rise in temperature during transport which in-turn causes rheological changes in the backfill. Numerical models of the backfill pipelines from three different underground mines are developed to investigate the relationship of backfill rheological properties and sand particle interaction with temperature rise. The viscous heating phenomenon is solved using the native energy model in ANSYS Fluent using C language based codes in the form of User Defined Functions (UDF) to modify the energy equations.

The thesis is targeted at developing techniques to predict erosion and temperature rise in

pipelines by studying the effect of individual factors and how their manipulation provides control over their impacts through the use of numerical models. The results from the erosion model and Taguchi analysis shows that flow velocity has the highest impact on erosion followed by sand percentage and solid percentage. The results from the viscous heating model indicate that a change in yield stress of the material has the highest impact on the viscous heating phenomenon followed by consistency index, coefficient of pressure, thermal conductivity and mass flow rate. The presence of sand in the backfill has a significant effect on the temperature rise. The results from the numerical simulations are compared and validated against in-situ mine data obtained from the three mines used in the study showing good agreement.

ABRÉGÉ

Le transport hydraulique est le système privilégié pour le remblai minier. Une série de pompes, assistées par la gravité, achemine le remblai à travers des tuyaux de différentes tailles vers les chantiers souterrains. Le matériel transporté est une combinaison de résidus miniers, de sable et d'eau en quantités prédéterminées. Du ciment peut être ajouté lorsque le remblai sert pour le soutènement, ce qui ajoute au coût au système. Le passage du remblai à travers des longueurs importantes de tuyaux cause des problèmes importants pour le système. Cette thèse en examine deux en particulier: l'érosion des parois créée par la haute teneur solide du remblai, ainsi que l'augmentation graduelle de la température du remblai dû à la haute viscosité du matériel. L'érosion est causée par l'impact des particules solides du remblai contre les parois des tuyaux, ce qui cause une réduction de leur épaisseur et de leur durée de vie, et force leur remplacement et augmente les frais de maintenance. Une modèle numérique représentant le système de remblai d'une mine a été développé afin d'étudier la façon dont différents paramètres de design affectent l'érosion. En particulier, le pourcentage de solide, la vitesse du flot et le pourcentage de sable sont analysés. Le modèle multiphase de ANSYS est résolu grâce au modèle de Phase Discrète Dense (DDPM) et de la formulation de la Théorie Cinétique du Flot Granulaire (KTGF) qui résout le champ vectoriel de phase continue dans un cadre de référence Eulérien, et les trajectoires des phases granulaires injectées dans un cadre Lagrangien.

La haute viscosité du remblai engendre le phénomène de chauffage visqueux qui cause une augmentation de température durant le transport, ce qui peut causer des changements rhéologiques dans le remblai. Des modèles numériques représentant trois systèmes de transport de différentes mines ont été développés pour analyser la relation entre les propriétés rhéologiques et les interactions des particules de sable quand la température augmente. Le phénomène de réchauffement visqueux est résolu en utilisant une Fonction Définie par l'Usager (UDF) écrite en langue C afin de modifier les équations du modèle

d'énergie natif de ANSYS Fluent. Cette thèse vise à développer des techniques pour prédire l'érosion et l'augmentation de température dans une pipeline en étudiant comment la variation de certains facteurs permet de contrôler leur impact grâce à l'usage de modèles numériques.

Les résultats du modèle d'érosion et l'analyse Taguchi indique que la vitesse du flot est le facteur qui influence le plus l'érosion, suivi par le pourcentage de sable, et pourcentage de solides. Le chauffage visqueux quant à lui est affecté principalement par les contraintes d'élasticités, suivi par l'index de consistance, le coefficient de pression, la conductivité thermique et le flot de matériel. La présence de sable dans le remblai a des effets importants sur l'augmentation de chaleur. Les résultats des simulations numériques sont comparés et validés par-rapport à des données de terrain de trois mines, et montrent une bonne corrélation.

NOMENCLATURE

A	Face area [m^2]
A'	Pre-exponential factor
a	Carreau-Yasuda parameter
C	Concentration [%]
C_D	Coefficient of drag
d	Diameter [m]
d_n	Mean diameter [m]
D^*	Viscous heating criterion
e	Coefficient of restitution
F	Force [N]
\vec{F}	Force vector per unit volume [Nm^{-3}]
g	Acceleration due to gravity [ms^{-2}]
g_0	Radial distribution function
H	Total height of slump mould [m]
h	Total final height [m]
h_0	Yielded region height [m]
h_0'	Dimensionless yielded region height
h_1	Unyielded region height [m]
h_1'	Dimensionless unyielded region height
$\bar{\bar{I}}$	Unit tensor

k	Consistency index [$Pa s^n$]
k_{eff}	Effective conductivity [$W m^{-1} K^{-1}$]
K	Inter-phase exchange coefficient
m	Mass [kg]
\dot{m}	Mass transfer rate per volume [$kg s^{-1} m^{-3}$]
\dot{m}_s	Particle mass flow rate [$kg s^{-1}$]
M	Torque [Nm]
n	Flow behaviour index
n'	Rotational speed
n''	Spread diameter
p	Pressure [Pa]
R	Universal gas constant [$JK^{-1}mol^{-1}$]
R_i	Vane radius, bob radius [m]
R_H	Slump cone bottom radius [m]
R_o	Container radius [m]
R_0	Slump cone top radius [m]
Re	Reynolds number
s	Slump height [m]
s'	Dimensionless slump height
t	Time [s]
T	Absolute temperature [K]

T_e	Temperature of surroundings [K]
T_o	Inlet temperature [K]
T_0	Temperature shift [K]
T_α	Reference temperature [K]
u	Velocity [ms^{-1}]
\vec{u}	Velocity vector [ms^{-1}]
w	Length from top of the slump mould [m]
Y_d	Cumulative retained percentage [%]

GREEK SYMBOLS

Δt	Time step [s]
α	Volume fraction
α'	impact angle [°]
λ	Bulk viscosity [Pas]
λ'	Relaxation time [s]
μ	Viscosity [Pas]
μ_c	Molecular viscosity [Pas]
τ	Shear stress [Pa]
$\bar{\bar{\tau}}_q$	Phase stress tensor [Pa]
τ_y	Yield stress [Pa]
τ_y'	Dimensionless yield stress

$\dot{\gamma}$	Strain gradient [s^{-1}]
ψ	Viscous dissipation function
ρ	Density [kgm^{-3}]
η	Plastic viscosity [Pas]
η_0	Zero viscosity [Pas]
η_∞	Infinite viscosity [Pas]
θ	Angle of internal friction [$^\circ$]
Θ	Fluctuating energy

SUBSCRIPTS

b	Body
D	Drag
fr	Frictional
l	Liquid
m	Material
p	Paste - Continuous phase
s	Solid - Discrete phase
v	Volume
w	Weight
w'	Wall
x	Horizontal coordinates

y Vertical coordinates

coll Collisional

face Face

kin Kinetic

lift Lift

1 INTRODUCTION

Mining processes produce a large amount of waste into the environment that are distinct for each mine site depending on the local geology. In mining operations, the ore-waste discrimination is made on the basis of a cut-off grade. If block grade is above cut-off grade, it is assessed as ore and the remaining as waste. Mine waste is categorized into different types based on their physical and chemical composition, how they are managed at the mine site and their potential for causing harm to the environment. The types of waste include: overburden, waste rock, tailings, slags, mine water, water treatment sludge and gaseous waste (Rankin, 2011). Waste management methods employed by each mine are dependent on the type of waste, cost involved, environmental effects and risk of failure of system. The waste water is recycled and used in dust suppression systems, mineral processing or discharged into the environment after treatment (Lottermoser, 2011). Solid wastes are used for backfilling in underground and open pit mines, stored in piles and used in the construction of roads and dams (European Commission, 2009).

Backfilling is a waste management method that sends the waste obtained from the mining process back into the ground to provide stability to the mine walls for successful extraction from adjacent stopes (Barrett et al., 1978). The open stope voids are filled with backfill to maintain stability for the adjacent work areas thereby reducing the risk of local and regional ground failure from the collapse and caving in of the structure. Backfill is typically made from waste rock or dewatered tailing residues and is often mixed with cement to achieve moderate strengths. It is delivered to stopes via trucks or by pumping as dense slurry or paste through boreholes and pipelines. Paste backfill requires a relatively small diameter pipeline in comparison to other systems and it provides an extremely flexible system in terms of changes in orebody geometry, such as stope width, dip and length (Wayment, 1978). The backfill is loaded by its weight and through lateral and shear support from adjacent rock in addition to potential loadings from the back, sides and drawn rockfill (Barrett et al., 1978). The amount of water added determines

the backfill fluidity and balances its mechanical properties. The high solid concentration of the backfill makes it behave as a non-Newtonian fluid. The flow of a highly viscous non-Newtonian fluid through pipelines over long distances for long periods of time affects the pipeline as well as the material properties of the fluid.

The research described in this thesis stems from the need to quantify and explain the erosion and backfill temperature rise in long distance paste backfill transport pipelines. Currently, there exist very few experimental studies that investigate the heat transfer processes in non-Newtonian fluids. Research progress in non-Newtonian rheology has been mostly aimed at magma flows, polymer solutions and polymer melts, with less attention towards slurries and thick pastes specifically mine paste backfill. The studies are carried out using CFD software ANSYS Fluent and the results are validated using mine in-situ data.

1.1 EROSION

Erosion in pipelines is a major issue that is faced by mining companies during operation. Long distance and buried pipelines are generally designed to operate for the system's life without replacement (Cooke et al., 1999). Any bursts in the pipeline will result in a large quantity of material escaping from the pipeline and depositing in the drift. This would cause unexpected downtime in the mine affecting production. Frequent pipe replacements can amount to high costs. To prevent such circumstances a method for the accurate prediction of wear is required. The optimum method is the installation of spools in existing backfill pipelines to monitor the wear rate in a real-time scenario. The limitations include the inability to vary design parameters such as solid concentrations, flow velocity, particle size distribution and pH amongst others (Cooke et al., 1999). The restraint in flexibility proves difficult to study the effects of each parameter on wear directly in the mine. Experiments may be performed in laboratories using recirculating pipe loops by mimicking the actual backfill flow in mines. It has the advantage of being

able to vary the different design parameters but also has a few limitations. The scaling of the data obtained from small diameter pipes to large diameter pipes over a few days of operation may prove cumbersome in addition to the difficulty in maintaining constant rheological properties over the course of the experiment (Faddick, 1975). The erosion in pipes carrying backfill are influenced by numerous factors broadly classified as variables such as carrier fluid, dispersed particles and its bulk properties, flow field, pipe material and its surface properties (Steward & Spearing, 1992) (Humphrey, 1990) (Gustavsson, 2002). This thesis focusses on the effects of flow velocity, sand and total solid fractions on the erosion rate in a pipeline carrying mine backfill from one mine named as Mine-A in the study. The effects of corrosion is not included in this thesis and the research is limited to erosion.

1.2 VISCOUS HEATING

Viscous heating phenomenon arises in fluid flows with high viscosity. The mechanical energy supplied to the backfill paste is partly dissipated out to the environment as heat and the remaining energy increases the fluid temperature (Sestak & Charles, 1987). Temperature changes cause changes to the rheological properties of the backfill. Being non-Newtonian the backfill viscosity is temperature dependent and a rise in temperature reduces the viscosity of the fluid in addition to a decrease in yield strength. Changes in backfill strength will affect the curing time after deposition and the mechanical strength after the curing process. Temperature determination is done on the mine site either by directly measuring at the exit of the pipeline or by using pill sensors that are introduced in to the flow at the pipe inlet and exits out of the outlet. These sensors record temperature data along the length of the pipeline. A numerical model to predict the temperature rise in a pipeline for different compositions and mixtures that may be used in the mine is necessary. This thesis focusses on the effect of viscous heating on temperature rise in pipelines carrying mine backfill from three mines, Mine-A, Mine-B and Mine-C. The unique mineral composition of each mine tailings defines their rheological properties and

behaviour when exposed to high and low temperatures.

1.3 OUTLINE OF THESIS

In this thesis the material properties of non-Newtonian paste backfill was determined at different temperatures using a cup and bob viscometer. Numerical models were then developed for determining erosion using Eulerian-Lagrangian DDPM KTGF formulation and viscous heating by using UDFs to modify the source terms of the energy equations. The results were validated against in-situ mine data and studies were conducted to determine the impact of individual design factors on erosion and their interaction with each other. The impact of temperature dependence of the material properties and viscous heating on the temperature rise was also studied. In addition, the work concentrates on the determinign the influence of material properties and design parameters on the flow of paste backfill in long distance underground pipelines and its impact on erosion and temperature rise which differs from other works laid out in the literature that is reviewed below.

2 LITERATURE REVIEW

In this section the work done by previous researchers and published literature related to this study are explored. The first part reviews different erosion models, modelling of multiphase flows and the use of CFD for erosion prediction. The second part focusses on the viscous heating phenomenon, its application in non-Newtonian fluids, the factors that affect it and the influence of temperature on rheological properties. Lastly, the gap in the research is discussed followed by the objectives of the study and the approaches adopted to tackle erosion and temperature rise in pipelines are introduced.

2.1 EROSION

Wear as defined as the gradual deterioration of any part in the system to the point of danger or uselessness (Miller, 1986). It is further divided into two types; erosion and corrosion. Erosion involves the removal of material by mechanical activities such as abrasion or cavitation and corrosion involves material removal by chemical or electrochemical means. The gradual degradation of material from pipe walls affects the integrity of a piping system. Common industrial practices involve the use of protective wear linings. The quality of linings used is restricted by cost and frequency of replacement. Protective linings are further classified for abrasion and impact control. Companies inspect, locate and replace affected pipe segments during scheduled maintenance checks. Through the use of standard equipments the wear rates in pipes are monitored. The instruments range from non-destructive sonar based devices to simple thickness measurements from pipe samples. This thesis aims to study the effects of individual parameters that will assist in predicting erosion rates and enable proactive scheduling and maintenance.

A large number of parameters influence erosion and based on the importance given to each parameter numerous equations and erosion models have been developed. An extensive review conducted on solid particle erosion in oil and gas pipelines compared different erosion models and concluded that there is still room for development in incorporating particle size distributions in the models (Parsi et al., 2014). In one of the earliest erosion models developed, the authors considered motion of particles and material properties decisive in causing erosion (Finnie, 1960). The materials were divided into ductile and brittle and the erosion equations were developed for a single grain striking a surface at low and high impact angles. An erosion model based on fluid-particle interactions, wall impingement and particle trajectories was developed and implemented as a CFD code (Edwards et al., 1998). The study was performed for a sudden pipe expansion geometry for different turbulence models, the effects of these models on particle trajectory and velocity was observed but not on erosion itself. An empirical relation was developed to predict erosion rate in dry and wet carbon steel (Ahlert, 1994). The authors conducted

direct impact experiments at different impact angles and particle shapes. Another method proposes the use of empirical relations to predict erosion rates (Y. Oka & Yoshida, 2005) (Y. I. Oka et al., 2005). The authors included the effects of particle properties and mechanical properties such as target material hardness, work hardening and load relaxation ratio, impact angles, speed, particle size and types of materials. An erosion model for ductile materials based on experimental data from air-sand flows showed that the erosion rate in tees was about half of that in elbows (Salama, Venkatesh, et al., 1983). An erosion model for multiphase flows that accounted for material properties, particle shape factor, penetration factor, elbow radius, impact velocity and sand production rate was based on single phase erosion model (McLaury et al., 1999).

Experiments conducted in a closed-loop pipeline to test the erosion rate in steel, elastomers and polymers showed that under jet-impact conditions the plastics had a higher erosion rate than steel whereas, under pipeline conditions, the plastics had better erosion resistance than steel (Steward & Spearing, 1992). The authors reason that the high velocity jets quickly penetrate the surface of plastic accelerating wear which was not the case in pipelines.

Other studies emphasized the importance of knowledge of the flow field surrounding impinging particles and target for understanding slurry erosion (Clark, 1992). The work reviewed the effect of liquid viscosity, liquid density, particle size range, particle density, solid concentration, target shape and suspension free stream velocity on erosion. It was observed that the actual impact velocities of particles on a target may vary from the free stream velocity of the suspension and under some circumstances most, or even all particles that are directed at a target may fail to collide with it. The authors further highlighted the need for realistic analytical models of particle trajectories to complement experimental erosion tests to fully understand the erosion process.

An attempt was made to develop a universal wear map that predicted the local wear by impinging water-sand mixtures via jets on stainless steel plates (Gnanavelu et al.,

2009). The results were validated against CFD models and some quantitative variations in profile were observed, which was attributed to the use of a single particle size, ignoring particle-particle interactions and alignment of the nozzle with the test specimen.

The effects of impact velocity and impact angle of sand on erosion in ductile and brittle materials was studied through experiments and CFD modeling (Q. Nguyen et al., 2014) (V. Nguyen et al., 2014). The authors used the Eulerian-Lagrangian approach treating the sand as the discrete phase and $k - \omega$ turbulence model was adopted. The authors observed peak erosion rate at 40° impact angle and a linear relationship with impact velocity. The erosion rate was over-predicted by the CFD simulations which was associated with particle shape parameters and particle interference. A similar study was performed on stainless steel by developing an approximate erosion equation from experimental testing to predict local wear depth (Mansouri et al., 2015). The authors found good agreement in the wear profile with experimental results for 75° impact angle but found discrepancies at 45°. They based their erosion correlation on normal impingement jet testing data and found low accuracy with application in low angles.

A study was performed to analyse the coupled effects of solid particles and gas velocities on erosion of elbows in natural gas pipelines (Lin et al., 2015). Using the DPM model they observed an increase in erosion rate with increase in gas velocity, particle size, particle concentration. A procedure was designed to calculate sand erosion in standard pipe components using CFD and DNV RP (Det Norske Veritas RP O501, 2007) for calculation of erosion (Huser & Kvernfold, 1998). The authors found good agreement with the experimental results and attributed the differences to the effects of multiphase flow on particle distribution and erosion patterns.

A study modelling the flow of a sand-water slurry using ANSYS Fluent for 5% - 30% solid concentration by volume for different particle sizes and flow velocities was performed (Nabil et al., 2014). The authors aimed to observe the capability of CFD in modelling complex slurry flows in pipelines. They used a Eulerian-Eulerian model with $k - \epsilon$

turbulence model to validate against experimental results and observed an asymmetry in particle distribution that increased with increase in particle size but decreased with increase in concentration. With increase in concentration the velocity of the flow was seen to be asymmetric as well being higher in the top portion of the pipe. The study used three particle sizes and not a distribution making it difficult to be translated to a real-time scenario.

The DDPM model and the KTGF formulation have been used together and individually in numerous studies and fields. Coal gasification in circulating fluidized bed was numerically modelled using DDPM to model the particulate phase and KTGF to model the particle interactions (“Towards a hybrid Eulerian-Lagrangian {CFD} modeling of coal gasification in a circulating fluidized bed reactor”, 2015). KTGF was used to model dense granular flow in high shear mixer granulators (Ng et al., 2009).

The validity of the application of Kinetic Theory of Granular Flows (KTGF) with the Dense Discrete Phase Model (DDPM) and the Two Fluid Model (TFM) was evaluated in 2D and 3D bubbling fluidized beds and granular flow systems (Cloete et al., 2010) (Cloete et al., 2011). The authors observed that the DDPM model was able to solve finer details in the volume fraction fields compared to the TFM model. The authors predicted this behaviour was due to Lagrangian approach which has no numerical diffusion.

2.1.1 RESEARCH GAP

Most studies carried out focus on low solid concentration slurries which fall into the Newtonian flow regime and/or use turbulence flow models (Cloete et al., 2010) (Cloete et al., 2011) (Q. Nguyen et al., 2014) (V. Nguyen et al., 2014) (Nabil et al., 2014). Fluid flows with high solid concentrations being used in mines display non-Newtonian multiphase flow behaviour with dispersed sand particles requiring in-depth studies to characterize and define their complex flow nature. Due to the difficulty in measurement techniques, very few experimental data are available for flow of highly viscous fluids and their at high

solid concentrations (Bozzini et al., 2003).

2.1.2 OBJECTIVE

The objective of modelling erosion using CFD is to analyze and study the effects of solid concentration, flow velocity and sand fraction on erosion. The flow behaviour of non-Newtonian paste backfill is characterized by the Bingham plastic model. The DDPM model with KTGF formulation is used to model the discrete phase. The results from the erosion model are then analysed using Taguchi statistical model to discover the impact on erosion by each factor individually and in relation with one another.

2.2 VISCOUS HEATING

Initiation of flow in a fluid requires an application of mechanical energy. Fluids with high viscosity require a higher energy compared to those with lower viscosity for deformation and initiation of the flow. As per the first law of thermodynamics, the change in internal energy in a closed system is equal to the amount of heat supplied to the system minus the work done by the system. During the flow of a viscous fluid through pipelines, mechanical energy is supplied by a pump or in the form of hydrostatic pressure to move the fluid leading to a positive increment in internal energy. Depending on the thermal properties of the fluid, pipeline and surroundings, a fraction of the internal energy is dissipated out to the environment as heat and the remaining increases the temperature of the fluid. This phenomenon is defined as the viscous heating phenomenon (Sestak & Charles, 1987). Numerous researches have been conducted on viscous heating, the effect of temperature on rheological properties of non-Newtonian fluids and their effects on heat transfer. Heat transfer problems concerning forced convection has been a widely researched field for many years. Studies for both Newtonian and non-Newtonian fluids under different boundary conditions have been investigated.

Laminar forced convection in a Newtonian fluid was analysed with constant properties and viscous dissipation at constant heat flux and constant wall temperature boundary conditions (Aydin, 2005b) (Aydin, 2005a). The authors studied the relation between the Brinkman number and the viscous dissipation at each case. Laminar convective heat transfer of a non-Newtonian fluid using Bingham model with Papanastasiou approximation was studied using numerical methods (Min et al., 1997). The authors concluded that for hydrodynamically developing flow, shorter entrance length was required to reach a fully developed flow field and for simultaneously developing flow, the heat transfer showed good agreement with the predictions from thermally developing flow.

The effects of viscous dissipation and temperature dependent viscosity in laminar forced convection was analysed in straight microchannels (Del Giudice et al., 2007). The authors considered a linearly varying viscosity with respect to temperature while other fluid properties were held constant and observed their effects on the development of thermal field, modifying both heat fluxes and velocity distributions. The authors concluded that the effect of temperature dependence of viscosity and viscous dissipation cannot be neglected.

Significant temperature increases were observed in microtubes and microchannels that occur due to viscous dissipation at a low Reynolds number flow even for a fluid with high viscosity and low heat capacity and the increase in temperature reduces the viscous dissipation effect in liquids (Koo & Kleinstreuer, 2004). Numerous other studies observed the effects of Peclet number, Reynolds number, Eckert numbers, Prandtl number, Knudsen number, Poiseuille number, Brinkman number on heat transfer in elliptical ducts, microtubes and microchannels with viscous heating (Tunc & Bayazitoglu, 2001) (Koo & Kleinstreuer, 2004) (Morini, 2005) (Ragueb & Mansouri, 2013).

Fully developed laminar forced convection of a Bingham plastic in a circular duct under different boundary conditions was analysed and the effects of viscous dissipation and yield stress on the asymptotic temperature profile and Nusselt numbers was observed (Khatyr et al., 2003). The authors used constant physical properties and negligible axial

conduction. They concluded that constant wall temperature and convection boundary conditions led to the same asymptotic values of Nusselt number and in convection case this number was independent of Biot number. The authors found good agreement upon validation of their theoretical results with those from literature for Newtonian fluids. In a study conducted by (Boualit et al., 2011) on the laminar flow of Bingham fluid between two parallel plates taking into account viscous dissipation, the authors concluded the velocity increase due to temperature rise increases the heat transfer.

A numerical study using finite volume method for a Herschel-Bulkley fluid with Papanastasiou regularization in a circular pipe with uniform wall temperature was conducted (Labsi et al., 2015). They found that by neglecting the viscous dissipation and temperature dependence of the fluid consistency could lead to an excess of 50% underestimation of the heat transfer phenomenon due to the viscous nature of the fluid.

The effect of temperature increase due to viscous dissipation of non-Newtonian fluids in an oscillatory pipe flow using the power law model was studied (Herrera-Velarde et al., 2001). They found that the temperature increased with the power parameter and with the speed of oscillation. The authors employed a variable viscosity inelastic power law model to characterize the fluid rheology.

The effects of temperature on sweet potato starch mixed with low concentrations of xanthan gum was analysed by (Choi & Yoo, 2009). The authors used the power law model and found that the activation energy decreased with increase in xanthan concentration and the decrease in apparent viscosity was profound at lower xanthan concentrations. Laboratory tests using rotational viscometer and dynamic shear rheometer were conducted for crumb rubber modified binder (Thodesen et al., 2009). The authors studied the effectiveness of statistical regression and neural network in predicting the viscosity values. Decreasing viscosities with increasing temperatures was observed in aqueous and aqueous alcoholic mixtures with ammonium chloride and ammonium bromide salts (Saeed et al., 2009). An increasing viscosity with increasing salt concentration was also

observed at a fixed temperature. The viscous heating effects in magma by considering it as a Bingham fluid with temperature dependent viscosity was studied (Costa & Macedonio, 2003). The authors observed temperature increase and velocity profiles consistent with lava flows.

2.2.1 RESEARCH GAP

Majority of heat transfer literature of non-Newtonian fluids neglect either temperature dependent rheological properties and/or the viscous heating phenomenon. Paste backfill used in mines possess high viscosities and display profound temperature rises during flow. The extent of the influence viscous heating has on this rise needs to be studied along with the effects of material physical properties.

2.2.2 OBJECTIVE

The objective of modelling temperature rise in paste backfill using CFD is to ascertain the effects of viscous heating and material properties on temperature rise. Temperature dependent rheological properties are obtained from experiments conducted at different temperatures. Using the non-Newtonian Bingham plastic model the influence viscous heating has on temperature rise is studied by modifying the source terms in the energy equation. Temperature dependent and independent rheological properties with convection and zero heat flux boundary conditions are used and their differences are observed. This study is performed on mine backfill from three mines, Mine-A, Mine-B and Mine-C.

3 FLUID RHEOLOGY

Rheology is the science of deformation and flow of materials. The term itself was coined by Eugene C. Bingham and his associates from Lafayette College ,USA. 'Rheo' in greek

means flow. Rheology involves the study of kinematics which deals with the geometrical aspects of deformation and flow; the laws of conservation that handle the forces, stresses and energy exchanges that determine a flow; and the constitutive relations that link the forces, stresses and motion with the material properties and the flow phenomenon. Rheology derives its roots from the basics of solid and fluid mechanics. The densities of the fluid phase and the dispersed phase affect the density of the multiphase fluid as a whole. Individual phase concentrations and densities can be expressed through the relationship shown in equations (3.1) and (3.2) as explained by (Wasp et al., 1977).

$$C = \frac{C_w \rho_m}{\rho_s} = \frac{100 \frac{C_w}{\rho_s}}{\frac{C_w}{\rho_s} + \frac{100 - C_w}{\rho_l}} \quad (3.1)$$

$$\rho_m = \frac{100}{\frac{C_w}{\rho_s} + \frac{100 - C_w}{\rho_l}} \quad (3.2)$$

where, w , m , s and l denote weight, material, solid and liquid respectively. The equations (3.1) and (3.2) help provide an understanding of the differentiation between dilute and dense flows. A dilute flow typically has a particle volume concentration of less than 10% and those higher are called dense flows.

3.1 NEWTONIAN FLUIDS

A fluid is a substance that continually deforms under the influence of shear stress. Viscosity is the property of a fluid that measures its resistance to deformation. In a Newtonian fluid, the applied shear stress τ is directly proportional to the shear rate $\dot{\gamma}$ and viscosity μ is the constant of proportionality. Figure 3.1 shows the relationship between shear rate and shear stress for various kinds of fluids both Newtonian and non-Newtonian. The shear rate-shear stress relationship is used to define the rheology of a material. Equation (3.3) below shows the relationship between these parameters derived

from Newton's law of viscosity that states that for a fluid at rest between two parallel plates, the force required to move the top plate is proportional to the velocity and area and inversely proportional to distance between the plates. A plot made based on this equation will generate a straight line passing through the origin and shows that shear stress is a linear function of shear rate. Viscosity is the single flow parameter that characterizes the laminar flow of a Newtonian fluid giving rise to the term "one-parameter" fluids. Water, alcohol and air are general examples of Newtonian fluids. They exhibit a viscosity that is only temperature dependent.

$$\tau_{yx} = \mu \frac{du}{dy} \quad (3.3)$$

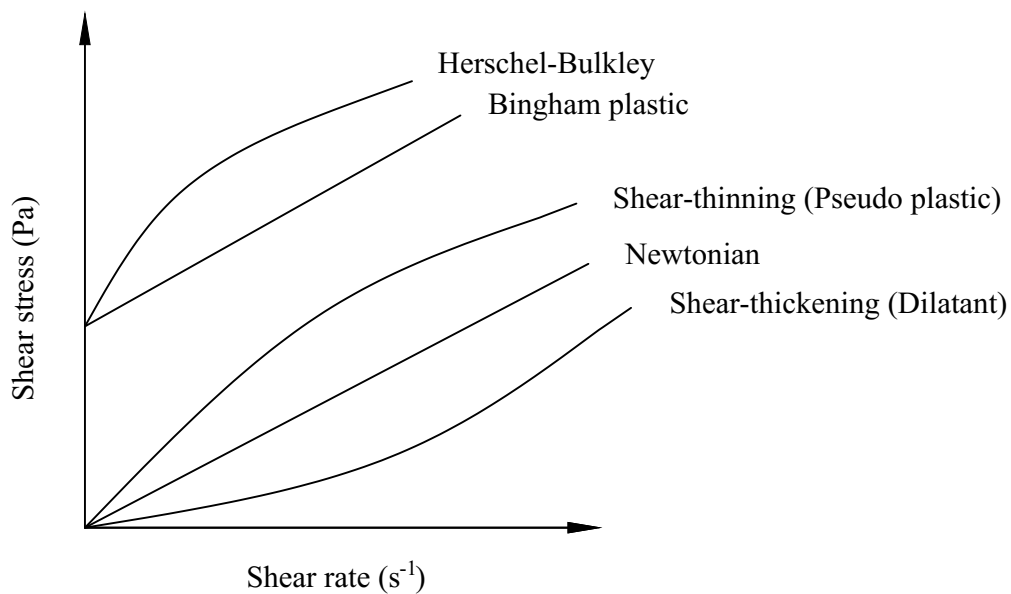


Figure 3.1: Shear rate vs shear stress for various fluids

3.2 NON-NEWTONIAN FLUIDS

Newtonian fluids generally require a good knowledge of the fluid viscosity for evaluation and comparison of laminar flow behaviour. In the case of non-Newtonian fluids the establishment of what constitutes as viscosity, even in analytical terms, is a matter upon which there is no general agreement (Wasp et al., 1977). In non-Newtonian fluids, the viscosity is dependent on both shear stress and shear rate and is termed apparent viscosity

η . For Newtonian fluids, the fluid viscosity and apparent viscosity are equal. Unlike Newtonian fluids, multiple rheological parameters are required to define the relationship between shear stress and shear rate for a non-Newtonian fluid.

Non-Newtonian fluids could display either a non-linear relationship between shear stress and shear rate, have a yield stress, or viscosity that is dependent on time or deformation history (thixotropic fluid) or a combination of all the above. With the increase in shear rate if there is an increase in viscosity, then the fluid is said to be shear thickening (dilatant). A mixture of cornstarch in water is a common example. Fluids that experience a decrease in viscosity when the shear rate increases are called shear thinning fluids (pseudo-plastics). Ketchup, paint and blood are examples of pseudo-plastics.

Fluid flow is highly dependent on the viscosity of fluids. Successfully defining the viscosity is key in determining the flow behaviour of a fluid. As per Newton's law of viscosity by assuming a case where a fluid is flowing as a series of layers sliding past each other, the resistance to flow arises because of the friction between these layers. For a layer to slide over another twice as fast, a resisting force that is twice as greater needs to be overcome. If both the layers involved in the sliding have the same speed of motion, then there would be no resistance. Numerous studies involving mathematical expressions have been performed to explain non-Newtonian fluid flow characteristics. Some commonly used models are discussed below.

Since non-Newtonian fluids are complex and their viscous effects have profound impacts on the fluid flow characteristics, it is necessary to define the paste-backfill using the appropriate non-Newtonian model.

3.2.1 POWER-LAW MODEL

The power-law model also known as the the Ostwald-de Waele relationship offers the simplest explanation to describe the behaviour of a non-Newtonian fluid. It is limited

by the range of shear rates for which it is applicable making the fitted values of k and n dependent on the shear rates. Moreover, it does not accurately predict the values of zero and infinite values of viscosity.

$$\tau = k\dot{\gamma}^n \quad (3.4)$$

$$\eta = k\dot{\gamma}^{n-1} \quad (3.5)$$

where, τ is the shear stress in Pa, k is the consistency index, $\dot{\gamma}$ is the strain gradient in s^{-1} and n is the flow behaviour index. The consistency index gives an idea of the viscosity of a fluid; the higher the value of k , the more viscous the fluid. The flow behaviour index n is a measure of the degree of deviation from Newtonian behaviour. In general, the further n departs from 1, the more pronounced the non-Newtonian properties. For n values close to 1, the fluid's behaviour shifts from shear thinning to thickening or vice versa. For $n > 1$, the fluid is shear thinning and shear thickening for $n < 1$. These relationships are summarized below in Table 3.1.

Table 3.1: Yield stress and flow behaviour index of Fluids

Fluid	Yield Stress	Flow Behaviour Index
Newtonian	$\tau_y = 0$	$n = 1$
Bingham plastic	$\tau_y > 0$	$n = 1$
Pseudoplastic	$\tau_y = 0$	$n < 1$
Dilatant	$\tau_y = 0$	$n > 1$

3.2.2 CROSS MODEL

The Cross model is commonly used to describe low and high shear rate behaviour in non-Newtonian fluids.

$$\frac{\eta - \eta_\infty}{\eta_0 - \eta_\infty} = \frac{1}{1 + k\dot{\gamma}^n} \quad (3.6)$$

where, η_0 and η_∞ are the zero and infinite shear viscosities. All the parameters involved are calculated using a curve fit. For low values of $\dot{\gamma}$, η becomes η_∞ and for intermediate values of $\dot{\gamma}$, the Cross model reduces to Power-law model. The model also exhibits a Newtonian behaviour when $k \rightarrow 0$.

3.2.3 CARREAU MODEL

The Carreau-Yasuda model is a five-parameter model that takes into account the limiting values of viscosities η_0 and η_∞ . The variation of viscosity at high shear rates can be captured using this model. Similar to the power-law model, the Carreau-Yasuda model as shown in equation (3.7) is a generalized Newtonian fluid model and unable to predict memory or other elastic effects. A model was later developed that reduced the five parameters to four by taking the value of a as 2 as shown in equation (3.8).

$$\frac{\eta(\dot{\gamma}) - \eta_\infty}{\eta_0 - \eta_\infty} = [1 + \lambda' \dot{\gamma}^a]^{\frac{n-1}{a}} \quad (3.7)$$

$$\frac{\eta(\dot{\gamma}) - \eta_\infty}{\eta_0 - \eta_\infty} = [1 + \lambda' \dot{\gamma}^2]^{\frac{n-1}{2}} \quad (3.8)$$

3.2.4 HERSCHEL-BULKLEY AND BINGHAM MODELS

A Bingham plastic fluid is characterized by a flow curve which is a straight line having an intercept τ_y on the shear stress axis as shown in figure 3.1. The yield stress τ_y is the minimum stress that is required to cause the fluid to flow like a viscous material with a finite viscosity. When the stress applied to the fluid is lesser than the critical yield stress

of the material, then the fluid does not flow but deforms plastically like a solid and upon removal of the stress the material regains its initial state.

A generalized model was proposed by (Herschel & Bulkley, 1926) to characterize the relationship between shear stress and shear rate by the introduction of three parameters, consistency index, flow behaviour index and yield stress. The knowledge of yield stress then leads to quantifying the amount of shear stress the fluid requires prior to yielding. The plastic viscosity of the herschel-bulkley fluid is obtained by dividing the equation (3.9) by the strain gradient $\dot{\gamma}$.

$$\tau = \tau_y + k\dot{\gamma}^n \quad \text{for } |\tau| > \tau_y, \quad (3.9)$$

$$\eta = \frac{\tau_y}{\dot{\gamma}} + k\dot{\gamma}^{n-1} \quad \text{for } |\tau| > \tau_y, \quad (3.10)$$

In equations (3.9) and (3.10), if $n=1$ is substituted as the value of the flow behaviour index, we arrive at the Bingham plastic model as proposed by (Bingham, 1922). The Bingham fluid is to some extent an idealized case. It is a fluid that requires a finite shearing stress to initiate motion and for which there exists a linear relationship between the shearing stress in excess of the initiating and the resulting velocity gradient (Govier et al., 1973).

$$\tau = \tau_y + k\dot{\gamma} \quad \text{for } |\tau| > \tau_y, \quad (3.11)$$

$$\eta = \frac{\tau_y}{\dot{\gamma}} + k \quad \text{for } |\tau| > \tau_y, \quad (3.12)$$

3.3 NON-NEWTONIAN FLUID PROPERTIES

The determination of yield stress and consistency index of a Bingham plastic fluid is critical in understanding the flow behaviour of backfill. They can be determined using viscometers. Experiments require a carefully controlled laboratory environment.

3.3.1 SLUMP TEST

The slump test is an experiment generally used to determine the workability of fresh concrete. Workability is a property that represents the amount of work which is to be done to compact the concrete in a given mould and it is affected by factors such as water content, aggregate size and composition. Yield stress of the backfill is obtained from a slump test performed using a metal conical frustrum and a cylindrical PVC boger. The slump cone used adheres to ASTM C143 standard (ASTM C143 / C143M-15a, 2015). The cone is made out of metal that is not readily affected by backfill paste. The cone has a height of 300 mm, top diameter of 100 mm and base diameter of 200 mm (ASTM C143 / C143M-15a, 2015). The PVC boger has a height of 152.4 mm and a diameter of 152.4 mm. Both moulds are checked for mismatches with the prescribed dimensions. It is ensured that the setup is free of dents, deformations or material stuck from previous trials. Figures 3.2 and 3.3 show the schematic arrangement of the initial and final stress distributions in the cylindrical boger and conical C143 slump tests.

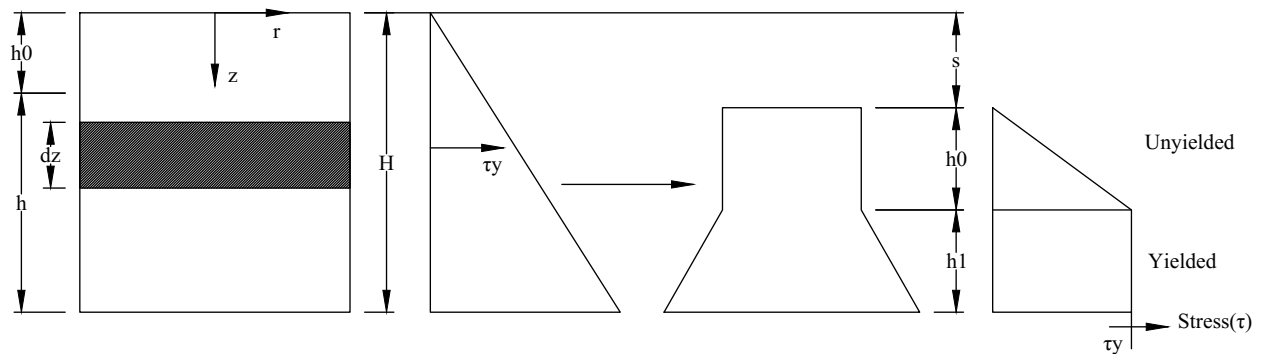


Figure 3.2: Schematic arrangement showing the initial and final stress distribution of the cylindrical boger slump test (Pashias et al., 1996)

where, dz is element thickness, h is total final height, H is total height of slump mould,

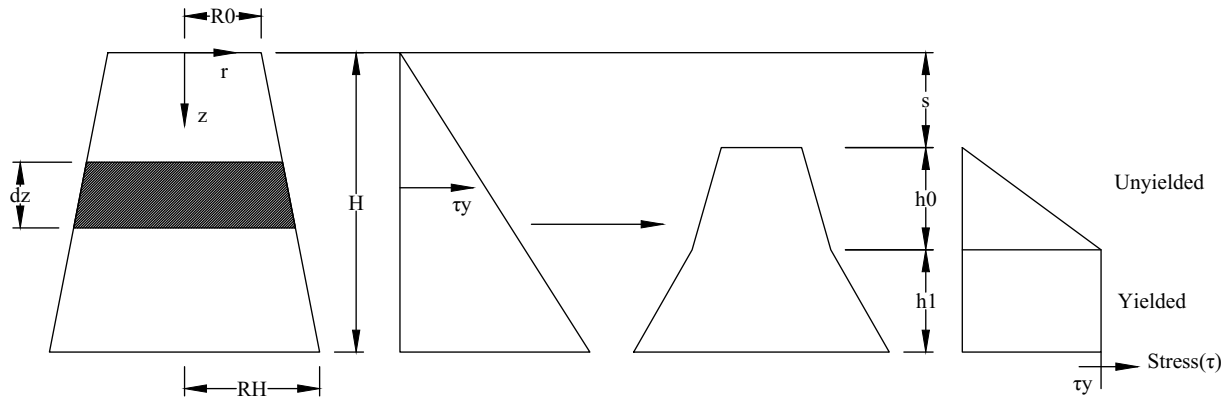


Figure 3.3: Schematic arrangement showing the initial and final stress distribution of the conical C143 slump test (Schowalter & Chrsitensen, 1998)

h_0 is yielded region height, h_1 is un-yielded region height, s is slump height, R_0 is slump cone top radius and R_H is slump cone bottom radius.

The inside of the moulds are covered with a thin layer of lubricant that will prevent rusting due to backfill and water. It is placed on top of a flat, rigid and non-absorbent surface that has been cleaned prior to the commencement of the test. It is held firmly in place as the prepared backfill samples are poured into the mould cavity slowly. After one thirds of the cavity is filled, a tamping rod longer than the maximum height of the mould is taken and dipped into the backfill a minimum of 25 times uniformly over the cross section. This ensures the uniform settling of the paste inside the mould cavity and removes air bubbles if any. The same process is repeated after two thirds of the cavity is filled and finally after filling the entire volume. If some paste subsides due to the rodding process, extra material is added till the top of the mould. The mould is now steadily raised off the flat surface vertically without any torsional or lateral motion. The mould needs to be raised high enough beyond the original height of the mould from the surface allowing the material to collapse under its own weight, and is placed beside the slumped material. The slump height of the paste is thn measured from the top of the mould to the top surface of the slumped specimen.

Slump heights obtained from the experiment are converted into dimensionless forms with the use of arithmetic relations laid forth by (Pashias et al., 1996) for the slump cylinder test as shown in equation 3.13 and (Schowalter & Christensen, 1998) for the ASTM C143

test as shown in equation 3.14.

$$s' = 1 - 2\tau_y' [1 - \ln(2\tau_y')] \quad (3.13)$$

$$s' = 1 - h_0' - h_1' = 1 - h_0' - 2\tau_y' \ln \left[\frac{3}{(1 + h_0')^3 - 1} \right], \quad (3.14)$$

Where, s' is dimensionless slump height, τ_y' is dimensionless yield stress, h_0' is dimensionless yielded region height and h_1' is dimensionless unyielded region height. Figure 3.4 shows the relationship between dimensionless yield stress and dimensionless slump. A magnified portion of the graph shows the results from the slump tests. The focus is on high solid fraction paste backfill. The dimensionless approach standardizes equations making them independent of variables and easy to scale. A decrease in dimensionless slump height with increase in dimensionless yield stress holds in good agreement with the general understanding that yield stress is inversely proportional to slump height. There is good agreement between the experimental slump results and the analytical solution developed by (Roussel & Coussot, 2005), particularly in the case of the cylinder slump. The dimensional yield stress for ASTM slump test slightly deviates from analytical solution. This can be adequately explained by the fact that the analytical solution for yield stress proposed by the author was originally derived for concrete while our experiment focusses on paste backfill of mine tailing and water.

3.3.2 CUP AND BOB VISCOMETER

In addition to the slump test, yield stress of the backfill samples may be experimentally measured using a viscometer. The method of estimation is distinct and changes with the attachments. The yield stress τ_y and the consistency index k are determined experimentally using a cup and bob viscometer. The inner cylinder (bob) is rotated via a spindle inside an outer container (cup) whose dimensions adhere to (ISO 3219, 1993).

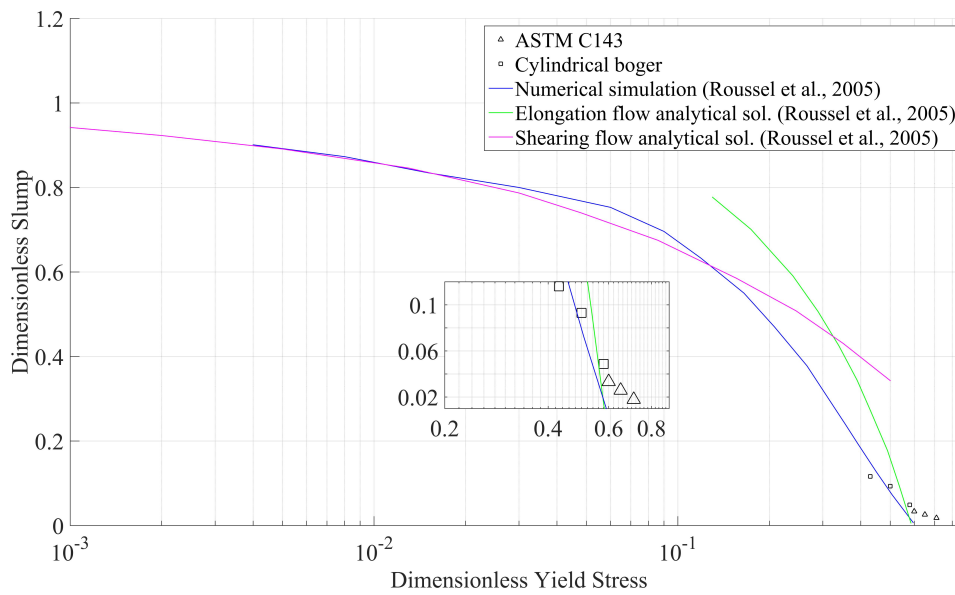


Figure 3.4: Dimensionless slump height as a function of dimensionless yield stress. The viscometer setup is shown below in figures 3.5 and 3.6. The backfill material is filled in the gap between the cup and bob. A torque is induced in the spindle and the bob is allowed to rotate causing shear in the material trapped between the two cylinders. The shear stress τ is calculated from the torque M and radius of the bob R_i while the shear rate $\dot{\gamma}$ is calculated from the rotational speed n' (ISO 3219, 1993).



Figure 3.5: Bob attachment in the viscometer for yield stress and consistency index measurement

$$\tau = \frac{0.0446M}{R_i^3} \quad (3.15)$$



Figure 3.6: Cup and bob attachment with outer jacket for water circulation

$$\dot{\gamma} = 1.291n', \quad (3.16)$$

Tailings from the mine and water are mixed in a vessel using handheld and stationary mixers to obtain the backfill test material. The tests are conducted for a range of 5 solid percentages each at three different temperatures on HAAKE Viscotester 550 that is connected to a computer with an installed program to interpret the results. The tests are conducted for a shear rate of 0 - 220 s^{-1} and the relationship of shear stress with shear rate and viscosity with shear rate are obtained. Water at three different temperatures is circulated around the cup inside a cover jacket with the help of tubes. The temperature is measured regularly using thermometers to ensure it is constant during the experiment. The trials are repeated three times for each solid percentage at each temperature and the results are recorded in the system. Using equations (3.11), (3.12), (3.15) and (3.16) the Bingham yield stress and plastic viscosity values are obtained for the various solid percentages and the results are fitted on to a curve as shown below in figures 3.7-3.12. An increase in yield strength and consistency index with increase in solid percentage is

seen owing to the increase in particle-particle interaction.

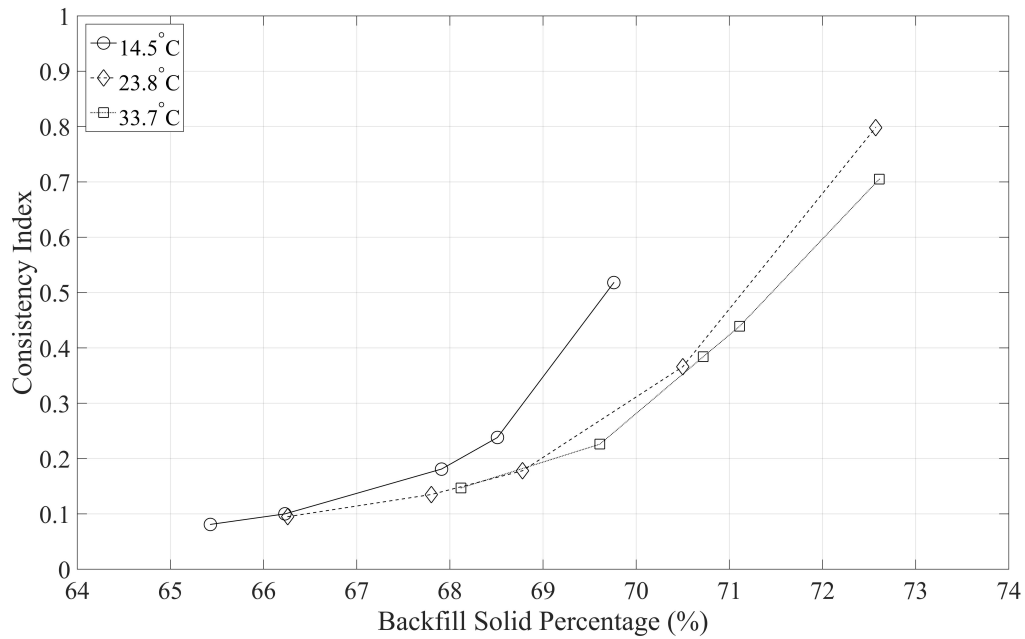


Figure 3.7: Mine-A consistency index at three different temperatures

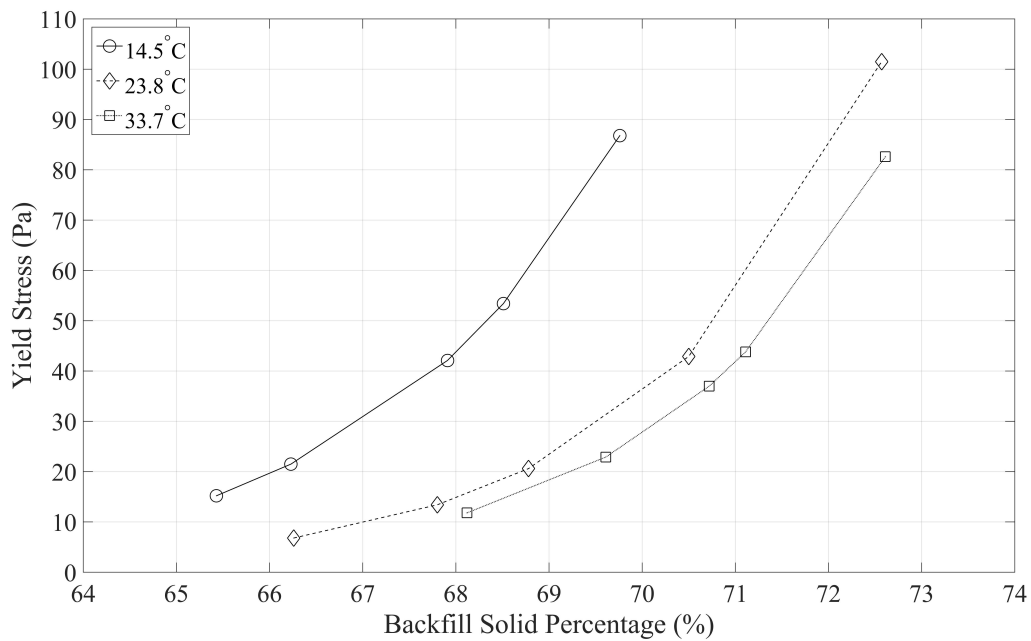


Figure 3.8: Mine-A yield stress at three different temperatures

3.3.3 VANE RHEOMETER

A vane attachment as shown below in Figure 3.13 is used to avoid wall slip due to the displacement of the disperse phase away from the solid boundaries (Saak et al., 2004).

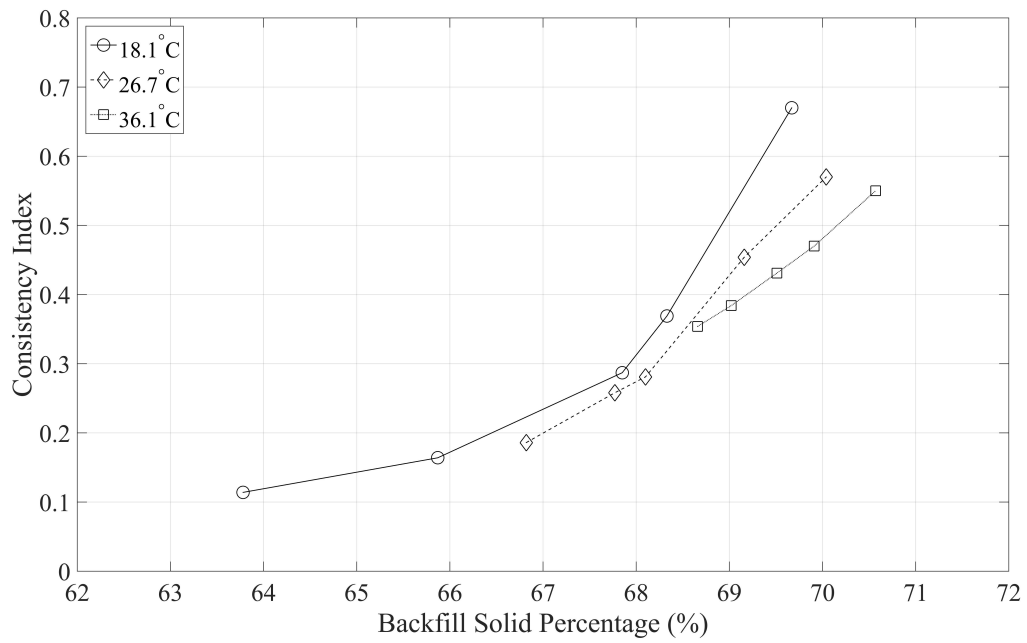


Figure 3.9: Mine-B consistency index at three different temperatures

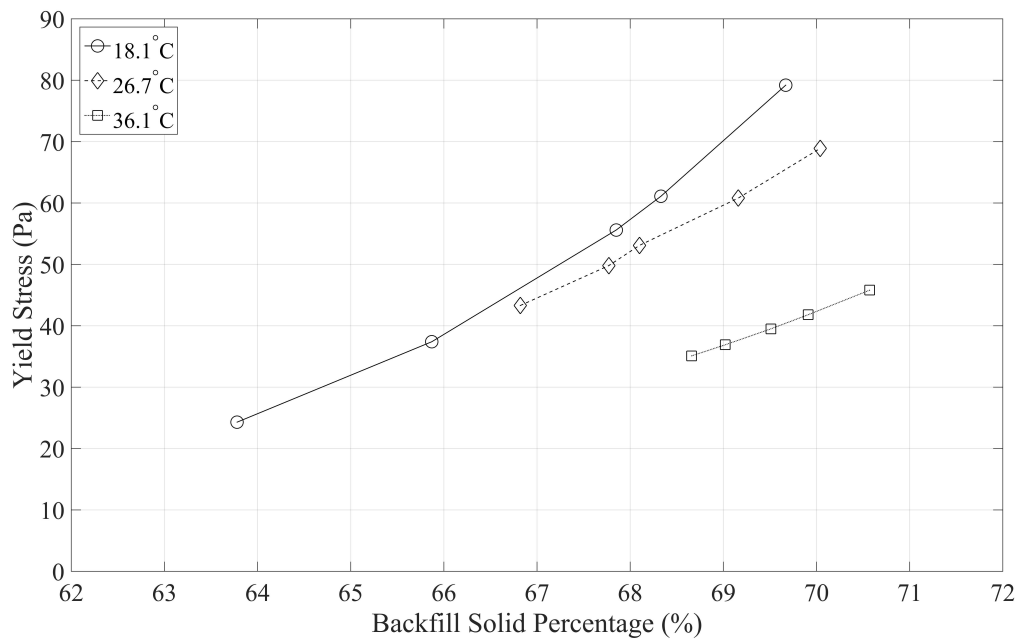


Figure 3.10: Mine-B yield stress at three different temperatures

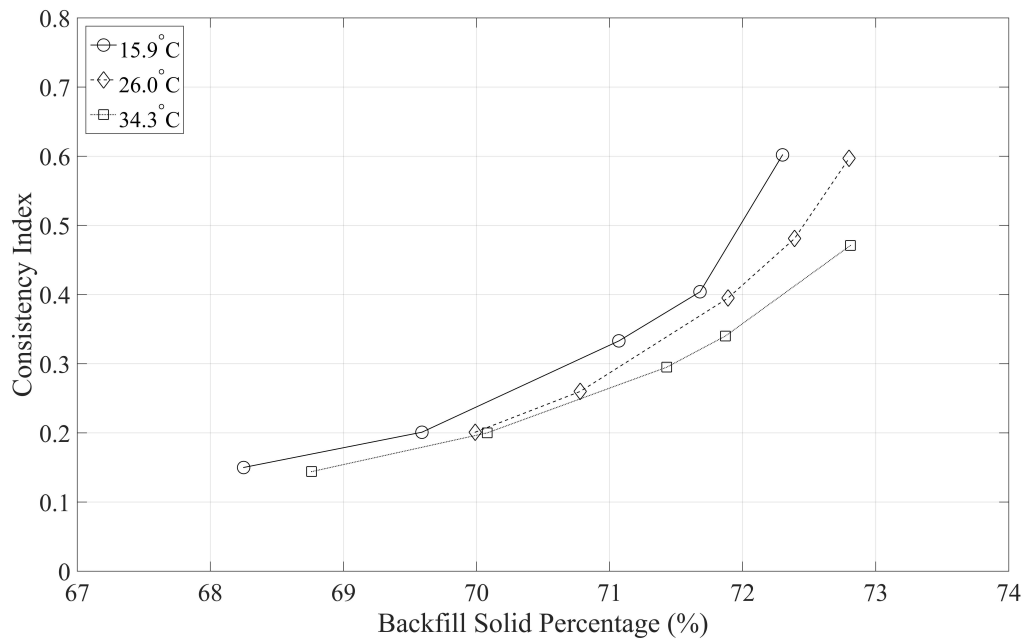


Figure 3.11: Mine-C consistency index at three different temperatures

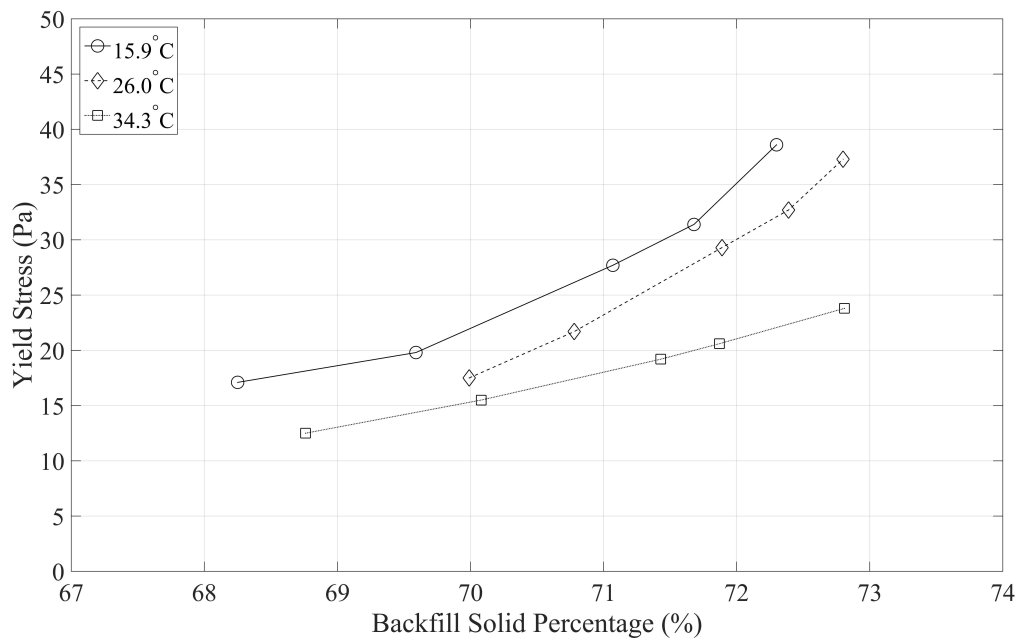


Figure 3.12: Mine-C yield stress at three different temperatures

The vane is inserted into a container holding the test sample with little disturbance to the structure of the sample. The radius of the vane R_i should be lesser than the radius of the container R_o in accordance to the relationship mentioned below in equation (3.17). Similar to the cup and bob method, the shear rate is ramped up from 0 to 220 s^{-1} and the relationship of shear stress with shear rate is obtained.



Figure 3.13: Vane attachment in the rheometer for yield stress measurement

$$R_o > R_i \left(\frac{\tau_y}{\tau_{w'}} \right)^{0.5} \quad (3.17)$$

The standard method employed for measuring the yield stress and consistency index is by fitting models to the measured rheograms obtained from the rheometers. The Bingham model discussed above is employed to describe the behaviour of the non-Newtonian paste backfill. Extrapolation of the shear stress - shear rate rheogram to zero shear rate is a common method employed to determine the yield stress of a non-newtonian fluid. The rheogram obtained from 70% solid concentration of Mine-A tailings in water at three different temperatures is shown below in Figure 3.14.

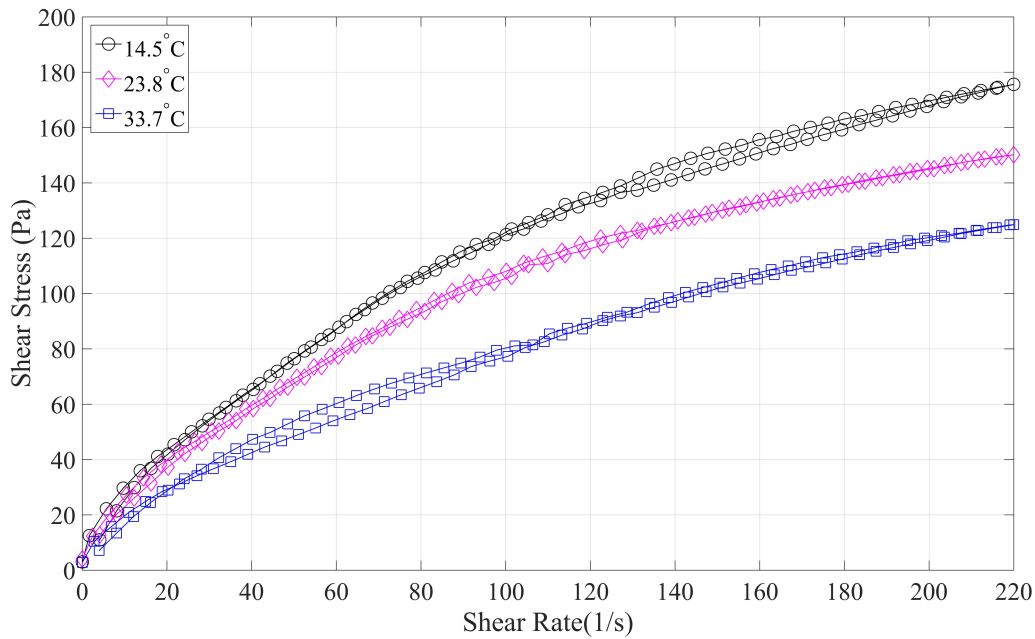


Figure 3.14: Rheogram of 70% solid concentration of Mine-A tailings in water at three different temperatures

3.3.4 ARRHENIUS RELATIONSHIP - TEMPERATURE DEPENDENT PROPERTIES

The rates of chemical reactions are governed by the addition of and removal of heat. With increase in temperature, molecules move faster and collide producing enough energy to increase the rate of chemical reactions and the reverse holds true for decrease in temperature. Swedish scientist Svante Arrhenius postulated the Arrhenius equation (Arrhenius, 1889) wherein lies the dependence of rate constant k of a chemical reaction on the absolute temperature T , where A' is a pre-exponential factor, E_a is the activation energy and R is the universal gas constant. Equation (3.18) below shows the Arrhenius equation.

$$k = A' \exp\left(\frac{-E_a}{RT}\right) \quad (3.18)$$

Activation energy is the minimum energy required in a chemical reaction for reactants to react and form a product. The term RT refers to the average kinetic energy of the

molecules and thus the exponent is a ratio of activation energy to average kinetic energy. It can be inferred from equation (3.18) that either increasing the temperature or decreasing the rate of reaction by addition of external agents such as catalysts can increase the rate of reaction. Equation (3.18) may be re-written as shown below with a constant α , which is the ratio of activation energy E_a to universal gas constant R .

$$k = A' \exp\left(\frac{-\alpha}{T}\right) \quad (3.19)$$

Activation energy may be determined either by plotting graphs or experimentally. In the first method, the equation (3.19) is re-written by taking logarithms on both sides.

$$\ln k = \ln A' + [-\alpha] \left[\frac{1}{T} \right] \quad (3.20)$$

The above (3.20) is in the form of an equation of a straight line, $y = mx + b$ where by plotting $\ln k$ as a function of $1/T$, the slope α is obtained. (3.20) may be re-written for a case where experiments have been done at two different temperatures T_1 and T_2 yielding two rate constants k_1 and k_2 respectively.

$$\ln k_1 = \ln A' + [-\alpha] \left[\frac{1}{T_1} \right] \quad (3.21)$$

$$\ln k_2 = \ln A' + [-\alpha] \left[\frac{1}{T_2} \right] \quad (3.22)$$

Subtracting (3.21) from equation (3.22) eliminates the pre-exponential factor A' and gives the value of the constant α and from that the activation energy.

$$\ln k_2 - \ln k_1 = \left[\ln A' - \frac{\alpha}{T_2} \right] - \left[\ln A' - \frac{\alpha}{T_1} \right] \quad (3.23)$$

$$\ln k_2 - \ln k_1 = \alpha \left[\frac{1}{T_2} - \frac{1}{T_1} \right] \quad (3.24)$$

$$\alpha = \frac{\ln \frac{k_2}{k_1}}{\left[\frac{1}{T_2} - \frac{1}{T_1} \right]} \quad (3.25)$$

In the second method, the natural logarithm of the consistency index, $\ln(k)$ is plotted on the y axis against the inverse of the temperature, $(1/T)$ for which they are measured in the x axis. For each solid percentage a linear regression is used by taking $(1/T)$ as the explanatory variable and $\ln(k)$ as the dependent variable. This is shown below in Arrhenius plots for Mine-A, Mine-B and Mine-C in Figures 3.15, 3.16 and 3.17 respectively.

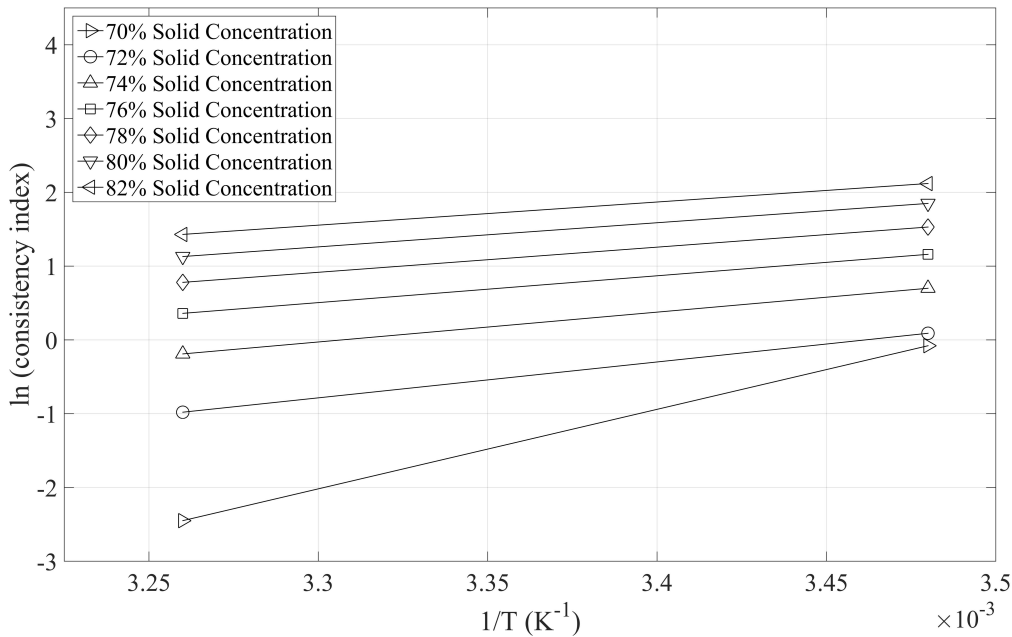


Figure 3.15: Arrhenius plot for Mine-A

The constant α obtained is negative as seen in Figures 3.15, 3.16 and 3.17. This is due to the reduction in consistency index with an increase in temperature producing a positive slope. By multiplying α with the universal gas constant R , the activation energy E_a is obtained and is plotted below in Figure 3.18. From (3.18) it is evident that for high values of E_a and thus α the consistency index will increase. The higher activation energy for Mine-C followed by Mine-A and Mine-B indicates the less effect temperature has on their respective consistency indices which is highest for Mine-B then for Mine-A and finally for

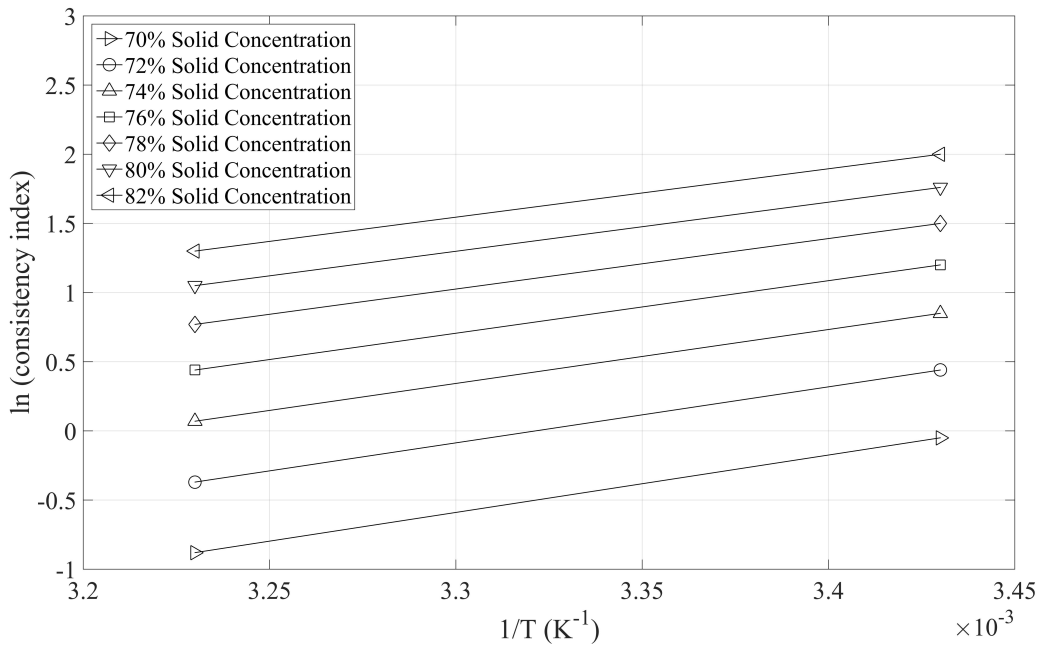


Figure 3.16: Arrhenius plot for Mine-B

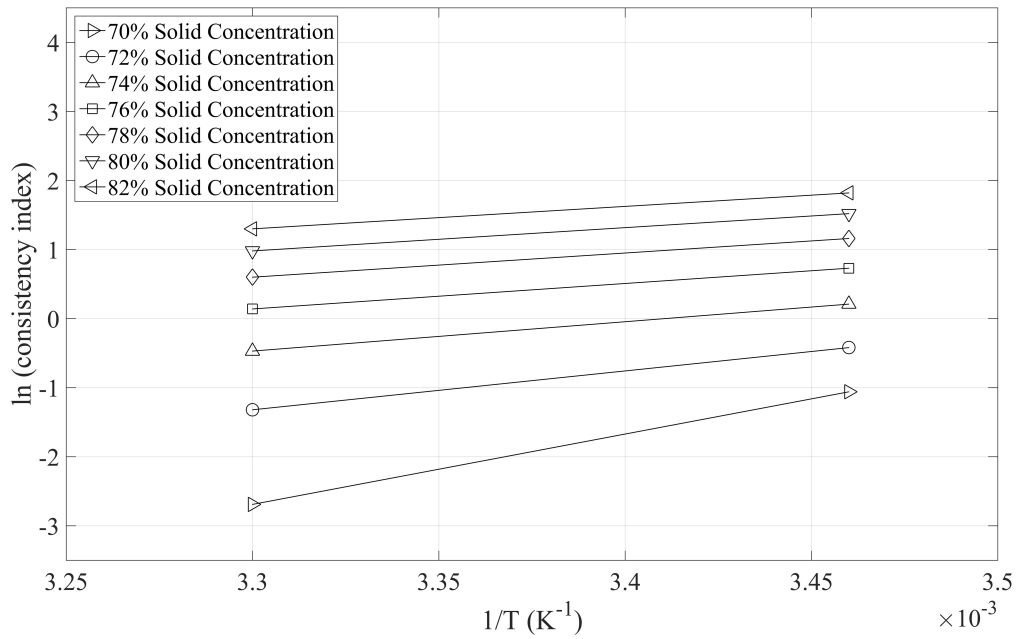


Figure 3.17: Arrhenius plot for Mine-C

Mine-C. The activation energy reduces with an increase in solid percentage for all mines. Mine-A sees a 58% drop in activation energy, Mine-B sees a 15% drop while Mine-C sees a 68% drop.

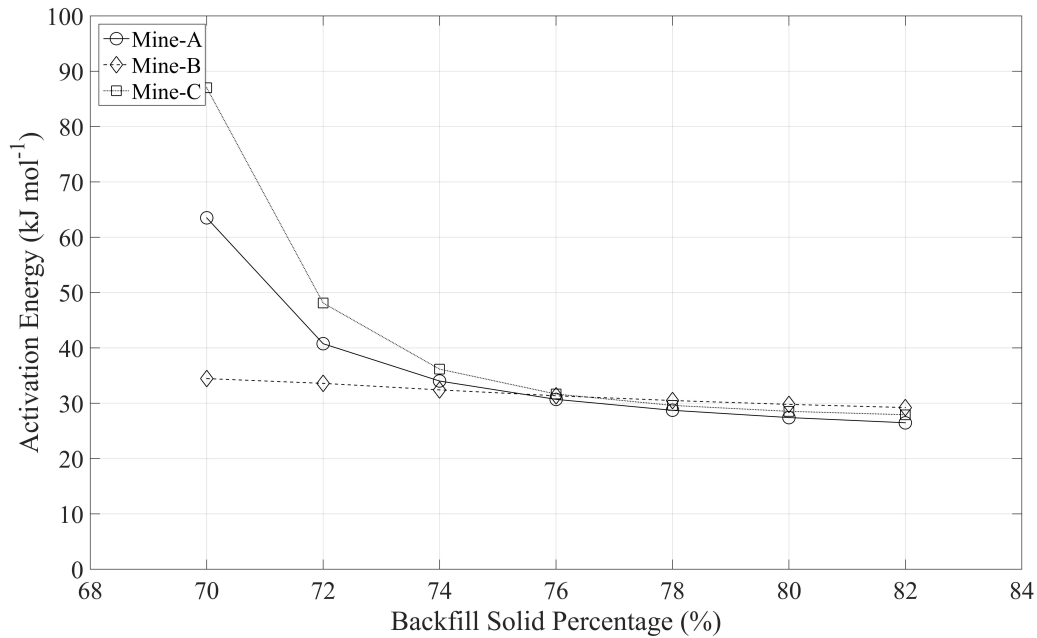


Figure 3.18: Activation energies in Mine-A, Mine-B and Mine-C tailings-water mixture. The non-Newtonian Bingham plastic model discussed earlier can be re-written with the effect of temperature dependent viscosity. The Arrhenius equation is used to model the strong viscosity-temperature relationship of the paste backfill (Giap 2010; Wu et al. 2013; Balmforth and Caster 2001; Li and Zhang 2003). This form is represented below in (3.26).

$$\eta = A' \exp\left(\frac{-\alpha}{T}\right) \quad (3.26)$$

By following the same method for determining the plastic viscosity as rate constant from (3.18) to (3.27) we arrive at the relationship between constant α , viscosity η and the testing temperatures.

$$\alpha = \frac{\ln \frac{\eta_2}{\eta_1}}{\left[\frac{1}{T_2} - \frac{1}{T_1}\right]} \quad (3.27)$$

ANSYS Fluent incorporates a temperature dependency $H(T)$ that is derived from the

Arrhenius law to the non-Newtonian viscosity term. The equation (3.12) detailed above is modified to equation (3.28).

$$\eta = \left(\frac{\tau_y}{\dot{\gamma}} + k \right) H(T) \quad (3.28)$$

$$H(T) = \exp \left[\alpha \left(\frac{1}{T - T_0} - \frac{1}{T_\alpha - T_0} \right) \right] \quad (3.29)$$

where, T_α is a reference temperature for which $H(T) = 1$, T_0 is the temperature shift corresponding to the lowest thermodynamically possible temperature. For $\alpha = 0$, the temperature dependence is ignored.

3.3.5 THERMAL PROPERTIES

The thermal conductivity and specific heat capacity of the backfill are critical in understanding its heat transfer capabilities. A high thermal conductivity value permits a high rate of heat transfer across the material than a low thermal conductivity value. The specific heat capacity on the other hand determines the amount of heat required per unit mass of material to increase the temperature by one unit of temperature. Figures 3.19 and 3.20 display the thermal conductivities and specific heat capacities of the three mines under study. The individual properties of each component making up the mine tailings is obtained and the properties of the entire mixture for given solid percentages is obtained by a similar approach adopted for density explained in (3.2). There is an increase in thermal conductivity and a decrease in specific heat capacity with solid percentage. This is an indication of the effect solid percentage has on heat transfer. Temperature dependent rheological properties used in this thesis are critical in heat transfer analysis of viscoplastic fluids adding a complexity to the momentum and energy balance equations (Labsi et al., 2015). A strong temperature-viscosity relationship results in strong coupling of these two equations.

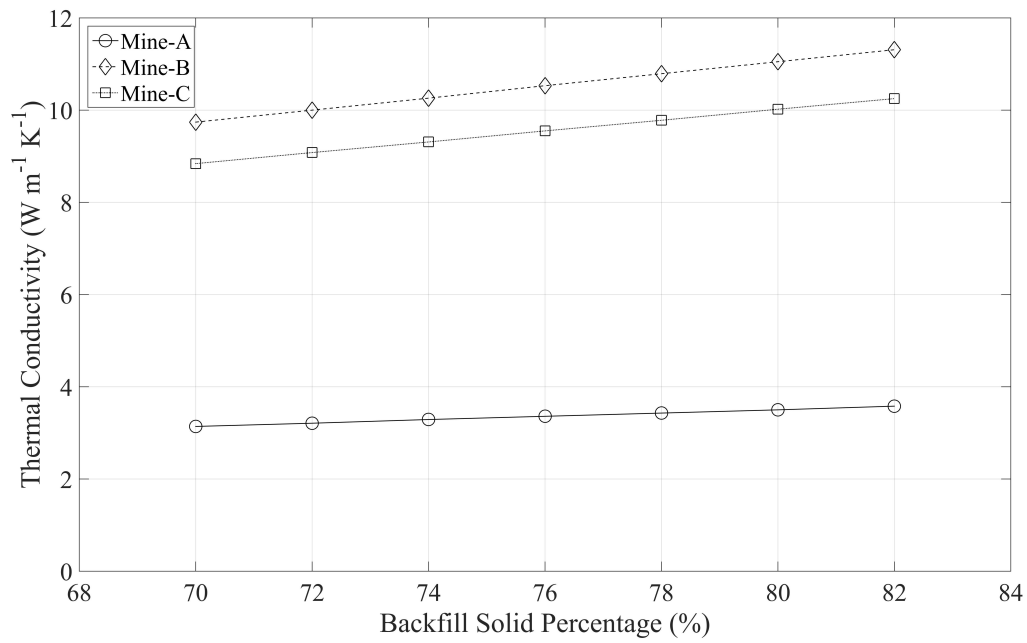


Figure 3.19: Thermal conductivities of Mine-A, Mine-B and Mine-C backfill

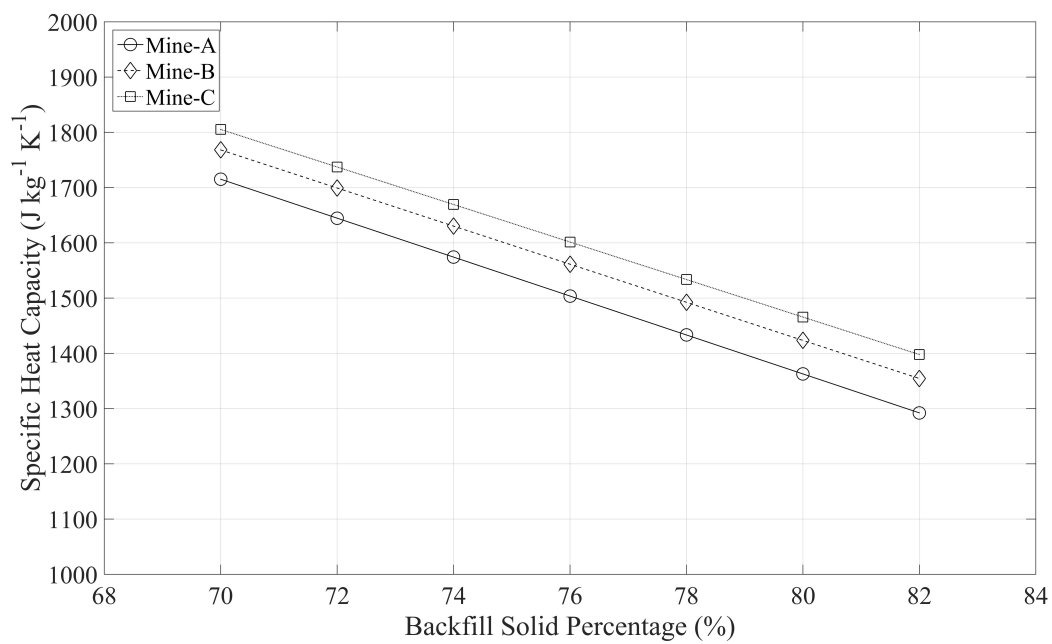


Figure 3.20: Specific heat capacities of Mine-A, Mine-B and Mine-C backfill

4 NUMERICAL MODELLING

Multiphase flows are a fluid flow system consisting of two or more distinct phases or components flowing simultaneously in mixture, having some level of phase separation at a scale well above the molecular level. Liquid-solid flows deal with a suspended solid in the liquid phase. The density of the particulate phase characterizes the flow as either dense or dilute. In a liquid-particle flow, both the liquid and solid phases are primarily driven by the pressure gradients due to the difference in the density ratios and significantly high drag between them (Yeoh & Tu, 2009). During flow through pipes, the motion of the particles following impact on the pipe walls is different from flow in an unbounded domain. In a liquid-solid multiphase flow the particulate phase is referred as the dispersed or discrete phase and the liquid phase as the continuous phase. Few liquid-solid multiphase flows that are often encountered are:

- Blood flow.
- Transportation of sediment and soil by rivers.
- Slurry and sewage transportation.

The complex nature of multiphase flows and the interaction between the various phases are difficult to understand and a need to model and predict their behavior arises. Laboratory experiments have certain limitations; it is difficult to artificially recreate real-life processes in a controlled environment. This magnifies when a large process is scaled down to accommodate in to a laboratory environment. The scale-down restricts the reliability of the extrapolation of the results. To overcome these restraints, computational models are developed and validated through experimental data. Available computational technologies make it possible to solve transport equations governing mass, momentum and energy conservations for all phases of a multiphase flow at the same time tracking the position of particles. Owing to the ability to control experimental variables with comparative ease

and produce accurate predictions, computational fluid dynamics is being increasingly adopted to simulate multiphase flows.

Dispersed flows are generally treated using the trajectory models or the two-fluid models. In trajectory models, the motion of the dispersed phase is determined by following either the motion of the actual particles or that of larger representative particles. The details of flow around each particle encompasses the assumption that the drag, lift and moment forces acting on it alter its trajectory. In addition to this the thermal history of the particles can be tracked using this model. In the two-fluid models also known as Eulerian-Eulerian approach, the dispersed phase is treated as a second continuous phase in addition to the primary continuous phase with which it is considered to interact and generalized Navier-Stokes equations are solved for both phases. Each phase occupies a volume giving rise to the concept of phasic volume fraction. These volume fractions are assumed to be continuous functions of space and time and their sum is equal to one. The Eulerian model solves a set of n governing equations for each phase and coupling is achieved through the pressure and inter-phase exchange coefficients. This model neglects the discrete nature of the dispersed phase enabling the use of an averaging process to derive the effective conservation equations and characterize the properties of the dispersed phase. When the fluid moves these conservation laws need to be satisfied.

4.1 EULERIAN-LAGRANGIAN

The Eulerian-Lagrangian approach also known as Trajectory Model has the fluid medium as the continuous phase and the dispersed particles as the discrete phase. This model is commonly used in rheological studies of granular flows. In this framework, the fluid is treated as the continuum by solving time averaged Navier-Stokes equations while the motion of the discrete phase is determined by following either the motion of the actual particles or the motion of larger representative particles through a calculated flow field. For each representative particle stream, the mass, momentum and energy equations

are solved for the determination of its location and properties. There is interaction between the two phases and exchange of mass, momentum and energy. The Eulerian-Lagrangian framework permits one-way, two-way and four-way coupling by the inclusion of appropriate interaction terms in the continuous phase equations. Depending on the volume fraction of the discrete phase and the way the particle-particle collisions and interaction between phases are modelled, there are different Eulerian-Lagrangian methods employed.

4.1.1 DISCRETE PHASE MODEL

An important assumption in this model is that the dispersed phase is sufficiently dilute so that the particle-particle interactions and the effects of the particle volume fraction on the continuous phase are limited. Although, a high mass loading is permitted there is a limitation on the volume fraction of dispersed phase which should not exceed 10% (“ANSYS Fluent Theory Guide”, 2015). ANSYS Fluent solves the equations of motion of the discrete phase model using transient numerical methods and it has provisions to solve particle trajectory calculations using both steady and unsteady solvers. The particle treatment is independent of the continuous phase treatment and a steady or unsteady solver may be used regardless of the solver used for the continuous phase (“ANSYS Fluent Theory Guide”, 2015). In steady particle tracking, the the particle is tracked immediately from release till it reaches its final destination. Each particle is simulated in a coupled or decoupled manner where it travels through the fluid changing the DPM sources in each cell. In unsteady particle tracking depending on the steady or unsteady treatment of continuous phase the particle time step size, number of time steps and fluid flow time step sizes determine the interval at which the particles are injected. In all cases the particles are tracked in accordance to the continuous phase solver. This method gives an additional flexibility with the ability to control the injection start and stop time with respect to the start of the calculation. The standard form of the mass and momentum conservation equations are written below in equations (4.1) and (4.2) (“ANSYS Fluent Theory Guide”,

2015).

$$\frac{\partial \rho}{\partial t} + \nabla \cdot (\rho \vec{u}) = 0 \quad (4.1)$$

$$\frac{\partial \rho \vec{u}}{\partial t} + \nabla \cdot (\rho \vec{u} \vec{u}) = -\nabla p + \nabla \cdot \tau + \rho \vec{g} + \vec{F}_{DPM} \quad (4.2)$$

The trajectory of a discrete phase particle is predicted by the integration of the force balance on the particle written in a Lagrangian frame of reference. The force balance equates the inertia of a discrete phase particles with the forces acting on the particle and is written below in equation (4.3). On the right hand side the first term denotes the drag force per unit particle mass and the second term denotes the effect of gravity.

$$\frac{d\vec{u}_s}{dt} = F_D (\vec{u}_p - \vec{u}_s) + \frac{\vec{g}(\rho_s - \rho_p)}{\rho_s} \quad (4.3)$$

The drag factor F_D is defined below in equation (4.4). The coefficient of drag C_D is modelled based on the drag law correlation developed by (Haider & Levenspiel, 1989) for non-spherical particles with a shape factor of 0.8.

$$F_D = \frac{18\mu_c C_D Re}{24\rho_s d_s^2} \quad (4.4)$$

where, μ_c is the molecular viscosity of the fluid and Re is the relative Reynolds number.

4.1.2 DENSE DISCRETE PHASE MODEL

The treatment of the continuous phase and dispersed phase in dense discrete phase model is similar to that in discrete phase model and is employed for solving flows with high solid concentrations. In liquid-solid flows where the solid phase is taken to be granular

the properties are derived from the Kinetic Theory of Granular Flow (KTGF). KTGF creates an analogy between the granular phase and the kinetic theory of dense gases. The derivation of the equations of motion and KTGF is done by an averaging process (Jenkins & Savage, 1983) (Lun, Savage, Jeffrey, & Chepurniy, 1984) (Ding & Gidaspow, 1990) (Hiltunen et al., 2009) (“ANSYS Fluent Theory Guide”, 2015) and are written below from equations (4.5) to (4.21). The equations have been derived for a case of one solid phase dispersed in a continuous phase. A general assumption while deriving the equations for multiphase flow is the adoption of an infinitesimal volume in the flow field that is both very much smaller than the typical distance over which the flow properties vary significantly and very much larger than the size of the individual dispersed particles. However, in the treatment of multiphase flows, both of the above mentioned conditions are very rarely satisfied (Brennen, 2005), necessitating the need for an averaging method such as time, volume or ensemble. The equations below are obtained by volume averaging which provides an intuitive and straightforward interpretation of the interaction terms and dynamic quantities at the same time illustrating potential problems common to all averaging methods (Hiltunen et al., 2009).

1. The continuity equation for any phase p is written as:

$$\frac{\partial}{\partial t}(\alpha_p \rho_p) + \nabla \cdot (\alpha_p \rho_p \vec{u}_p) = 0 \quad (4.5)$$

2. The continuity equation for any phase s is written as:

$$\frac{\partial}{\partial t}(\alpha_s \rho_s) + \nabla \cdot (\alpha_s \rho_s \vec{u}_s) = 0 \quad (4.6)$$

where, α is the phase volume fraction, u is the velocity, and ρ is the density. The subscripts p and s denote the two phases paste and solid respectively and m characterizes the mass transfer between them.

3. The momentum equation for phase p is written as:

$$\begin{aligned} \frac{\partial}{\partial t}(\alpha_p \rho_p \vec{u}_p) + \nabla \cdot (\alpha_p \rho_p \vec{u}_p \vec{u}_p) = & -\alpha_p \nabla p + \nabla \cdot \bar{\bar{\tau}}_p + \alpha_p \rho_p \vec{g} \\ & + \sum_{p=1}^n (\vec{K}_{sp}) + (\vec{F}_b + \vec{F}_{lift}) \end{aligned} \quad (4.7)$$

The momentum equation for phase s is written as:

$$\begin{aligned} \frac{\partial}{\partial t} (\alpha_s \rho_s \vec{u}_s) + \nabla \cdot (\alpha_s \rho_s \vec{u}_s \vec{u}_s) = & -\alpha_s \nabla p + \nabla \cdot \bar{\bar{\tau}}_s + \alpha_s \rho_s \vec{p} \\ & + \sum_{p=1}^n (\vec{K}_{ps}) + (\vec{F}_b + \vec{F}_{lift}) \end{aligned} \quad (4.8)$$

where, p is the solid pressure, K_{pq} is the momentum exchange coefficient between the continuous phase and the discrete phase. $\bar{\bar{\tau}}_p$ and $\bar{\bar{\tau}}_s$ are the p^{th} and s^{th} phase stress tensor and they are expressed below in equation (4.9) and (4.10).

$$\bar{\bar{\tau}}_p = \alpha_p \mu_p \left(\nabla \vec{u}_p + \nabla \vec{u}_p^T \right) + \alpha_p \left(\lambda_p - \frac{2}{3} \mu_p \right) \nabla \cdot \vec{u}_p \bar{\bar{I}} \quad (4.9)$$

$$\bar{\bar{\tau}}_s = \alpha_s \mu_s \left(\nabla \vec{u}_s + \nabla \vec{u}_s^T \right) + \alpha_s \left(\lambda_s - \frac{2}{3} \mu_s \right) \nabla \cdot \vec{u}_s \bar{\bar{I}} \quad (4.10)$$

where, μ and λ are the shear and bulk viscosities of the phases p and s , $\bar{\bar{I}}$ is the unit tensor, \vec{F}_b is the external body force and \vec{F}_{lift} is the lift force. The inter-phase momentum transfer coefficient can also be expressed in terms of mean inter-phase momentum transfer coefficient and phase velocities as shown below in equation (4.11).

$$\sum_{p=1}^n \vec{K}_{ps} = \sum_{p=1}^n K_{ps} (\vec{u}_p - \vec{u}_s) \quad (4.11)$$

The trajectory of the discrete phase in DDPM is computed in a similar manner to DPM. An additional term F_{int} is added to the force balance equation (4.3) that models the acceleration acting on a discrete phase particle from inter-particle interactions. F_{int} is computed from the stress tensor given by the kinetic theory of granular flows (KTGF) and is written below in (4.13).

$$\frac{d\vec{u}_s}{dt} = F_D (\vec{u}_p - \vec{u}_s) + \frac{\vec{g} (\rho_s - \rho_p)}{\rho_s} + F_{int} \quad (4.12)$$

$$F_{int} = -\frac{1}{\rho_s} \nabla \cdot \bar{\bar{\tau}}_s \quad (4.13)$$

The solid stress tensor $\bar{\bar{\tau}}_s$ is given by the Kinetic Theory of Granular Flow. It contains shear and bulk viscosities arising from particle momentum exchange due to translation and collision. A frictional component of viscosity is also included to account for the viscous-plastic transition that occurs when particles of a solid phase reach the maximum solid volume fraction. These collisional, kinetic and frictional parts are added to give the solids shear viscosity.

$$\mu_s = \mu_{s,coll} + \mu_{s,kin} + \mu_{s,fr} \quad (4.14)$$

The collisional component is modelled as per (Gidaspow et al., 1991):

$$\mu_{s,coll} = \frac{4}{5} \alpha_s \rho_s d_s g_{0,ss} (1 + e_{ss}) \left(\frac{\Theta_s}{\pi} \right)^{1/2} \alpha_s \quad (4.15)$$

The kinetic component is modelled as per (Gidaspow et al., 1991):

$$\mu_{s,kin} = \frac{10 \rho_s d_s \sqrt{\Theta_s \pi}}{96 \alpha_s (1 + e_{ss}) g_{0,ss}} \left[1 + \frac{4}{5} g_{0,ss} \alpha_s (1 + e_{ss}) \right]^2 \alpha_s \quad (4.16)$$

The granular bulk viscosity accounts for the resistance of the granular particles to compression and expansion. It is modelled as per (Lun et al., 1984):

$$\mu_{s,kin} = \frac{4}{3} \alpha_s^2 \rho_s d_s g_{0,ss} (1 + e_{ss}) \left(\frac{\Theta_s}{\pi} \right)^{1/2} \quad (4.17)$$

The frictional viscosity accounts for the generation of stress is mainly due to friction between particles in dense flows with low shear, where the secondary volume fraction for the solid phase nears the packing limit. It is modelled as per (Schaeffer, 1987):

$$\mu_{s,fr} = \frac{p_s \sin \theta}{2\sqrt{I_{2D}}} \quad (4.18)$$

where, θ is the angle of internal friction and I_{2D} is the second invariant of the deviatoric stress tensor.

4.1.3 PARCELS

Flows with high particle concentrations have a large number of particles and it becomes computationally intensive to solve for all of them. The DPM model uses the concept of parcels which is a group of particles and are indicative of the properties such as diameter and velocity of the particle. The number of parcels are determined by the number of injection locations and the frequency of injection. It represents the resolution of the discrete phase in a manner similar to mesh resolution for the continuous phase (Braun et al., 2012). A high number of parcels improves the discretization of the discrete phase and aides with convergence, accuracy and stability but makes the simulation computationally expensive. The standard parcel release methods is used in this study. This method injects a single parcel per injection stream per time step. The number of particles in the parcel, NP is determined as given below:

$$NP = \dot{m}_s \frac{\Delta t}{m_p} \quad (4.19)$$

4.1.4 COUPLING BETWEEN PHASES

The interaction between the continuous phase and the discrete phase can be defined in Fluent by means of coupling. The choice of coupling resides on the volume fraction of the particles in the flow. In one-way coupling or uncoupled approach, the fluid phase influences the discrete phase via aerodynamic forces such as drag and turbulence while

the discrete phase in return has negligible influence on the fluid. The DPM particles may be tracked in this approach in post processing but they do not affect the flow solution. This method is appropriate in cases where particle concentration is less resulting low mass and momentum loading and the external body forces seen in momentum equations (4.7) and (4.8) become zero i.e. $\vec{F}_b = 0$.

In two-way coupling or the coupled approach, in addition to the impacts of the continuous phase on the discrete phase, the heat, mass and momentum gained by the particles that follows a trajectory is tracked and incorporated in the subsequent continuous phase calculations. This is accomplished by first solving the continuous flow field and then injecting the discrete phase and calculating the particle trajectory. The continuous phase is then recalculated using the mass, momentum and heat exchange terms obtained from the discrete phase calculation followed by the recalculation of the discrete phase trajectories based on the latest continuous phase flow field. This process is carried out alternatively till both the discrete phase trajectories and continuous phase flow field solutions stop changing. A simulation where the different phases of a multiphase fluid interact with each other, particle-particle collisions occur and the particles take up a volume in the flow is called a fully coupled simulation. In four-way coupling used in this study, the inelastic collisions of the particles in has an effect on the momentum exchange.

The Continuous phase flow field must be solved first when the DPM model is applied in the Lagrangian framework. The number of continuous phase iterations performed before each DPM injection depends on the sensitivity of the mass, momentum and energy sources of the DPM trajectories on the continuous phase. It is a measure of the frequency at which the particles are tracked and the DPM sources are updated. A higher number of continuous phase iterations will give a stable solution but in a case with a high solid concentration where the DPM injection has a high influence on the fluid flow, a delay in convergence occurs.

4.2 EROSION RATE

Erosion causes the gradual removal of material from a surface due to repeated impact of sand particles or liquid droplets (Det Norske Veritas RP O501, 2007). The rate at which the process take place is called erosion rate and it is represented in mass removed per unit area. The default ANSYS erosion model as laid out by (Edwards et al., 1998) is used in this thesis and it is represented below in (4.20).

$$ER = \sum_{p=1}^{N_{particles}} \frac{\dot{m}_s C(d_p) f(\alpha') v^{b(v)}}{A_{face}} \quad (4.20)$$

where, \dot{m}_p is the mass flow rate of the particle, α is the impact angle of the particle on the face of the wall, $f(\alpha')$ is the impact angle function and it characterizes the ductility of the target material is input in the form of a piecewise-linear profile in Fluent and the values are laid out in table 4.2. A_{face} is the area of the cell face at the wall. Constant values of relative velocity function $b(v)$ and particle diameter function $C(d_p)$ are laid out in table 4.1 as per (Det Norske Veritas RP O501, 2007).

Table 4.1: Erosion functions for steel

Material	Diameter Function	Velocity Exponent Function	Density (kgm^{-3})
Steel	2^{-9}	2.6	7800

Table 4.2: Piecewise linear profile of the impact angle function

Point	Angle	Value
1	0	0.0
2	20	0.8
3	30	1.0
4	45	0.5
5	90	0.4

4.3 VISCOUS HEATING

Viscous dissipation is generally used in turbulence flows to describe the rate at which the kinetic energy is converted into internal energy due to the flow working against viscous stresses. This transformation causes a temperature rise and heats up the fluid. This process is irreversible and is referred to as viscous dissipation. In macro-scale studies this phenomenon is generally ignored but it's inclusion is critical in understanding the causes for temperature rise in highly viscous fluids. The heat that is generated through viscous heating causes a local increase in temperature near the pipe walls which consequently causes a decrease in viscosity resulting in a local increase in flow velocity. This velocity increase assists in the further increase in local temperature. The energy equation solved for a single phase is written as follows:

$$\frac{\partial}{\partial t}(\rho E) + \nabla \cdot (\vec{u}(\rho E + p)) = \nabla \cdot (k_{eff} \nabla T) + S_h \quad (4.21)$$

where, k_{eff} is the effective conductivity and S_h is the source term. Viscous heating is incorporated in non-Newtonian laminar flow equations by means of UDFs which are displayed in APPENDIX B. Equation (4.21) is modified by the addition of an energy source term to include the viscous heating effect. It is defined by the viscous dissipation function ψ in equation (4.23) and ϕ in the UDFs. The source term S_h is written below in (4.22).

$$S_h = \left[k \psi^{\frac{n-1}{2}} + \frac{\tau_y}{\sqrt{\psi}} \right] \psi \quad (4.22)$$

$$\psi = 2 \left[\left(\frac{\partial u}{\partial x} \right)^2 + \left(\frac{\partial v}{\partial y} \right)^2 + \left(\frac{\partial w}{\partial z} \right)^2 \right] + \left[\frac{\partial u}{\partial y} + \frac{\partial v}{\partial x} \right]^2 + \left[\frac{\partial u}{\partial z} + \frac{\partial w}{\partial x} \right]^2 + \left[\frac{\partial v}{\partial z} + \frac{\partial w}{\partial y} \right]^2 \quad (4.23)$$

$$dS[eqn] = \left[\frac{(kn + k)\psi^{\frac{n}{2}} + \tau_y}{2\sqrt{\psi}} \right] \quad (4.24)$$

A first order differentiation of S_h is performed. If $dS[eqn] = 0$ is assumed then the explicit solution for the source term is enforced. Viscous heating criterion as laid out by (Sestak & Charles, 1987) is an indication of the relationship between viscosity and temperature which in turn quantifies the extent of viscous heating effects on the fluid. Equation (6.16) below defines the viscous heating criterion. At D^* nearing zero the viscous heating is negligible, at $D^* > 0$ the viscous heating is non-negligible and has a weak viscosity-temperature relationship and at $D^* < 0$ the viscous heating is non-negligible and has a strong viscosity-temperature relationship.

$$D^* = \frac{\dot{V}(-dp/dx)}{u\pi d(T_o - T_e)} \quad (4.25)$$

5 METHODOLOGY

A parametric study is performed in the erosion model with a total of 3 factors; factor-1 is solid percentage, factor-2 is flow velocity and factor-3 is sand fraction. Each factor has 5 levels and hence a total of $5^3 = 125$ simulations will need to be run in this scenario. To reduce the computational load on the analyses, the experiment is designed using Taguchi statistical method reducing the number of simulations. Table 5.1 below details the different variables and their levels.

Table 5.1: Factors used in the erosion model

Levels	Factor-1 solid percentage (%)	Factor-2 Flow velocity (m_s^{-1})	Factor-3 Sand fraction (%)
1	70	0.75	15
2	73	1.10	25
3	76	1.70	30
4	79	2.30	40
5	82	2.70	50

5.1 TAGUCHI METHOD

Japanese engineer Genichi Taguchi first laid out the Taguchi method for design of experiments. The method utilizes orthogonal arrays to stipulate the way of conducting minimal number of experiments to give the maximum information of all factors that affect the performance parameter. The solid percentage, flow velocity and sand fraction are selected as the three factors and each has five factor levels resulting in a L25 (5^3) orthogonal array that reduces the $5^3 = 125$ simulations to 25 simulations for the erosion model. A Taguchi orthogonal array is developed using Minitab 17 software with the above mentioned variables and such that the left most variable in the array changes less than the subsequent variables, thus reducing the cost of running experiments with multiple factors (Kacker et al., 1991). The above method is adopted to design the experiment for the erosion model and it is laid out in table 8.1 in Appendix A. Another available method for designing the experiment is the full factorial design, however this method requires a higher number of simulations to be run.

5.2 L-PIPE FLOW MODEL

An experimental setup to study the paste backfill flow through pipes was prepared to monitor the velocity of paste backfill flowing under the influence of gravity. The backfill material is composed of tailings from a gold mine, sand and water. An arrangement of the experimental setup as used in the laboratory is shown below in figure 5.1. An inverted cone made of sheet metal is used as a funnel to collect and store the material temporarily prior to conducting the experiment. The funnel is connected to a 1.90 m long vertical plastic pipe of 2 inches (0.0508 m) inner diameter. A 90° elbow connects the vertical pipe to a 0.50 m horizontal pipe. The funnel is attached to the pipe by means of adhesives. Below the funnel-pipe interface, a small slit is made in the pipe and a copper plate is inserted into it. This copper plate serves as a stopper and enables the control of the backfill flow through the pipe.

The paste backfill is mixed in the proportions mentioned in solid percentages ranging from 70% to 78% in steps of 2% and filled in the funnel. Upon removing the copper stopper plate, the backfill flows down the pipe under the effect of its own weight. The velocity of the backfill through the pipes is observed with the help of three video cameras pointed at three distinct locations on the pipe. The experiment is repeated three times for each solid percentage and the data is recorded.



Figure 5.1: L-pipe arrangement used in the laboratory

5.3 MODEL DEVELOPMENT

AutoCAD 2017 is used to model the pipes using the sweep option. The model is then imported to ANSYS Workbench through ANSYS Design Modeler. ANSYS Meshing tool is used to develop the grid for the model. Figure 5.3 shows the schematic arrangement of the viscous heating models developed for pipelines from Mine-A, Mine-B and Mine-C. Figure 5.2 shows the schematic arrangement of the erosion model developed for pipelines from Mine-A. A grid independence study is conducted for all models to refine the mesh such that the solution is not affected by the variation in grid size. Tables 5.2, 5.3 and 5.4 detail the number of mesh elements generated for the study and if result variation was observed.

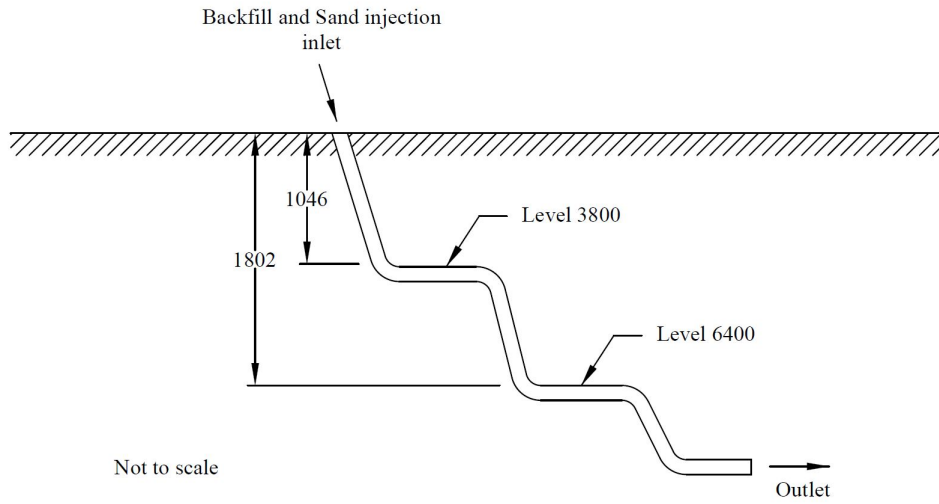


Figure 5.2: Erosion model pipeline schematic arrangement

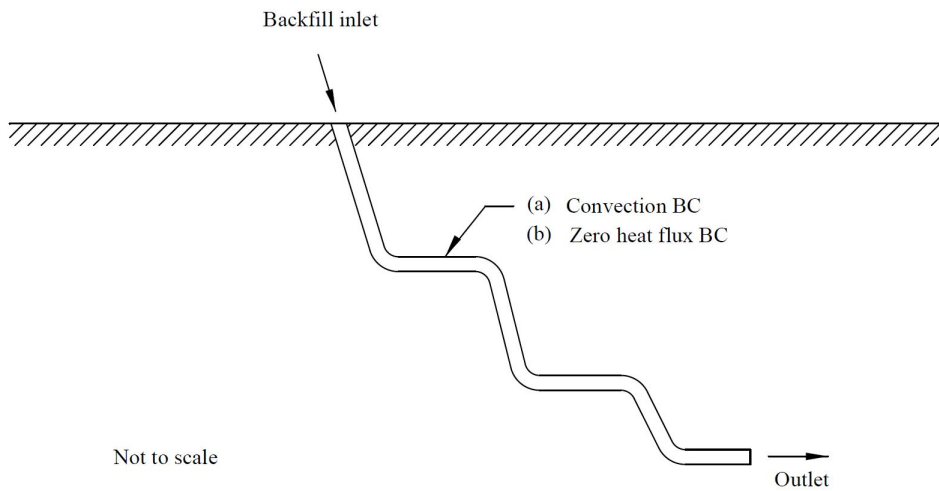


Figure 5.3: Viscous heating model pipeline schematic arrangement

Table 5.2: Grid independence results for Mine-A

Number of mesh elements	Pressure drop (kPa)	% Change
1.6M	4328.93	-
2.3M	4395.94	1.55
3.2M	4453.50	1.31
3.7M	4456.77	0.07
7.9M	4467.79	0.25

Table 5.3: Grid independence results for Mine-B

Number of mesh elements	Pressure drop (kPa)	% Change
1.8M	849.31	-
2.5M	850.48	0.14
3.5M	856.51	0.71
4.8M	860.49	0.46
5.2M	869.90	1.09
5.5M	874.38	0.52

Table 5.4: Grid independence results for Mine-C

Number of mesh elements	Pressure drop (kPa)	% Change
2.0M	7015.81	-
2.5M	7281.95	3.79
3.8M	7365.44	1.15
4.1M	7425.42	0.81
8.0M	7541.53	1.56

Based on the grid independence studies, the elements with 2.3 million cells, 2.5 million cells and 3.8 million cells were selected for Mine-A, Mine-B and Mine-C respectively. The length and diameters of the pipelines are listed below in table 5.5. A 5D bend is modelled

in elbows. A 5D bend describes the elbow radius which is considered to be 5 times the nominal diameter.

Table 5.5: Pipeline dimensions for Mine-A, Mine-B and Mine-C

Mine name	Pipeline length (<i>m</i>)	Pipeline diameter (<i>m</i>)
Mine-A	2896.2	0.2027
Mine-B	2373.3	0.1524
Mine-C	1729.1	0.2032

5.4 MATERIAL PROPERTIES

The densities of individual backfill constituents sand, water, and tailings of Mine-A, Mine-B and Mine-C are listed below in table 5.6. Table 8.7 containing the composition of sand and tailings from all the mines is included in Appendix A.

Table 5.6: Backfill constituents densities

Location	Material	Value	Unit
Mine-A	Sand	2630	kgm^{-3}
Mine-A	Tailings	2743	kgm^{-3}
Mine-B	Tailings	2800	kgm^{-3}
Mine-C	Tailings	2038	kgm^{-3}
-	Water	1000	kgm^{-3}

For the erosion model, the yield stresses and consistency indices are obtained from cup and bob viscometer experiments. Table 5.7 below shows material and flow properties for the case used for validation of the numerical model. The density of the backfill with and without sand is determined from the individual densities of water, sand and tailings from table 5.6 and equation (3.2). The total mass flow rate is a product of the total density with sand, velocity and pipe cross sectional area. The sand mass flow rate is a percentage of the total sand fraction in the total mass flow rate. Tables 8.2 and 8.3 included in the Appendix

A contain the material properties of the 25 erosion model cases that were run on ANSYS Fluent. The viscous heating model uses α , the ratio of activation energy to universal gas constant. The value of α is worked out for each solid concentration and for each mine through cup and bob viscometer experiments carried out at high, medium and low temperatures. Equation (3.27) provides one method of determination of the α value and the other method is through linear curve fitting of the slopes from figures 3.15, 3.16 and 3.17. Table 5.8 below showcases the material and flow properties of the validation case. The yield stress and consistency index are extrapolated for higher solid concentrations. The properties for viscous heating models of Mine-A, Mine-B AND Mine-C are displayed in tables 8.4, 8.5 and 8.6 respectively in Appendix A.

Table 5.7: Material properties for erosion validation case

Description	Value (<i>m</i>)	Unit
Solid percentage	82	%
Flow velocity	1.8	ms^{-1}
Sand fraction in solid %	50	%
Total sand fraction	41	%
Yield stress	79.644	Pa
Consistency index	0.344	Pas
Density without sand	1788	kgm^{-3}
Density with sand	2129	kgm^{-3}
Total mass flow rate	123.64	$kg s^{-1}$
Sand mass flow rate	50.72	$kg s^{-1}$

Table 5.8: Material properties for viscous heating validation case

Description	Value (<i>m</i>)	Unit
Solid percentage	82	%
Flow velocity	1.8	ms^{-1}
Yield stress	36.54	Pa
Thermal conductivity	3.14	$Wm^{-1}K^{-1}$
Specific heat capacity	1715.14	$Jkg^{-1}K^{-1}$
Consistency index	0.518	$Pa\cdot s$

5.5 PARTICLE SIZE DISTRIBUTION

Sand particles used for the purposes of backfill mixing and numerical modelling do not have a single diameter, but instead a wide range of particle diameters exist. Particle sizes play an important role in the rheology of a fluid especially in a case with high solid concentration. Larger particles tend to remain in the bottom of the fluid flow and smaller particles flow more freely in the upper region. Predicting the solid concentration and distribution accurately is necessary to numerically solve the particle impingement on the pipe and the resulting erosion rates.

Particle size distributions give the number of particles that fall into various size ranges as a percentage of the total number of sizes in the sample. Table 8.8 in Appendix A displays the sand particle sizes from Mine-A in terms of percentage of particles passed through and retained in a sieve. The commonly used approach for particle size distribution in ANSYS Fluent is to provide the first and last points and use a linear equation fit the particle size variation. However, to obtain different mass flow rates for each particle size, the Rosin-Rammler distribution which is an empirical equation to fit the particle size distribution curve is used. As per (Rosin & Rammler, 1933), the cumulative percentage of retained Y_d at a size d is given by the equation (5.1) where mean diameter d_n and spread diameter n are used as fitting parameters.

$$Y_d = \exp\left(\frac{-d}{d_n}\right)^n \quad (5.1)$$

$$n = \frac{-\ln Y_d}{\ln\left(\frac{d}{d_n}\right)} \quad (5.2)$$

The particle sizes from table 8.8 are plotted in figure 5.4 and an exponential curve fitting is done to match equation (5.1). Values of spread parameter n for all particle sizes are calculated as per equation (5.2) and an average value is taken. The value of mean diameter d_n is obtained from the graph for a $Y_d = e^{-1}$ from figure 5.4. The resulting particle size distribution parameters are displayed in table 5.9.

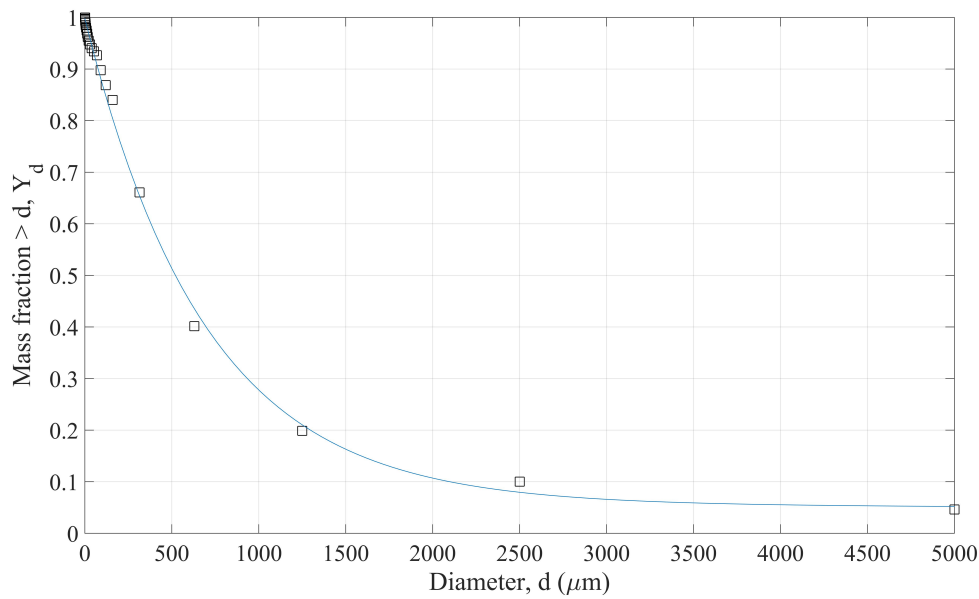


Figure 5.4: Rosin-Rammler curve fit for Mine-A sand particle sizes
Table 5.9: Rosin-Rammler sand particle size distribution parameters

Parameter	Value	Unit
Minimum diameter	0.96	μm
Maximum diameter	5000	μm
Mean diameter	700	μm
Spread diameter	0.966255	-
No. of diameters	25	-

5.6 BOUNDARY CONDITIONS AND SOLUTION PARAMETERS

The boundary conditions and solution parameters set for the erosion model are listed below in tables 5.11 and 5.12 and those for the viscous heating model are listed in 5.13. The two-phase backfill fluid is modelled using a Eulerian multiphase model where the backfill is assigned phase 1 and sand is assigned granular phase 2. The choice of granular multiphase provides a large number of parameters that need to be set.

The table 5.12 below details the approaches and equations adopted. Default under relaxation factors are used for the simulations to obtain stability and accuracy in the results. They may be lowered where necessary to solve for divergence in the residuals. The pipe wall has a DPM boundary condition set to reflect. This ensures the particles rebound off the surface of the wall with normal and tangential coefficients of restitution. These coefficients are displayed below in table 5.10.

The temperature rise in the non-Newtonian backfill due to viscous heating can be modelled by either switching ON the viscous heating option in laminar viscous model panel on ANSYS Fluent or by compiling a UDF to modify the source term of the energy equation. The UDF approach is employed in this thesis. The table 5.13 below details the boundary conditions adopted for this model. The UDFs used are displayed in Appendix B. In the case to analyze the individual effects of viscous heating phenomenon the zero heat flux boundary condition is used. For the case where the particle-particle interaction is added in the determination of temperature, the multiphase model detailed above in table 5.11 is used in conjunction with the viscous heating model.

Table 5.10: DPM wall discrete phase reflection coefficients

Parameter	Coeff. 1	Coeff. 2	Coeff. 3	Coeff. 4
Tangent function	0.988	-0.029	6.43×10^{-4}	-3.56×10^{-6}
Normal function	0.993	-0.0307	4.75×10^{-4}	-2.61×10^{-6}

Table 5.11: Erosion model boundary conditions

Parameter	Input
Model	Multiphase Eulerian - 2 phases Viscous - Laminar
Phase 1	Backfill
Phase 2	Granular phase (Sand)
Gravity	-9.81 ms^{-2} in -Y
Inlet	Velocity inlet
Outlet	Pressure outlet
Wall	No slip
Pressure velocity coupling	PC-SIMPLE
Momentum	First order upwind
Volume fraction	First order upwind

Table 5.12: Granular phase parameters

Parameter	Input
Granular viscosity	Gidaspow 1992
Granular bulk viscosity	Lun et al 1984
Frictional viscosity	Schaeffer 1987
Angle of internal friction	30.00007
Frictional pressure	Based on KTGF Ding and Gidaspow 1990
Friction packing limit	0.61
Granular temperature	Algebraic
Solids pressure	Lun et al 1984
Radial distribution	Lun et al 1984
Elasticity modulus	Derived
Packing limit	0.63

Table 5.13: Viscous heating model boundary conditions

Parameter	Input
Model	Viscous - Laminar Energy - ON
Gravity	-9.81 $m s^{-2}$ in -Y
Inlet	Velocity inlet at 293.15 K
Outlet	Pressure outlet
Wall	No Slip Convection
Heat transfer coefficient	10.5 $W m^{-2} K^{-1}$
Free stream temperature	298.15 K
Pressure velocity coupling	SIMPLE
Momentum	Second order upwind
Energy	Second order upwind

6 RESULTS AND DISCUSSION

6.1 EROSION

Prior to performing numerical simulations for predicting erosion, a validation of the flow model was done. This study involved experimentally obtaining the velocity of backfill at various solid concentrations in an L-shaped pipe using cameras. The L-pipe was numerically modelled using the VOF model and the results are plotted below in figure 6.1. We see good agreement between the results from the experiment and the numerical model.

The regions in the piping system with elbows are the most erosion prone segments of the entire system. Contours of erosion obtained from the numerical model are displayed below in figures 6.2 to 6.7. We see that there is a change in flow direction in an elbow when the particles strike on the surface of the pipe instead of changing directions with

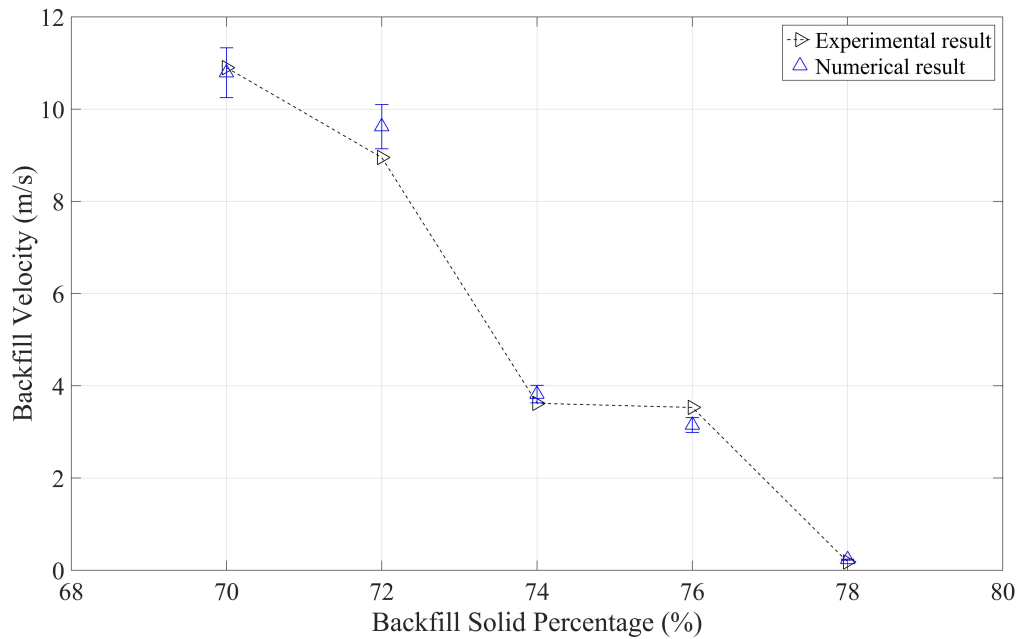


Figure 6.1: Backfill flow model validation with experimental results

the fluid. A schematic of the pipe elbow showing the flow direction and impact angle α is illustrated below in figure 6.8 where D is the pipe diameter and R is the $5D$ radius of the bend. In figures 6.3 and 6.5 we see the vector plots which indicate the direction of the particle during motion. Figures 6.2, 6.4, 6.6 and 6.7 show the erosion that occurs during the flow.

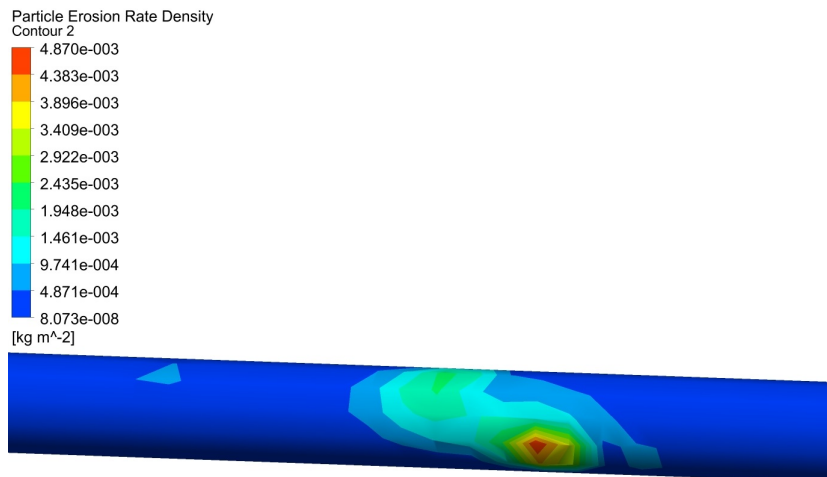


Figure 6.2: Erosion contour from numerical model at level 3800 - horizontal segment

For the purpose of validation, erosion was measured on the site at different points and at two levels 3800 and 6400. The pipe thickness was measured using ultrasonic devices

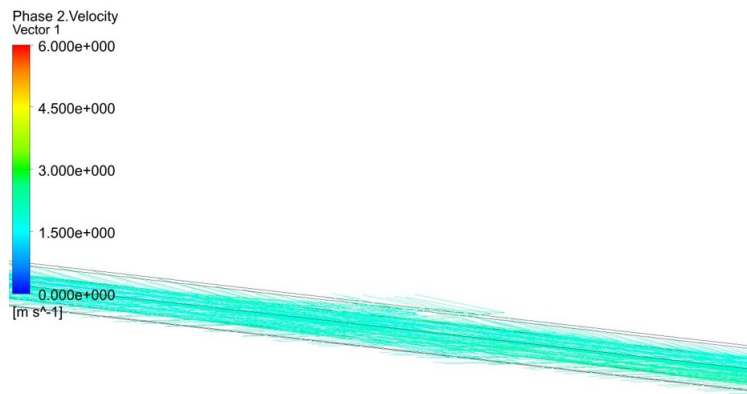


Figure 6.3: Vector contour from numerical model at level 3800 - horizontal segment

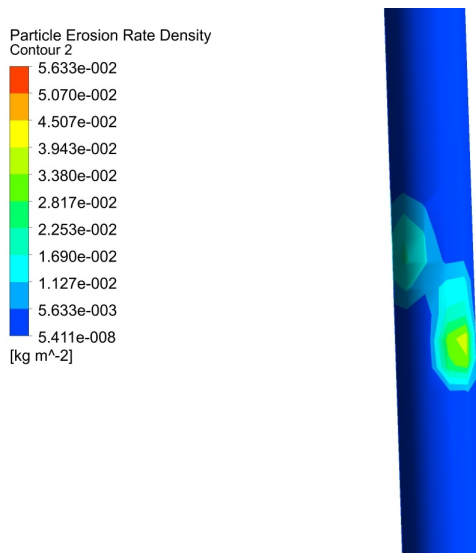


Figure 6.4: Erosion contour from numerical model at level 3800 - vertical segment

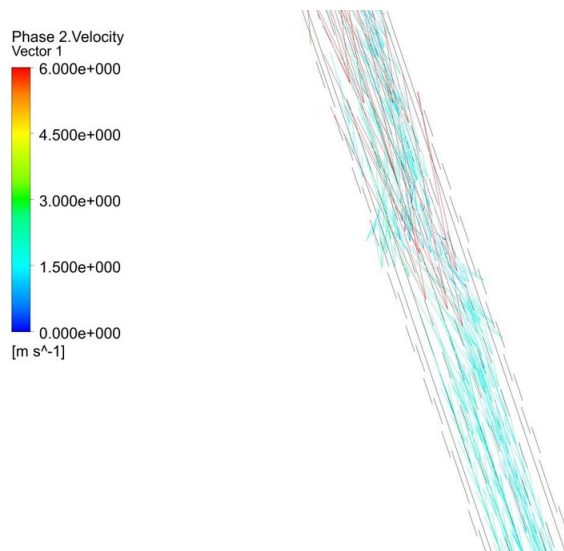


Figure 6.5: Vector contour from numerical model at level 3800 - vertical segment

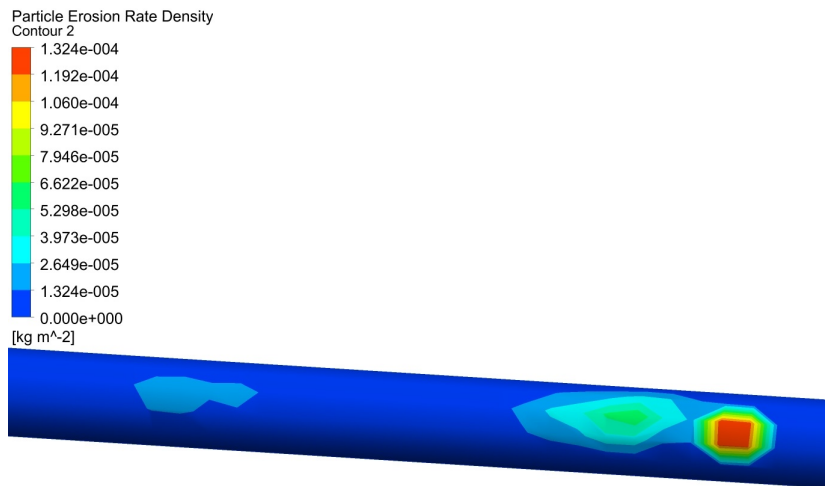


Figure 6.6: Erosion contour from numerical model at level 6400 - horizontal segment

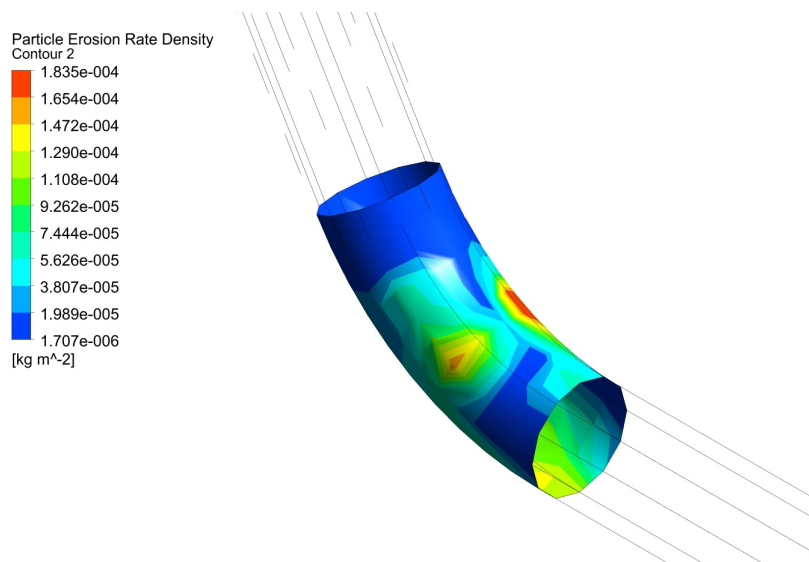


Figure 6.7: Erosion contour from numerical model at level 6400 - elbow segment

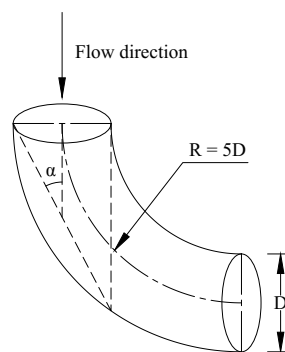


Figure 6.8: Particle impact angle in a 90° elbow

along the circumference of the pipe. Eight equidistant points along the circumference are chosen as shown below in figure 6.9. In the mine data, maximum erosion was seen on the underside at points 4, 5 and 6 while minimum erosion was seen on the upper side at points 8, 1 and 2.

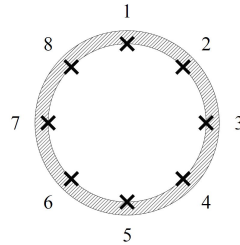


Figure 6.9: Measurement points along pipe circumference

In figures 6.10 and 6.12 below we compare the numerical results and the in-situ mine data. At Level 3800, there is an over prediction by the numerical model although, the highest erosion in point 5 is in good agreement. In the Level 6400, good agreement was seen at all points on the bottom and sides of the pipe but an under prediction by the numerical model was seen at the top side of the pipe. Figures 6.11 and 6.13 show the discrete phase volume fractions and secondary flows at the two levels. At both levels we see particle concentrations are higher at the bottom side of the pipeline. From the secondary flow figures we note that the higher erosion rates predicted by the model at level 3800 at points 4 and 6 is due to a recirculation of the flow near these two points. The flow pattern causes a local increase in particle concentration and affects erosion magnitude and erosion patterns.

Table 6.1: % Error in Level 3800 erosion results

Point	1	2	3	4	5	6	7	8
% Error	58	38	84	203	8	144	78	46

Table 6.2: % Error in Level 6400 erosion results

Point	1	2	3	4	5	6	7	8
% Error	71	71	4	11	6	40	36	69

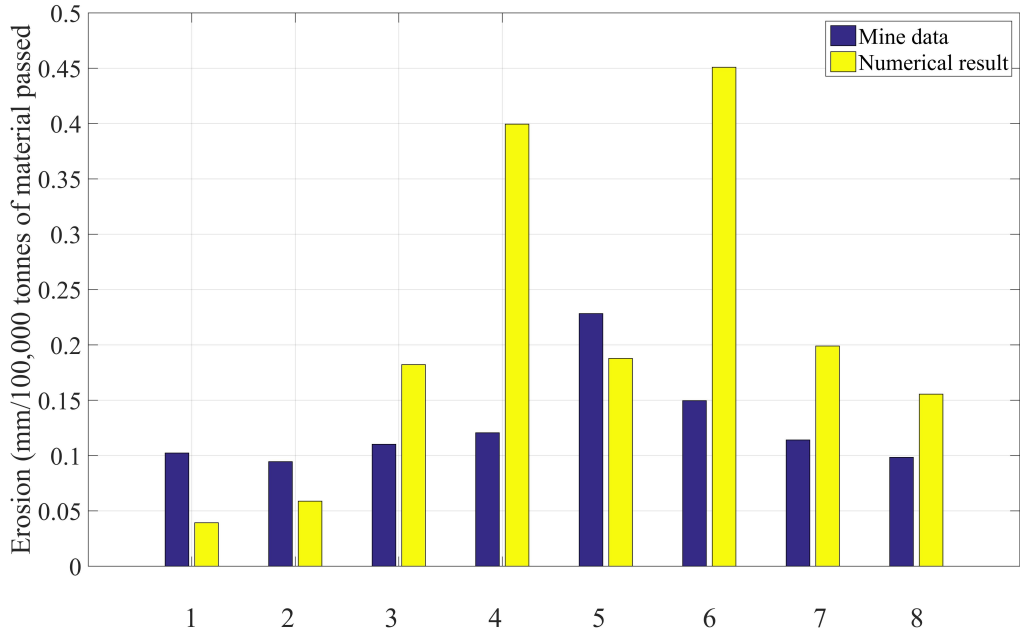


Figure 6.10: Erosion validation in Level 3800

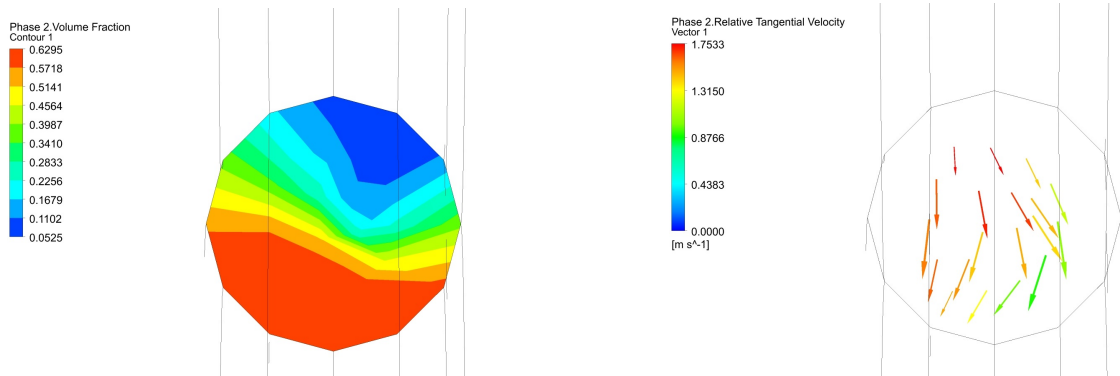


Figure 6.11: Discrete phase volume fraction and secondary flow at level 3800

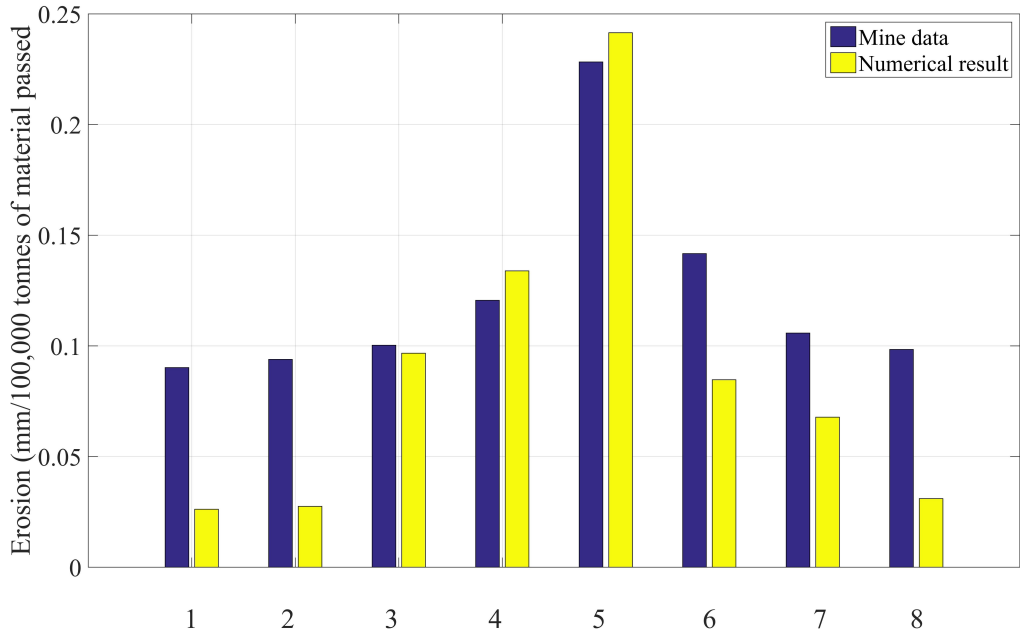


Figure 6.12: Erosion validation in Level 6400

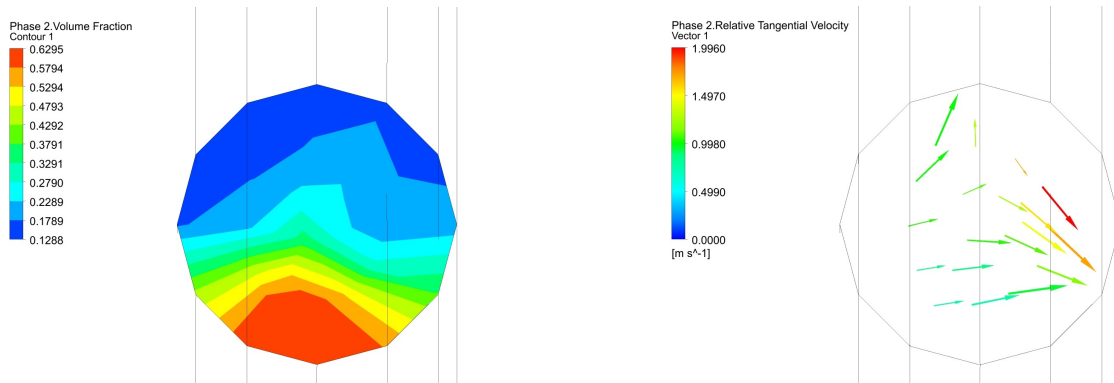


Figure 6.13: Discrete phase volume fraction and secondary flow at level 6400

The results from the numerical model were analysed using Taguchi statistical method to obtain the effects of the individual parameters used in the study as shown below in figure 6.14 and interaction between these parameters as seen in figure 6.15. From figure 6.14 we see that velocity has the highest influence on erosion followed by sand fraction and solid fraction. As the velocity increases the frequency of impact of the particles on the pipe wall increases. We see minimal change in erosion as solid percentage increases and a reduction in erosion at sand fractions. This can be attributed to the increase in viscosity arising from an increase in solid percentage and thus, reducing erosion. At high solid percentages and large particle loading, the influence of drag force on the particle trajectory is high and this reduces the interaction between particles and pipe wall thereby reducing erosion. At high solid concentrations when particles rebound from the wall, they hit particles that are moving towards the wall and slow them down. This phenomenon called shielding results in lower erosion rates (Brown et al., 1981).

The way to read the interaction plot in figure 6.15 is, plots that are parallel have little to no interaction between them while those which cross each other and deviate have a high interaction. This is evident at low velocities where the increase in solid percentage and sand fraction has minimum effect on erosion but with the increase in velocity, the same factors have a profound impact on erosion. The same trend is seen at low sand fractions where the effect of increasing flow velocity and solid percentage has minimal effect on erosion but as the sand fraction increases the impact of the other factors becomes profound. At low and high solid concentrations, both velocity and sand fraction have an impact on erosion. Maximum influence between factors was noted at higher values and lower interaction was noted at low values. The highest erosion was reported at 82% solid concentration, 40% sand fraction flowing at 3 m s^{-1} velocity.

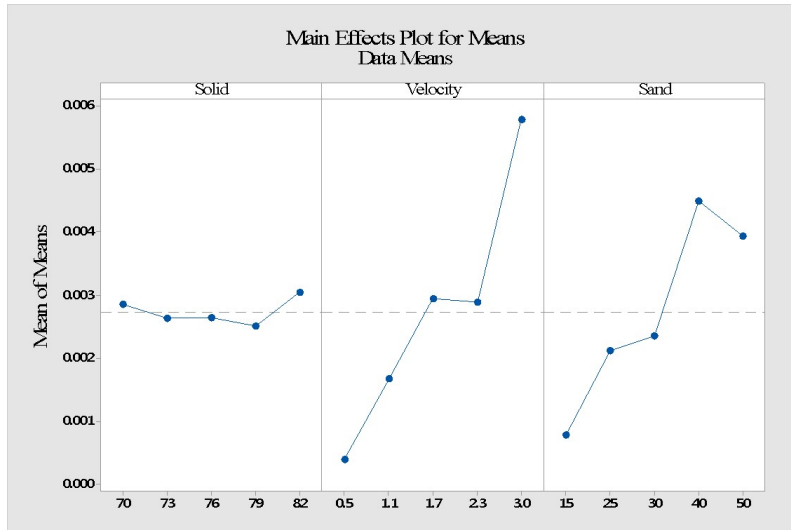


Figure 6.14: Taguchi analysis main effects plot

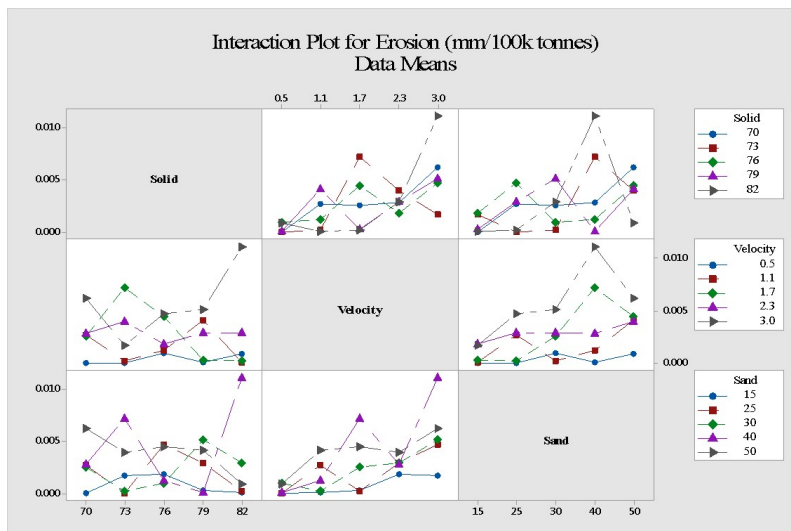


Figure 6.15: Taguchi analysis interaction plot

6.2 VISCOUS HEATING

Numerical simulations with the Bingham plastic model have been carried out with parametric studies on three different mines for determining the effect of temperature rise due to viscous dissipation. The first part involves temperature independent rheological properties at different solid concentrations. The second part involves temperature dependent rheological properties with the modified Bingham plastic equation detailed in (3.28). The third part involves the a zero heat flux boundary condition under temperature dependent rheological properties to determine the effect of viscous heating without convection effects.

The results from the numerical model solved using equation (6.16) is displayed below in figure 6.16. We see negative values for D^* in all three mines indicating a strong viscosity-temperature relationship and a non-negligible impact of viscous heating on the temperature rise process.

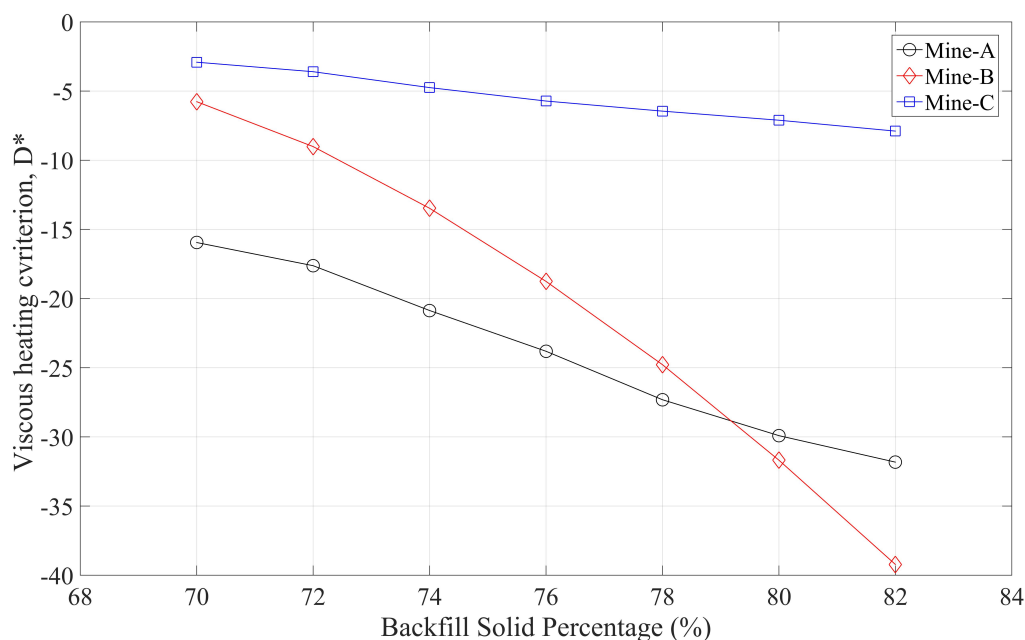


Figure 6.16: D^* comparison in three mines

The validation of the model was performed with temperature data collected from Mine-A and Mine-B. Mine-A used pill probes to record the data while Mine-B recorded the data directly from the paste at the exit of the pipeline. Figures 6.17, 6.18 and 6.19 show the temperature rises in the three mines along with the experimental data. We see a general

trend in all the three mines, the maximum temperature rise was seen in the temperature independent case followed by the temperature dependent case and the zero heat flux case. When the material properties are temperature dependent, as the temperature rises initially it affects the material properties such as viscosity which decreases. This decrease in viscosity causes the material to flow easily reduces the viscous heating effect in the fluid and thereby the temperature rise.

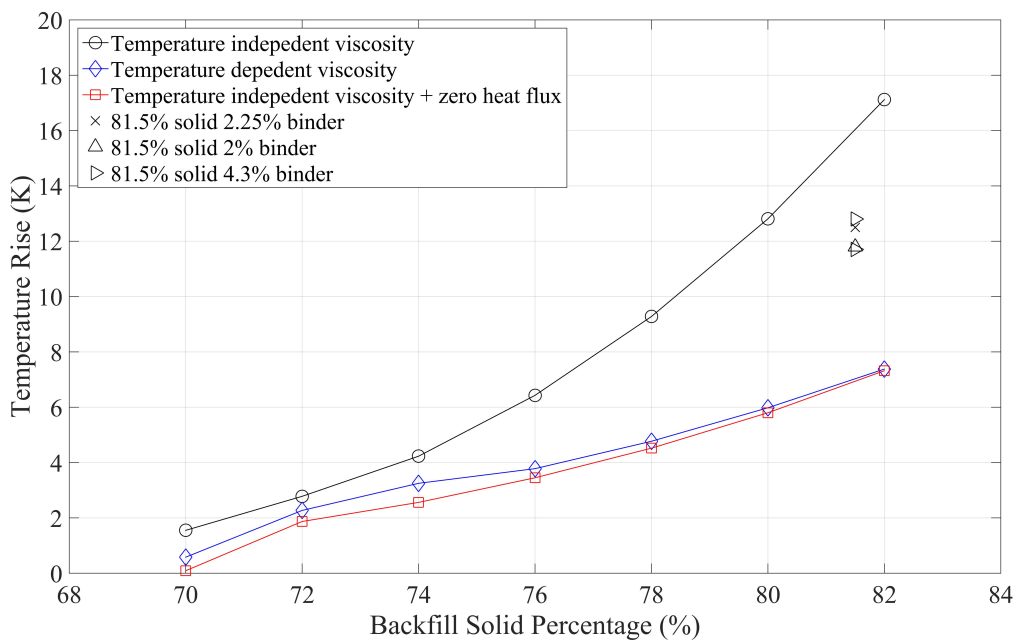


Figure 6.17: Temperature rise in Mine-A

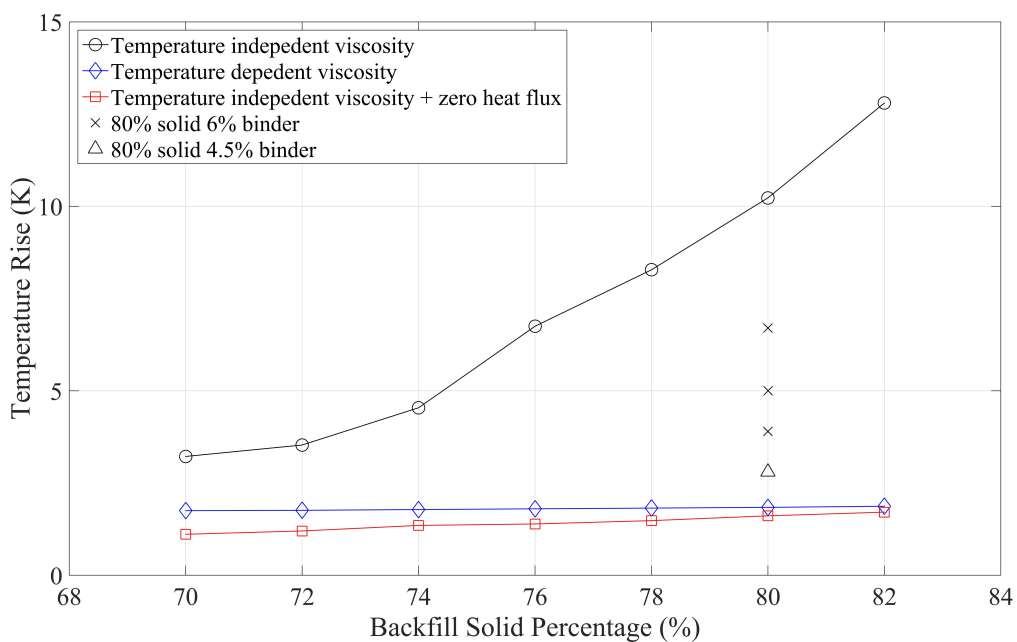


Figure 6.18: Temperature rise in Mine-B

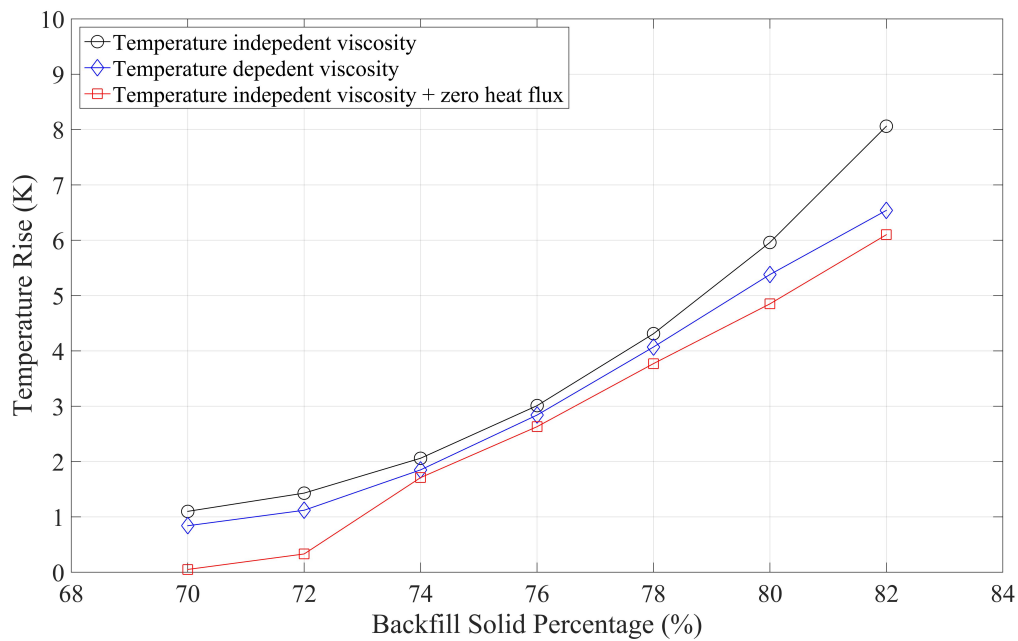


Figure 6.19: Temperature rise in Mine-C

In Mine-A we see less agreement between the numerical results and the mine in-situ data however, better agreement between them is seen in Mine-B. It can be seen from the mine in-situ data that the temperature rise increases with increase in binder percentage. Being a hydrating agent binders release heat when they cure. This causes an increase in the temperature and as the percentage of binder increases the effect it has on temperature rise also increases. Figure 6.20 shows the influence of viscous heating alone on temperature rise in the fluid. We see at high solid percentages the impact is profound in comparison to low solid percentages for Mine-A and Mine-C. This can be related to the high activation energy at low solid percentages in these mines indicating a strong viscosity-temperature relationship. Mine-B on the other hand also shows the same trend but with less change.

Figures 6.21 to 6.25 below depict the impact of material properties on the temperature rise. The change in temperature for unit change in a specific material property is determined to quantify the effect said property can bring about in temperature. Thermal conductivity is seen to have the highest impact followed by consistency index, mass flow rate, specific heat capacity and yield stress.

Figures 6.26 and 6.27 display contours obtained from numerical model for Mine-A with

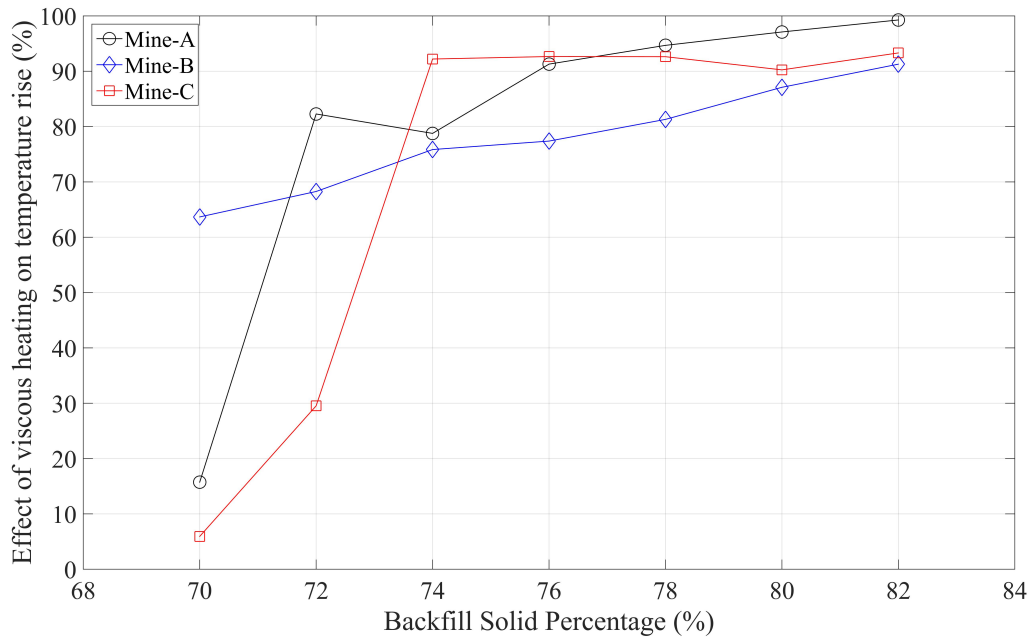


Figure 6.20: Influence of viscous heating on temperature rise

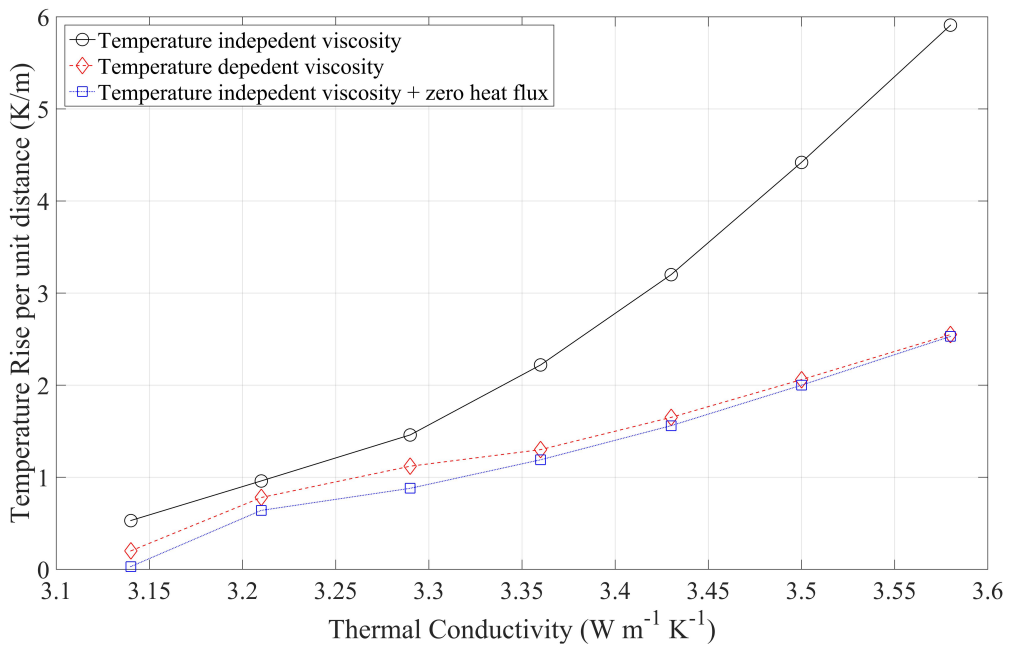


Figure 6.21: Influence of thermal conductivity on temperature rise

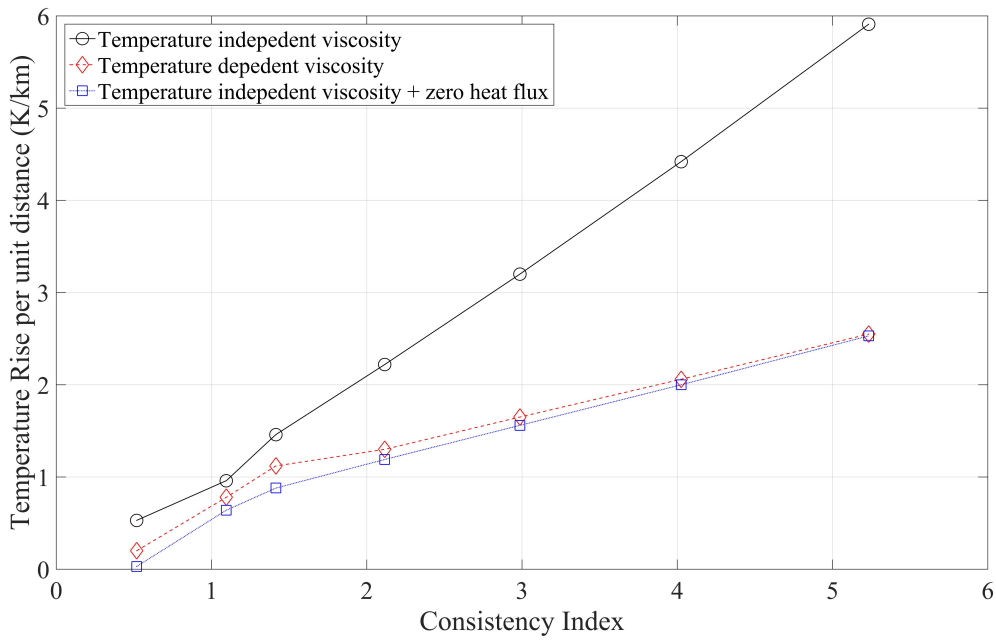


Figure 6.22: Influence of consistency index on temperature rise

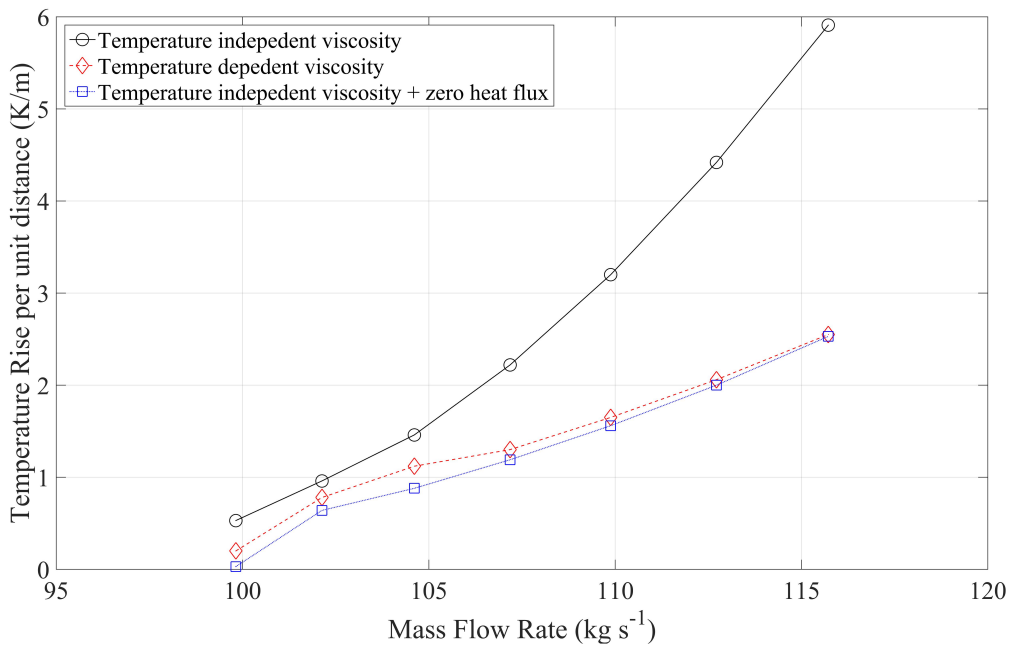


Figure 6.23: Influence of mass flow rate on temperature rise

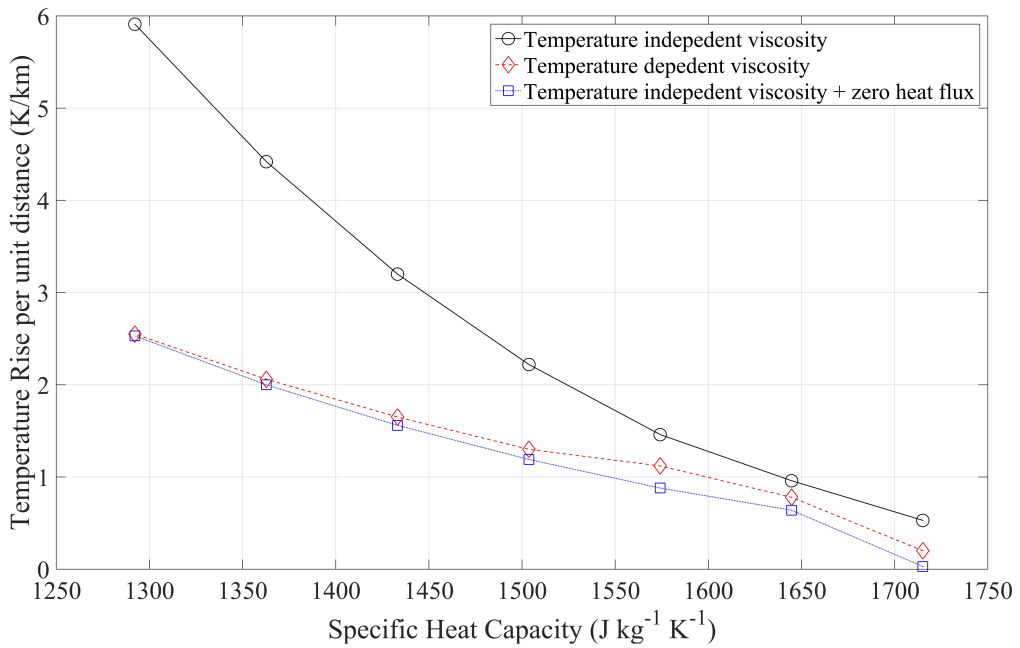


Figure 6.24: Influence of specific heat capacity on temperature rise

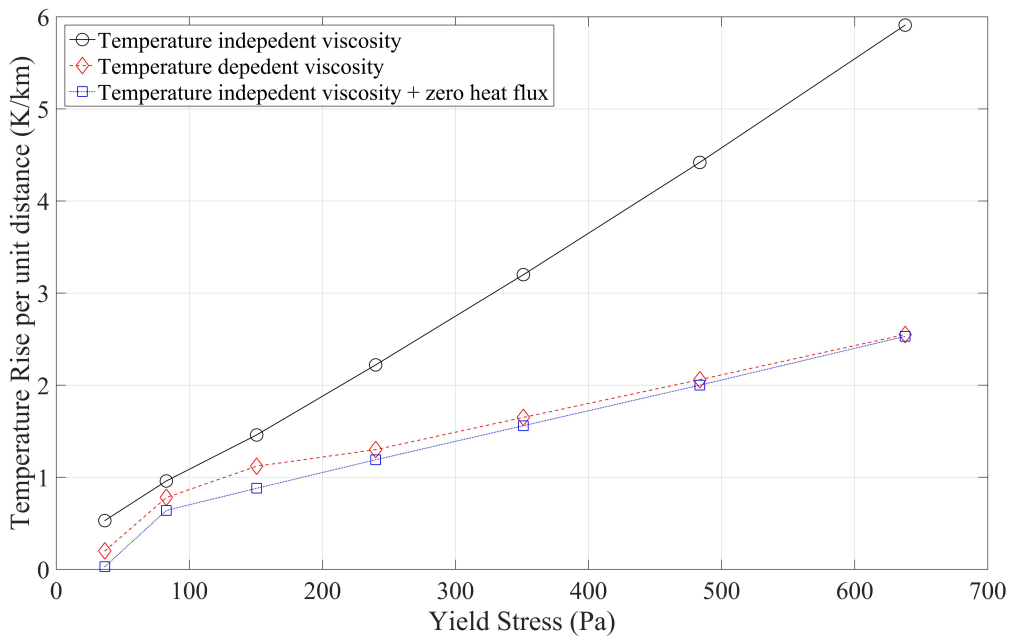


Figure 6.25: Influence of yield stress on temperature rise

temperature dependent material properties. In figure 6.26 we see the temperature contours at the pipeline entry, middle and exit segments. We see a difference in temperature in these portions, low temperatures at the inlet followed by a small but visible spike in temperature in the middle portion and highest temperatures at the exit portion. The elbow and horizontal segments at the exit are captured in figure 6.27, where the highest temperature is recorded. We also observe in the exit that the temperature is high in the vertical portion and elbow in comparison to the horizontal portion. This is due to the high flow velocity in these parts. At the bottom of the vertical segments the potential energy contained in the fluid is converted to kinetic energy and temperature increases. At the elbows the impact of the flow with the bottom wall of the pipe causes a recirculation in the fluid increasing heat transfer and raising the temperatures. Along the horizontal segments we see a stabilization of the velocity and flow which causes the temperature to reduce.

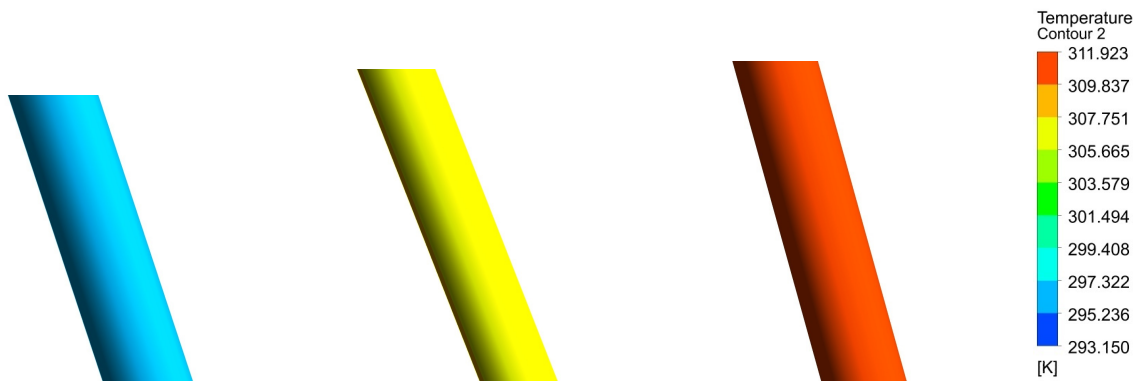


Figure 6.26: Temperature contour of pipeline entry, middle and exit segments

In figure 6.28 we see the temperature distribution along the length of the pipeline in Mine-A modelled with temperature dependent material properties. We observe a gradual increase in temperature along the length. A few peaks in temperature are seen at the regions of elbows and vertical segments.

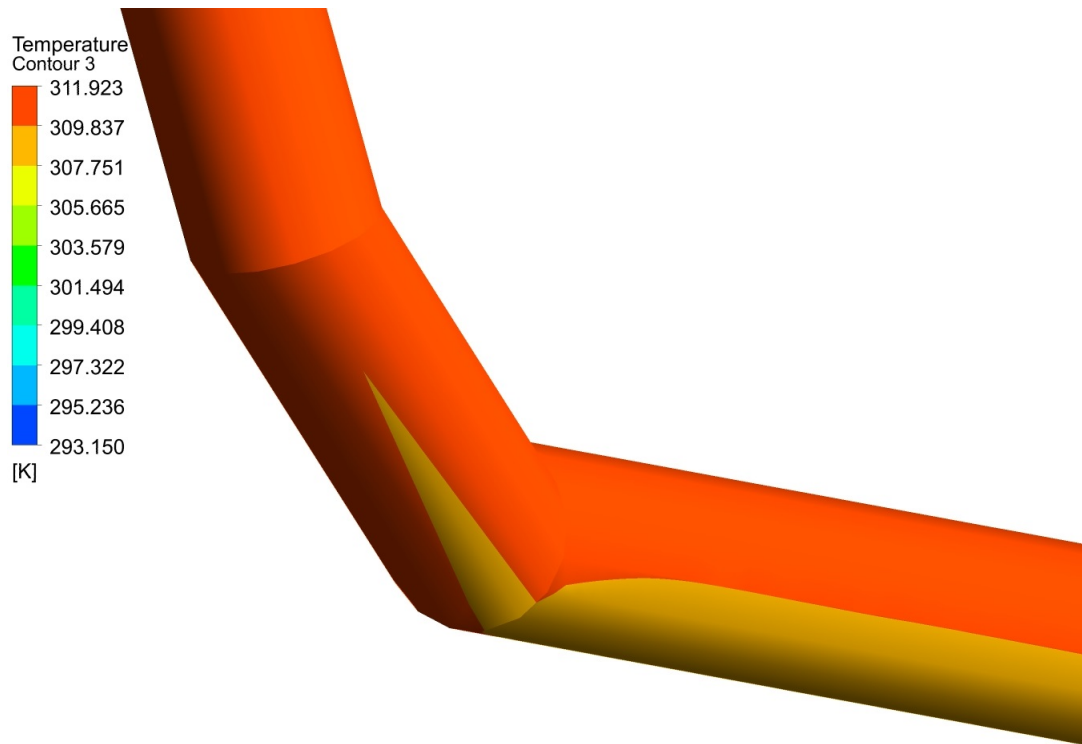


Figure 6.27: Temperature distribution at exit showing higher temperatures in vertical segment and elbow and temperature drop in horizontal segment

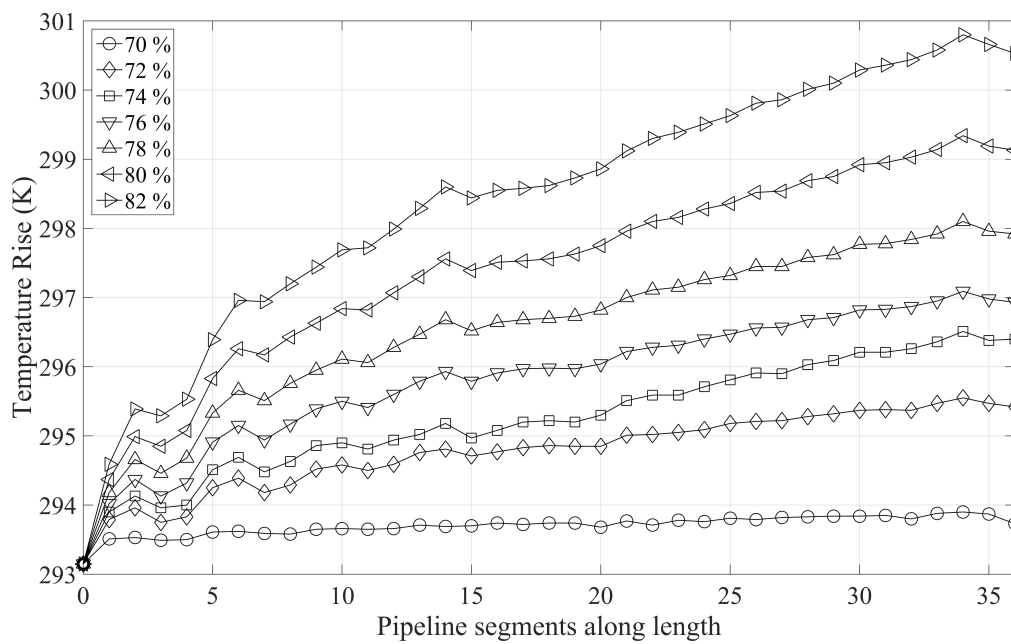


Figure 6.28: Temperature distribution in Mine-A

7 CONCLUSIONS AND RECOMMENDATIONS

The ability to predict the multiphase fluid flow behaviour with a high dispersed solid phase concentration is essential for not just predicting the erosion and temperature rise but also for efficient and effective design of the piping system that transports these materials. From both the numerical study and the in-situ mine data, it was seen that maximum erosion occurred in the under side of the pipe gradually reducing upwards along the circumference. From Taguchi analysis, the influence of flow velocity was seen to be the highest on erosion followed by sand fraction and solid percentage. Impact of high solid and sand percentages on erosion was little. This is due to less gap between the particles restricting lateral movement and increasing the inter-particle forces and thus, viscosity. A high viscosity fluid has a less impact on erosion in comparison to a low viscosity fluid. At high particle loadings, the impact of drag forces on particle trajectory influences the erosion.

Results from the numerical analysis indicated temperature rise was maximum for models running temperature independent properties followed by those running temperature dependent properties and zero heat flux. An increase in temperature brought about a reduction in yield stress and consistency index. The viscous heating criterion D^* values were seen to be less than zero confirming the initial assumptions that viscous heating is non-negligible in a mine backfill scenario and a strong viscosity-temperature relationship exists. The maximum impact on temperature rise by changes in material properties was seen from thermal conductivity followed by consistency index, mass flow rate, specific heat capacity and finally yield stress.

7.1 RECOMMENDATIONS FOR FUTURE WORKS

The results from this study forms a platform for future work in backfill rheology. The understanding of the effects of individual parameters on erosion will help in designing

better and long lasting systems in mines. This study can be further extended in the future by the inclusion of binder in the model. This will help in mimicking the real time conditions in the mine. Binder being a hydrating agent dissipates heat when curing and this causes an additional increase in temperature as also seen from mine in-situ data. The inconsistency in measured temperature data from the mine for the same solid and binder percentages indicate the need for a higher control in the environment during data collection which can be achieved using a chiller. A multiphase model similar to the erosion model may be developed to capture the effects of particle-particle interaction on the viscous heating phenomenon and temperature rise. Individual pipe segments such as fittings, elbows and joints can be targeted since these parts see the most erosion in a pipeline system. Impact of parameters not selected in this study such as particle size, shape, diameter, impact angles and pipe materials can also be studied. The results from the Fluent model used here can be compared with other erosion models available such as Mclaury et al, Salama & Venkatesh, Finnie, DNV, Oka, Zhang, Grant & Tabakoff. This will help in determining the most optimum model for non-Newtonian backfill flow through long distance pipelines.

REFERENCES

- Ahlert, K. R. (1994). *Effects of particle impingement angle and surface wetting on solid particle erosion of aisi 1018 steel*. BUiversity of Tulsa.
- Ansys fluent theory guide [Computer software manual]. (2015).
- Arrhenius, S. (1889). *Über die dissociationswärme und den einfluss der temperatur auf den dissociationsgrad der elektrolyte*. Wilhelm Engelmann.
- Aydin, O. (2005a). Effects of viscous dissipation on the heat transfer in a forced pipe flow. part 2: Thermally developing flow. *Energy Conversion and Management*, 46(18), 3091–3102.
- Aydin, O. (2005b). Effects of viscous dissipation on the heat transfer in forced pipe

- flow. part 1: both hydrodynamically and thermally fully developed flow. *Energy Conversion and management*, 46(5), 757–769.
- Barrett, J., Coulthard, M., & Dight, P. (1978). Determination of fill stability. In *Proceedings of the 12th canadian rock mechanics symposium* (pp. 85–91).
- Bingham, E. C. (1922). *Fluidity and plasticity* (Vol. 2). McGraw-Hill Book Compny, Incorporated.
- Boualil, A., Zeraibi, N., Boualil, S., & Amoura, M. (2011). Thermal development of the laminar flow of a bingham fluid between two plane plates with viscous dissipation. *International Journal of Thermal Sciences*, 50(1), 36 - 43. doi: <http://dx.doi.org/10.1016/j.ijthermalsci.2010.09.005>
- Bozzini, B., Ricotti, M. E., Boniardi, M., & Mele, C. (2003). Evaluation of erosion-corrosion in multiphase flow via cfd and experimental analysis. *Wear*, 255(1), 237–245.
- Braun, M., Srinivasa, M., & Gohel, S. (2012). Validation of an efficient cfd–dem model for large scale fluidized beds. In *Ninth international conference on cfd in the minerals and process industries, csiro, melbourne, australia*.
- Brennen, C. E. (2005). *Fundamentals of multiphase flow*. Cambridge university press.
- Brown, R., Jun, E.-J., & Edington, J. (1981). Erosion of α -fe by spherical glass particles. *Wear*, 70(3), 347–363.
- Choi, H. M., & Yoo, B. (2009). Steady and dynamic shear rheology of sweet potato starch–xanthan gum mixtures. *Food Chemistry*, 116(3), 638–643.
- Clark, H. M. (1992). The influence of the flow field in slurry erosion. *Wear*, 152(2), 223 - 240. doi: [http://dx.doi.org/10.1016/0043-1648\(92\)90122-O](http://dx.doi.org/10.1016/0043-1648(92)90122-O)
- Cloete, S., AMini, S., Johansen, S., Braun, M., & Popoff, B. (2011). Evaluation of a lagrangian discrete phase modeling approach for application to industrial scale bubbling fluidized beds. In *Proceedings of the 10th international conference on circulating fluidized beds and fluidization technology*.
- Cloete, S., Johansen, S., Braun, M., Popoff, B., & Amini, S. (2010). Evaluation of a lagrangian discrete phase modeling approach for resolving cluster formation in cfb risers. In *Proceedings of the 7th international conference on multiphase flow*.

- Cooke, R., Johnson, G., & Goosen, P. (1999). Laboratory apparatus for evaluating slurry pipeline wear. In *Bhr group conference series publication* (Vol. 36, pp. 647–662).
- Costa, A., & Macedonio, G. (2003). Viscous heating in fluids with temperature-dependent viscosity: implications for magma flows. *arXiv preprint physics/0302100*.
- Del Giudice, S., Nonino, C., & Savino, S. (2007). Effects of viscous dissipation and temperature dependent viscosity in thermally and simultaneously developing laminar flows in microchannels. *International journal of heat and fluid flow*, 28(1), 15–27.
- Ding, J., & Gidaspow, D. (1990). A bubbling fluidization model using kinetic theory of granular flow. *AIChE journal*, 36(4), 523–538.
- Edwards, J., McLaury, B., & Shirazi, S. (1998). Supplementing a cfd code with erosion prediction capabilities. In *Proceedings of asme fedsm* (Vol. 98).
- Erosive wear in piping systems* (Standard No. DNV RP O501 Revision 4.2). (2007). Hovik, Norway: Det Norske Veritas.
- Faddick, R. (1975). Pipeline wear from abrasive slurries. In *First internat. conf. internal and external protection of pipes, bhra fluid engineering, bedford, england. 1975, 9 p.*
- Finnie, I. (1960). Erosion of surfaces by solid particles. *Wear*, 3(2), 87–103.
- Gidaspow, D., Bezburuah, R., & Ding, J. (1991). *Hydrodynamics of circulating fluidized beds: kinetic theory approach* (Tech. Rep.). Illinois Inst. of Tech., Chicago, IL (United States). Dept. of Chemical Engineering.
- Gnanavelu, A., Kapur, N., Neville, A., & Flores, J. (2009). An integrated methodology for predicting material wear rates due to erosion. *Wear*, 267(11), 1935 - 1944. ({ICAP} 2008) doi: <http://dx.doi.org/10.1016/j.wear.2009.05.001>
- Govier, G. W., Aziz, K., & Schowalter, W. (1973). The flow of complex mixtures in pipes. *Journal of Applied Mechanics*, 40, 404.
- Gustavsson, M. (2002). Fluid dynamic mechanisms of particle flow causing ductile and brittle erosion. *Wear*, 252(11-12), 845 - 858. doi: [http://dx.doi.org/10.1016/S0043-1648\(01\)00688-3](http://dx.doi.org/10.1016/S0043-1648(01)00688-3)
- Haider, A., & Levenspiel, O. (1989). Drag coefficient and terminal velocity of spherical and nonspherical particles. *Powder technology*, 58(1), 63–70.

- Herrera-Velarde, J., Zenit, R., & Mena, B. (2001). Viscous dissipation of a power law fluid in an oscillatory pipe flow. *Revista Mexicana de Física*, 47(4), 351–356.
- Herschel, W. H., & Bulkley, R. (1926). Konsistenzmessungen von gummi-benzollösungen. *Colloid & Polymer Science*, 39(4), 291–300.
- Hiltunen, K., Jäsberg, A., Kallio, S., Karema, H., Kataja, M., Koponen, A., . . . Taivassalo, V. (2009). Multiphase flow dynamics. *Theory and Numerics. Tech. Rep*, 722.
- Humphrey, J. (1990). Fundamentals of fluid motion in erosion by solid particle impact. *International Journal of Heat and Fluid Flow*, 11(3), 170 - 195. doi: [http://dx.doi.org/10.1016/0142-727X\(90\)90036-B](http://dx.doi.org/10.1016/0142-727X(90)90036-B)
- Huser, A., & Kvernfold, O. (1998). Prediction of sand erosion in process and pipe components. In *Bhr group conference series publication* (Vol. 31, pp. 217–228).
- Jenkins, J., & Savage, S. (1983). Theory for the rapid flow of identical, smooth, nearly elastic, spherical particles. *Journal of Fluid Mechanics*, 130(1), 187–202.
- Kacker, R. N., Lagergren, E. S., & Filliben, J. J. (1991). Taguchi's orthogonal arrays are classical designs of experiments. *Journal of research of the National Institute of Standards and Technology*, 96(5), 577–591.
- Khatyr, R., Ouldhadda, D., & Idrissi, A. I. (2003). Viscous dissipation effects on the asymptotic behaviour of laminar forced convection for bingham plastics in circular ducts. *International Journal of Heat and Mass Transfer*, 46(4), 589 - 598. doi: [http://dx.doi.org/10.1016/S0017-9310\(02\)00331-9](http://dx.doi.org/10.1016/S0017-9310(02)00331-9)
- Koo, J., & Kleinstreuer, C. (2004). Viscous dissipation effects in microtubes and microchannels. *International Journal of Heat and Mass Transfer*, 47(14-16), 3159 - 3169. doi: <http://dx.doi.org/10.1016/j.ijheatmasstransfer.2004.02.017>
- Labsi, N., Benkahla, Y. K., FEDDAOUI, M., & Boutra, A. (2015). Viscous dissipation effect on the flow of a thermodependent herschel-bulkley fluid. *Thermal Science*, 19(5), 1553–1564.
- Lin, N., Lan, H.-Q., Xu, Y.-G., Cui, Y., & Barber, G. (2015). Coupled effects between solid particles and gas velocities on erosion of elbows in natural gas pipelines. *Procedia Engineering*, 102, 893 - 903. doi: <http://dx.doi.org/10.1016/j.proeng.2015.01.210>

- Lottermoser, B. G. (2011). Recycling, reuse and rehabilitation of mine wastes. *Elements*, 7(6), 405–410.
- Lun, C., Savage, S. B., Jeffrey, D., & Chepuruiy, N. (1984). Kinetic theories for granular flow: inelastic particles in couette flow and slightly inelastic particles in a general flowfield. *Journal of fluid mechanics*, 140, 223–256.
- Mansouri, A., Arabnejad, H., Shirazi, S., & McLaury, B. (2015). A combined cfd/experimental methodology for erosion prediction. *Wear*, 332-333, 1090 - 1097. (20th Intenational Conference on Wear Materials) doi: <http://dx.doi.org/10.1016/j.wear.2014.11.025>
- McLaury, B. S., Shirazi, S., Shadley, J. R., & Rybicki, E. (1999). *How operating and environmental conditions affect erosion* (Tech. Rep.). NACE International, Houston, TX (United States).
- Miller, J. (1986). The mechanics of wear in slurry dumping. In *International symposium on slurry flows*.
- Min, T., Choi, H. G., Yoo, J. Y., & Choi, H. (1997). Laminar convective heat transfer of a bingham plastic in a circular pipe. Numerical approach hydrodynamically developing flow and simultaneously developing flow. *International Journal of Heat and Mass Transfer*, 40(15), 3689–3701.
- Morini, G. L. (2005). Viscous heating in liquid flows in micro-channels. *International Journal of Heat and Mass Transfer*, 48(17), 3637 - 3647. doi: <http://dx.doi.org/10.1016/j.ijheatmasstransfer.2005.01.011>
- Nabil, T., El-Sawaf, I., & El-Nahhas, K. (2014). Sand-water slurry flow modelling in a horizontal pipeline by computational fluid dynamics technique. *International Water Technology Journal*.
- Ng, B., Ding, Y., & Ghadiri, M. (2009). Modelling of dense and complex granular flow in high shear mixer granulator - a {CFD} approach. *Chemical Engineering Science*, 64(16), 3622 - 3632. doi: <http://dx.doi.org/10.1016/j.ces.2009.05.011>
- Nguyen, Q., Nguyen, V., Lim, C., Trinh, Q., Sankaranarayanan, S., Zhang, Y., & Gupta, M. (2014). Effect of impact angle and testing time on erosion of stainless steel at higher

- velocities. *Wear*, 321, 87 - 93. doi: <http://dx.doi.org/10.1016/j.wear.2014.10.010>
- Nguyen, V., Nguyen, Q., Liu, Z., Wan, S., Lim, C., & Zhang, Y. (2014). A combined numerical-experimental study on the effect of surface evolution on the water-sand multiphase flow characteristics and the material erosion behavior. *Wear*, 319(1-2), 96 - 109. doi: <http://dx.doi.org/10.1016/j.wear.2014.07.017>
- Oka, Y., & Yoshida, T. (2005). Practical estimation of erosion damage caused by solid particle impact: Part 2: Mechanical properties of materials directly associated with erosion damage. *Wear*, 259(1), 102–109.
- Oka, Y. I., Okamura, K., & Yoshida, T. (2005). Practical estimation of erosion damage caused by solid particle impact: Part 1: Effects of impact parameters on a predictive equation. *Wear*, 259(1), 95–101.
- Parsi, M., Najmi, K., Najafifard, F., Hassani, S., McLaury, B. S., & Shirazi, S. A. (2014). A comprehensive review of solid particle erosion modeling for oil and gas wells and pipelines applications. *Journal of Natural Gas Science and Engineering*, 21, 850 - 873. doi: <http://dx.doi.org/10.1016/j.jngse.2014.10.001>
- Pashias, N., Boger, D., Summers, J., & Glenister, D. (1996). A fifty cent rheometer for yield stress measurement. *Journal of Rheology (1978-present)*, 40(6), 1179–1189.
- Plastics – polymers / resins in the liquid state or as emulsions or dispersions – determination of viscosity using a rotational viscometer with defined shear rate* (Standard). (1993). Geneva, CH: International Organization for Standardization.
- Ragueb, H., & Mansouri, K. (2013). A numerical study of viscous dissipation effect on non-newtonian fluid flow inside elliptical duct. *Energy Conversion and Management*, 68, 124 - 132. doi: <http://dx.doi.org/10.1016/j.enconman.2012.12.031>
- Rankin, W. J. (2011). *Minerals, metals and sustainability: meeting future material needs*. CSIRO publishing.
- Reference document on best available techniques for management of tailings and waste-rock in mining activities* (Reference Document). (2009). European Union: European Commission.
- Rosin, P., & Rammler, E. (1933). The laws governing the fineness of powdered coal.

Journal of the Institute of Fuel, 7, 29–36.

- Roussel, N., & Coussot, P. (2005). Fifty-cent rheometer for yield stress measurements: from slump to spreading flow. *Journal of Rheology (1978-present)*, 49(3), 705–718.
- Saak, A. W., Jennings, H. M., & Shah, S. P. (2004). A generalized approach for the determination of yield stress by slump and slump flow. *Cement and concrete research*, 34(3), 363–371.
- Saeed, R., Uddin, F., Masood, S., & Asif, N. (2009). Viscosities of ammonium salts in water and ethanol+ water systems at different temperatures. *Journal of Molecular Liquids*, 146(3), 112–115.
- Salama, M., Venkatesh, E., et al. (1983). Evaluation of api rp 14e erosional velocity limitations for offshore gas wells. In *Offshore technology conference*.
- Schaeffer, D. G. (1987). Instability in the evolution equations describing incompressible granular flow. *Journal of differential equations*, 66(1), 19–50.
- Schowalter, W., & Christensen, G. (1998). Toward a rationalization of the slump test for fresh concrete: comparisons of calculations and experiments. *Journal of Rheology (1978-present)*, 42(4), 865–870.
- Sestak, J., & Charles, M. (1987). Temperature variation and pressure drop in pipelines-effects of non-newtonian behaviour, temperature dependent viscosity and viscous heating. *Journal of pipelines*, 6(1), 49–65.
- Standard test method for slump of hydraulic-cement concrete* (Standard No. 32000`1:2008). (2015). West Conshohocken, PA: ASTM International.
- Steward, N., & Spearing, A. (1992). Combating pipeline wear—an advancing technology. *Journal of the South African Institute of Mining and Metallurgy(South Africa)*, 92(6), 149–157.
- Thodesen, C., Xiao, F., & Amirkhanian, S. N. (2009). Modeling viscosity behavior of crumb rubber modified binders. *Construction and Building Materials*, 23(9), 3053–3062.
- Towards a hybrid eulerian-lagrangian {CFD} modeling of coal gasification in a circulating fluidized bed reactor. (2015). *Fuel*, 152, 131 - 137. Retrieved from <http://www.sciencedirect.com/science/article/pii/S0016236114010539> (International

Freiberg Conference on {IGCC} amp; XtL Technologies in 2014) doi: <http://dx.doi.org/10.1016/j.fuel.2014.10.058>

Tunc, G., & Bayazitoglu, Y. (2001). Heat transfer in microtubes with viscous dissipation. *International Journal of Heat and Mass Transfer*, 44(13), 2395 - 2403. doi: [http://dx.doi.org/10.1016/S0017-9310\(00\)00298-2](http://dx.doi.org/10.1016/S0017-9310(00)00298-2)

Wasp, E. J., Kenny, J. P., & Gandhi, R. L. (1977). Solid–liquid flow: slurry pipeline transportation.[pumps, valves, mechanical equipment, economics]. *Ser. Bulk Mater. Handl.;(United States)*, 1(4), 45–46.

Wayment, W. R. (1978). Backfilling with tailings—a new approach. In *Proceedings of 12th canadian rock mechanics symposium, mining with backfill. canadian institute of mining and metallurgy, quebec, special* (Vol. 19, pp. 111–116).

Yeoh, G. H., & Tu, J. (2009). *Computational techniques for multiphase flows*. Elsevier.

8 APPENDIX A

Table 8.1: Taguchi variables for erosion model

Trial	Solid fraction (%)	Flow velocity (ms^{-1})	Sand fraction in solid (%)
A1	70	0.75	15
A2	70	1.10	25
A3	70	1.70	30
A4	70	2.30	40
A5	70	2.70	50
A6	73	0.75	25
A7	73	1.10	30
A8	73	1.70	40
A9	73	2.30	50
A10	73	2.70	15
A11	76	0.75	30
A12	76	1.10	40
A13	76	1.70	50
A14	76	2.30	15
A15	76	2.70	25
A16	79	0.75	40
A17	79	1.10	50
A18	79	1.70	15
A19	79	2.30	25
A20	79	2.70	30
A21	82	0.75	50
A22	82	1.10	15
A23	82	1.70	25
A24	82	2.30	35
A25	82	2.70	40

Table 8.2: Erosion model material properties

Trial	Total sand fraction (%)	Yield stress (Pa)	Consistency index (Pas)	Total mass flow rate ($kg s^{-1}$)	Sand mass flow rate ($kg s^{-1}$)	Density without sand ($kg m^{-3}$)	Density with sand ($kg m^{-3}$)
A1	11	20.201	0.100	44.10	4.63	1728	1822
A2	18	22.687	0.188	65.42	11.46	1676	1843
A3	21	40.958	0.549	101.78	21.39	1647	1855
A4	28	149.013	2.032	139.92	39.21	1586	1885
A5	35	393.784	5.068	167.63	58.72	1517	1924
A6	18	27.390	0.100	44.93	8.38	1737	1898
A7	22	31.510	0.146	67.74	14.83	1707	1908
A8	29	45.205	0.614	106.07	30.97	1643	1934
A9	36	189.203	2.546	146.00	53.28	1571	1967
A10	11	83.400	0.373	163.84	17.94	1791	1881
A11	23	64.411	0.226	47.63	10.87	1776	1968
A12	30	60.321	0.151	70.58	21.47	1710	1988
A13	38	55.754	0.771	110.61	42.06	1635	2016
A14	11	212.437	1.500	144.43	16.48	1861	1946
A15	19	106.947	0.566	170.73	32.46	1806	1960

Table 8.3: Erosion model material properties

Trial	Total sand fraction (%)	Yield stress (Pa)	Consistency index (Pas)	Total mass flow rate ($kg s^{-1}$)	Sand mass flow rate ($kg s^{-1}$)	Density without sand ($kg m^{-3}$)	Density with sand ($kg m^{-3}$)
A16	32	74.745	0.305	49.56	15.67	1784	2048
A17	40	20.201	0.100	73.47	29.04	1706	2070
A18	12	407.172	3.341	110.58	13.11	1936	2016
A19	20	261.069	1.950	150.34	29.71	1881	2026
A20	24	192.116	1.314	177.02	41.98	1851	2032
A21	41	79.644	0.344	51.52	21.13	1788	2129
A22	12	668.885	5.910	74.22	9.13	2018	2091
A23	21	492.589	4.171	115.04	23.59	1964	2097
A24	25	402.768	3.299	155.95	38.38	1934	2101
A25	33	227.469	1.638	184.04	60.39	1867	2112

Table 8.4: Material properties of Mine-A viscous heating model

Trial	Solid fraction (%)	Density (kgm^{-3})	Yield stress (Pa)	Consistency index (Pas)	Thermal conductivity ($Wm^{-1}K^{-1}$)	Specific heat capacity ($Jkg^{-1}K^{-1}$)
A1	70	1801	36.54	0.5180	3.14	1715.14
A2	72	1843	82.78	1.0952	3.21	1644.66
A3	74	1887	150.61	1.4144	3.29	1574.18
A4	76	1934	240.03	2.1158	3.36	1503.70
A5	78	1983	351.04	2.9860	3.43	1433.22
A6	80	2034	483.64	4.0250	3.50	1362.74
A7	82	2088	637.83	5.2328	3.58	1292.25

Table 8.5: Material properties of Mine-B viscous heating model

Trial	Solid fraction (%)	Density (kgm^{-3})	Yield stress (Pa)	Consistency index (Pas)	Thermal conductivity ($Wm^{-1}K^{-1}$)	Specific heat capacity ($Jkg^{-1}K^{-1}$)
B1	70	1818	68.41	0.5710	9.74	1768.22
B2	72	1862	89.09	0.9990	10.00	1699.25
B3	74	1907	113.46	1.5678	10.26	1630.29
B4	76	1955	141.52	2.2774	10.53	1561.32
B5	78	2006	173.27	3.1278	10.79	1492.36
B6	80	2059	208.72	4.1190	11.05	1423.39
B7	82	2115	247.86	5.2510	11.31	1354.43

Table 8.6: Material properties of Mine-C viscous heating model

Trial	Solid fraction (%)	Density (kgm^{-3})	Yield stress (Pa)	Consistency index (Pas)	Thermal conductivity ($Wm^{-1}K^{-1}$)	Specific heat capacity ($Jkg^{-1}K^{-1}$)
C1	70	1554	17.60	0.0440	8.84	1805.21
C2	72	1579	30.27	0.2524	9.08	1737.30
C3	74	1605	50.11	0.7688	9.31	1669.39
C4	76	1632	77.13	1.5932	9.55	1601.49
C5	78	1659	111.33	2.7256	9.78	1533.58
C6	80	1688	152.70	4.1660	10.02	1465.67
C7	82	1717	201.25	5.9144	10.25	1397.76

Table 8.7: Sand and tailings composition

Material	Mine-A sand (%)	Mine-A tailings (%)	Mine-B tailings (%)	Mine-C tailings (%)
Na_2O	3.89	3.32	1.50	5.13
MgO	1.70	3.26	3.97	2.48
Al_2O_3	12.03	18.64	17.67	15.68
SiO_2	69.69	54.79	49.02	63.30
SO_3	-	2.83	7.29	1.59
K_2O	2.11	3.46	2.70	4.34
CaO	7.56	5.67	6.52	4.25
TiO_2	0.21	0.57	0.64	0.30
MnO	-	0.15	0.13	-
Fe_2O_3	2.31	6.75	9.15	2.29
CO_2	-	-	0.88	-

Table 8.8: Mine-A sand particle size distribution

S.No.	Particle Size (μm)	Combined Cumulative Retained (%)	Combined Cumulative Passing (%)
1	5000	4.62	95.38
2	2500	10.00	90.00
3	1250	79.86	80.14
4	630	40.16	59.84
5	315	66.08	33.92
6	160	84.00	16.00
7	120	86.89	13.11
8	91	89.78	10.22
9	69	92.67	7.33
10	52	93.44	6.56
11	39	94.06	5.94
12	30	94.78	5.22
13	22	95.50	4.50
14	17	96.21	3.80
15	13	96.87	3.13
16	10	97.47	2.53
17	7	98.02	1.98
18	5	98.50	1.50
19	4	98.88	1.12
20	3	99.20	0.80
21	2	99.45	0.55
22	1.7	99.66	0.34
23	1.4	99.78	0.22
24	1.1	99.97	0.03
25	0.96	100.00	0.00

9 APPENDIX B

1. UDF for viscous heating model with temperature independent viscosity:

```
#include "udf.h"
#include "math.h"

#define k 0.518
#define n 1.0
#define tau_0 36.54

DEFINE_SOURCE(vh_source, c, t, dS, eqn)
{
    real source;

    real phi;

    phi = 2 * (pow(C_DUDX(c,t),2) + pow(C_DVDY(c,t),2) + pow(C_DWDZ(c,t),2)) +
    pow((C_DUDY(c,t) + C_DVDX(c,t)),2) + pow((C_DUDZ(c,t) + C_DWDX(c,t)),2) +
    pow((C_DVDZ(c,t) + C_DWDY(c,t)),2);

    source = ((k * pow(phi,(n - 1)/2)) + (tau_0/sqrt(phi))) * phi;

    dS[eqn] = (((k * n)+k) * pow(phi,(n/2)) + tau_0)/(2 * pow(phi,(1/2)));

    return source;
}
```

2. UDF for viscous heating model with temperature dependent viscosity:

```
#include "udf.h"
#include "math.h"

#define k 0.518
#define n 1.0
```

```

#define tau_0 36.54
#define alpha -7636.8
#define T_alpha 296.95
#define T_0 287.65
#define T 293.15

DEFINE_SOURCE(vh_source, c, t, dS, eqn)
{
real source;

real phi;

phi = 2 * (pow(C_DUDX(c,t),2) + pow(C_DVDY(c,t),2) + pow(C_DWDZ(c,t),2)) +
pow((C_DUDY(c,t) + C_DVDX(c,t)),2) + pow((C_DUDZ(c,t) + C_DWDX(c,t)),2) +
pow((C_DVDZ(c,t) + C_DWDY(c,t)),2);

source = ((k * pow(phi,(n - 1)/2)) + (tau_0/sqrt(phi))) * phi;

dS[eqn] = (((k * n)+k) * pow(phi,(n/2)) + tau_0)/(2 * pow(phi,(1/2)));

return source;
}

```